SEARCHING FOR GRAVITATIONAL WAVES FROM BINARY SYSTEMS IN
NON-STATIONARY DATA

A Dissertation

Submitted to the Graduate Faculty of
the Louisiana State University and
Agricultural and Mechanical College
in partial fulfillment of the
requirements for the degree of
Doctor of Philosophy

in

The Department of Physics and Astronomy

by
Chad Hanna
B.S., The Pennsylvania State University, 2004
M.S., Louisiana State University, 2006
May, 2008

To Jenny for 4 years of patience.

Acknowledgments

For all of my success I would like to acknowledge those who have advised me and who gave me a clear path: Gabriela González for extreme patience and wisdom; for giving me room to learn my own way, while constructively pointing out my mistakes; for giving me opportunity to collaborate and contribute to the most exciting field I could imagine: Ben Owen for giving me my first opportunity for research as an undergrad and for talking sense into me about life, physics and everything even until this day: Patrick Brady for taking time to always carefully explain details to me no matter how busy he was and for gently steering me in the right direction various times; The compact binary coalescence group members, who have been good collaborators and friends, such as Duncan Brown, Jolien Creighton, Nick Fotopoulos, Lisa Goggin, Drew Keppel, Steve Fairhurst, Eirini Messaritaki, Gareth Jones, Alan Weinstein, Brian O'Reilly, Vicky Kalogera, Richard O'Shaughnessy, Thomas Cokelaer and many, many others. (Sorry to everyone I forgot to mention!) And I would like to thank many professors who have influenced me greatly and who have given me much advice: Luis Lehner, Juhan Frank, Joel Tohline, Joe Giaime, Jorge Pullin, and many others. I want to specifically thank my i fellow grad students who had to put up with me, but who have become my good friends; Ravi, Andy, Jake, Jeff, Sarah, and Rupal. My work is supported by NSF grants PHY-0605496, PHY-0355289, and PHY-0135389. The chapters of this thesis require additional acknowledgments...

Chapter 2: I thank the LIGO Scientific Collaboration and some specific members who helped me with the draft of the technical document on which much of this chapter is based: Thomas Cokelaer, Gabriela González, Andres Rodriguez and Jacob Slutsky. I thank my gracious reviewers: Alan Weinstein, Duncan Brown, and Laura Cadonati.

Chapter 3: First and foremost I would like to thank Ravi Kumar Kopparapu for holding us together and all of the other authors: Vicky Kalogera, Richard O'Shaughnessy, Patrick Brady, Gabriela Gonzalez and Steve Fairhurst. I thank Brent Tully for generously providing his most up to date nearby galaxies catalog in the preparation of the galaxy catalog. I thank the maintainers of HyperLeda database, P. Nutzman and the LSC CBC group.

Chapter 4: Thanks to my coauthors, Miguel, Evan, and Carlos. I wish to thank Luis Lehner for suggesting this project and for for putting up with so many of my questions. I thank Luis and Franz Pretorius for providing the test particle time of flight used in section 2. Gabriela González, Patrick Brady, Alessandra Buonanno and Jolien Creighton provided motivating discussions and insightful comments. I would also like to thank the Kavli Institute for Theoretical Physics, for their hospitality, where some of this work was completed. The Kavli Institute is supported by NSF grant PHY05-51164.

Chapter 5: I thank the LIGO Scientific Collaboration. Specifically I thank Lindy Blackburn for providing KleineWelle triggers and Gabriela González for much help with the draft.

Chapter 6: Thanks to Ben Owen for originally suggesting this project and many great discussions. I also had many fruitful conversations with Patrick Brady, Steve Fairhurst, Duncan Brown, Bruce Allen, Jolien Creighton, Gabriela González, Warren Johnson, Lai-Him Chan and Jacob Slutsky.

Preface

Much of the work presented in this thesis was directly a result of my involvement in the LIGO Scientific Collaboration (LSC). In places where I have reproduced results derived from LIGO data I have done so with permission from the LSC; however, the opinions represented here are my own and not those of the LSC. Even work that was not directly derived from LIGO data often involved much collaboration and discussion with LSC members. I hope that I have given credit where credit is due.

Table of Contents

List of Tables

List of Figures

Abstract

The gravitational wave detectors at the LIGO Observatories have achieved record sensitivity to gravitational-waves produced by astrophysical systems. The LIGO Scientific Collaboration has analyzed data taken in several science runs, searching for different signals. We describe a search for black holes with less than a solar mass in the LIGO data taken from February 22 to March 24, 2005. No gravitational waves were found, and an upper limit was set on the rate of mergers of such binary systems. This search, as well as other searches for binary systems, are affected by non-stationary noise. We describe the sophisticated pipeline that attempted to reduce the false trigger rate while maximizing the sensitivity to simulated signals. Details regarding this search and interpretation of this search are presented along with new strategies to increase the confidence in detection through signal based vetoes and better template waveforms.

1. Introduction: Gravitational-Waves and the LIGO Detectors

1.1 Gravitational-Waves

General relativity asserts that the curvature of space-time causes gravity. The presence of matter curves space-time and the curvature in turn determines the behavior of matter. The space-time metric provides a way to measure the distance and time between points in the curved space-time. This metric is not static and changes as the matter moves (1). For a dynamic system of sufficiently high mass, the metric can remain non-stationary far from the matter source even though the gravity is negligible. The non-stationarity propagates as a wave travelling at the speed of light changing the measured distance between local points as it passes. This phenomenon is known as a gravitational-wave. The effects of gravitational-waves are small and have not been directly observed.

The lack of direct observation is not without effort. In the 1960's Joseph Weber pioneered a method to directly observe gravitational radiation. He developed what are now referred to as Weber Bars. These instruments were ~ 1 meter bars of solid aluminum with resonance frequencies of ~ 2 KHz. A passing gravitational-wave could excite the resonance mode and sensors affixed to the bar could register such an excitement. In a series of Physical Review Letters (2; 3; 4) Weber described measuring coincident events between geographically separated bars (2), described that some events found in coincidence with three detectors had a high probability of being gravitational-waves (3), and even concluded that the events seemed to be related to a source at the center of the Galaxy (4). This caused a stir in the scientific community since the amplitude that he measured was significantly higher than what was expected from theory. Groups began to build their own Weber Bars but no group was able to verify Weber's claims that his events were gravitational-waves, citing errors in his data analysis procedures (5).

Even though Weber's claims of gravitational-wave detections were refuted, his work inspired experimenters to produce better detectors and analysis methods. One of the detection strategies proposed was to use laser interferometers. This technique has been realized through the current world-wide effort to detect gravitational-waves using the Laser Interferometric Gravitational-wave Observatory (LIGO) (6) and other detectors such as GEO (7), TAMA (8) and VIRGO (9).

Since a gravitational-wave changes the distance between two separated points rather than displacing an object by an absolute distance, the effect is commonly described in terms of strain, which is defined as the change in length divided by the total length. An example of how a gravitational-wave changes coordinate distances is given in figure 1.2.

1.1.1 Motivation for Searching for Compact Binary Coalescence

A binary system of compact objects, e.g. neutron stars or black holes, produces gravitational-waves, which if close enough to the detector could have detectable strain. It is expected that gravitational radiation drives the evolution of such binaries causing them to inspiral and coalesce as gravitational-waves carry off their energy and angular momentum. Gravitational radiation from compact binary coalescence is proved to exist based on observations of the
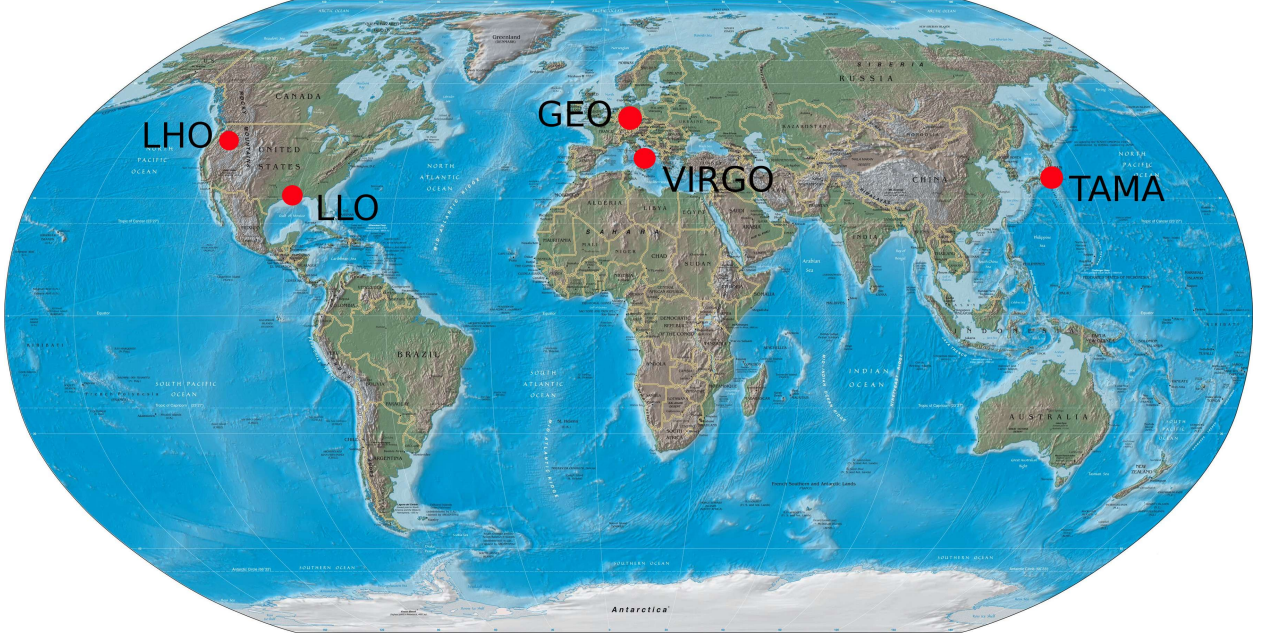
Figure 1.1: The three LIGO detectors at two sites, LHO in Hanford, WA USA and LLO in Livingston, LA USA, the British-German detector GEO, the French-Italian detector VIRGO and the Japanese detector TAMA form a world-wide network of interferometric gravitational-wave detectors. (image from **wikimedia.org**)

first binary pulsar PSR B1913+16 (10; 25). The shrinking orbit of this system is consistent with gravitational radiation to within 0.2 % (26); Gravitational radiation has not been observed directly from this system because no current detectors are sensitive to its very low frequency (< 1mHz) radiation. However, if PSR B1913+16 were about to coalesce it would be a very bright gravitational-wave source, detectable by LIGO and other detectors. The characteristic strains, h_c at a given frequency, f_c and waveforms for binary systems are known. The strains are approximately (11),

$$h_c = 4.1 \times 10^{-22} \left(\frac{\mu}{M\odot}\right)^{1/2} \left(\frac{M}{M\odot}\right)^{1/3} \left(\frac{100\text{Mpc}}{r}\right) \left(\frac{100\text{Hz}}{f_c}\right)^{1/6} \qquad (1.1)$$

where M is the total mass and μ is the reduced mass. Many other sources of gravitational radiation could exist producing comparable strains to (1.1).

Isolated neutron stars in our Galaxy might alone be gravitational-wave sources. If the neutron stars are not cylindrically symmetric, and spinning rapidly, they will radiate energy in gravitational-waves. This may explain the spin down of known pulsars. Recently upper limits on gravitational-wave emission from 78 known pulsars were set with LIGO data (12). Additionally analysts have done a "blind" all sky search looking for unknown pulsars, or isolated neutron stars, through gravitational-wave emission (13). There are many types of unmodeled, or poorly modeled gravitational-wave sources. Among these are supernova core collapse and gamma-ray engines. These systems are likely to produce short duration, perhaps broad band gravitational-wave signals. These "burst" signals have also been recently
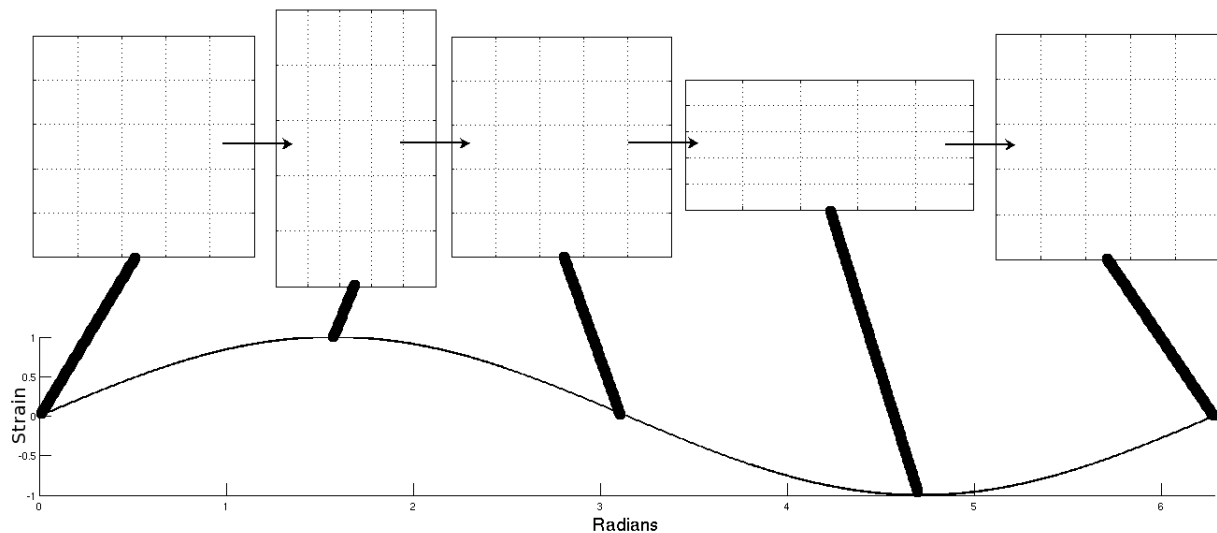
Figure 1.2: The effect of gravitational-waves on distances between points. This grid represents the metric on the 2 dimensional space of this page. As the gravitational-wave passes through the page the distances in the x and y directions of the grid shrink and expand. Gravitational-waves have two possible polarizations. Shown is the "plus" polarization. The "cross" polarization is rotated by 45º. One would measure different distances between free masses in the path of a gravitational-wave depending on the time of the measurement. LIGO attempts to measure the time varying metric with a laser interferometer because the light output will be modulated by the strain as shown in the partial sinusoid below. (see next section).

constrained (14). The effect of many weak unmodeled sources, including gravitational-waves left over from quantum fluctuations at the beginning of the Universe, has been analyzed through searching for a "stochastic background" of gravitational-waves (15). The focus of this work, however, will be on the detection of binary systems, where upper limits have also been recently presented (16).

1.2 The LIGO Detectors

In order to detect gravitational-waves from inspiraling binary systems, a gravitational-wave detector must be sensitive to the changes in coordinate distances between free masses as described in figure 1.2 at amplitudes given by equation (1.1). A simple Michelson interferometer can measure the relative change in distance between its two orthogonal arms by recording the light power output at the beam splitter. If the arms are the same length (up to a wavelength of the light), the fields will constructively interfere resulting in a bright output. As the arm's length changes differentially, the change in distance causes the light to interfere destructively, dimming the light, until it is dark. A gravitational-wave propagating

orthogonally to the plane of the interferometer will cause the path length of the light to differ in each arm, as demonstrated in figure 1.2. The change in length will result in a change in the light power output.

Laser Interferometric Gravitational-wave Observatory (LIGO) is a three detector network of interferometric gravitational-wave (GW) detectors located in two observatories in the United States, Hanford, Washington (LHO) and Livingston, Louisiana (LLO). The detectors attempt to measure gravitational-wave strain using a power-recycled Michelson interferometer with Fabry-Perot-cavity arms. LHO has two detectors called H1 (4 km arm length) and H2 (2 km) while the LLO site has one detector called L1 (4km). In order to measure strain of the magnitude given by equation (1.1), LIGO's optical design must be more complicated than a Michelson interferometer. The key to LIGO's strain sensitivity is its long arm lengths. Fabry-Perot cavities, which employ a set of partially reflective inner mirrors that cause light to circulate multiple times in the cavity, allow the phase difference caused by strain to accumulate as if LIGO's arms were effectively longer. A diagram of the simplified LIGO optical configuration is given in figure 1.3.
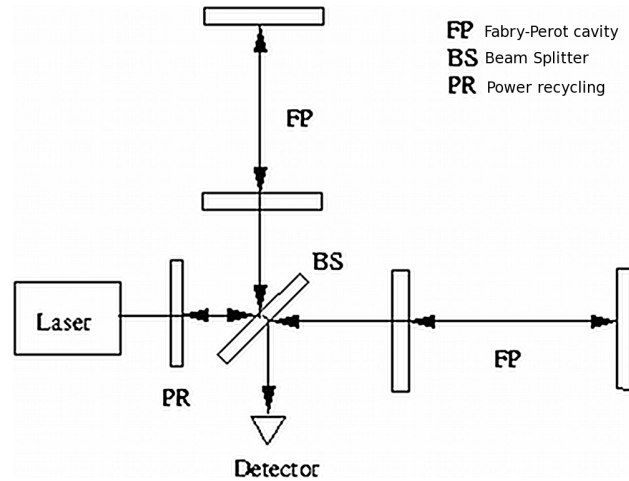
Figure 1.3: Simplified optical layout of LIGO (courtesy of Rupal Amin). LIGO is a power recycled laser Michelson interferometer with Fabry-Perot cavity arms. A gravitational-wave propagating perpendicular to both arms will change the distances between the mirrors in a similar fashion to figure 1.2. The light circulating in the cavity of one arm accumulates a phase difference with the other arm which changes the power observed at the detector port.

LIGO has collected data during five science runs. Its first science run, S1 (science run number one) began in 2002. It has since completed three additional science runs S2 (2003), S3 (2004) and S4 (2005), each contributing between 30 and 60 days of run time. Its most recent science run S5 ended in October 2007 and lasted for two years collecting 1 year of triple coincident data.

1.2.1 Noise Sources and Properties

LIGO detectors are limited by noise sources which mimic the strain of a passing gravitational-wave. The frequency dependence of the noise results in an effective bandwidth over which

LIGO is sensitive to the kind of strain magnitude given by equation (1.1) (17). Seismic motion, although attenuated by passive and active seismic isolation (20), limits the ability to measure strain below ~ 40Hz. This is the frequency below which sources would have to be very bright in order to be detectable. At high frequencies the noise is dominated by photon shot noise, which at ~ 2000 Hz is roughly the same amplitude as the seismic noise at 40 Hz $(\sim 2 \times 10^{-22}\,\text{strain}/\sqrt{\text{Hz}})$ for L1 and H1. The noise has a minimum at ~ 150 Hz where it is $\sim 2 \times 10^{-23}\text{strain}/\sqrt{\text{Hz}}$ and is dominated by thermal noise. 40-2000Hz is the bandwidth over which LIGO is most sensitive to inspiraling binary systems.

The frequency dependence of noise is measured by the noise power spectral density (PSD), $S_n(f)$. The PSD gives the power per unit frequency. Integrating it over all frequencies gives the average power of the signal. The Fourier transform of the detector data $s(t)$ is

$$\tilde{s}(f) \equiv \int_{-\infty}^{\infty} s(t)e^{-2\pi i f t}\mathrm{d}t \tag{1.2}$$

and its inverse is defined as,

$$s(t) \equiv \int_{-\infty}^{\infty} \tilde{s}(f)e^{2\pi i f t}\mathrm{d}f \tag{1.3}$$

One can define the PSD in the limit that the signal duration $T \to \infty$ as

$$S_n(f) \equiv \lim_{T\to\infty} \frac{1}{T}\tilde{s}(f)\tilde{s}^*(f) \tag{1.4}$$

For a special case, called stationary noise, the PSD is the Fourier transform of the auto-correlation function, $\mathcal{A}$ of the detector output, $s(t)$. If the detector output has a zero mean the auto-correlation function is defined as (21),

$$\mathcal{A}(t,\tau) = \langle s(t)\,s(t-\tau)\rangle = \lim_{T\to\infty} \frac{1}{T}\int_{t-T/2}^{t+T/2} s(t')s(t'-\tau)\mathrm{d}t' \tag{1.5}$$

In general the auto-correlation is a function of two variables t, τ. Noise that is stationary has an auto-correlation function that does not depend on the absolute value of time, but only on the relative time difference between two points. In other words,

$$\mathcal{A}(\tau)_{\text{stationary}} = \mathcal{A}(0,\tau) = \lim_{T\to\infty} \frac{1}{T}\int_{-T/2}^{T/2} s(t')\,s(t'-\tau)\mathrm{d}t' \tag{1.6}$$

Taking the integration limits to be ∞, using the Wiener-Khinchin theorem,

$$\mathcal{A}(\tau)_{\text{stationary}} = \lim_{T\to\infty} \frac{1}{T}\int_{-\infty}^{\infty} \tilde{s}(f)^*\tilde{s}(f)\,e^{-2\pi i f \tau}\mathrm{d}f \tag{1.7}$$

This shows that the PSD is the Fourier transform of the autocorrelation,

$$S_n(f) = \lim_{T\to\infty} \frac{\tilde{s}(f)^*\tilde{s}(f)}{T} = \frac{1}{T}\int_{-\infty}^{\infty} \mathcal{A}(\tau)e^{2\pi i f \tau}\mathrm{d}\tau \tag{1.8}$$

The amplitude spectral density (ASD) is defined as $\sqrt{S_n(f)}$.

This picture of the PSD is the most useful for discussion. By neglecting low frequency periodicity, where $|f| \lesssim 1/\tau$ the PSD may be estimated by truncating the auto-correlation function to a finite time τ. This results in a discrete number of frequencies allowed. LIGO data is digitized and is thus already discrete by time steps that are the reciprocal of the sampling rate f_s. The frequencies are bounded by the sampling rate f_s but the resolution is limited by the duration of the sample τ. Stationary noise allows this quantity to be computed for any start time. The PSD will not be time dependent for stationary noise. Within the resolution mentioned above it is possible to get a better estimate of the PSD by averaging (or taking the median) of several instances of the discrete PSD. This is how the PSD is estimated for compact binary searches in LIGO data (see chapter 2). An example of the S5 noise amplitude spectral density is shown in figure 1.4.
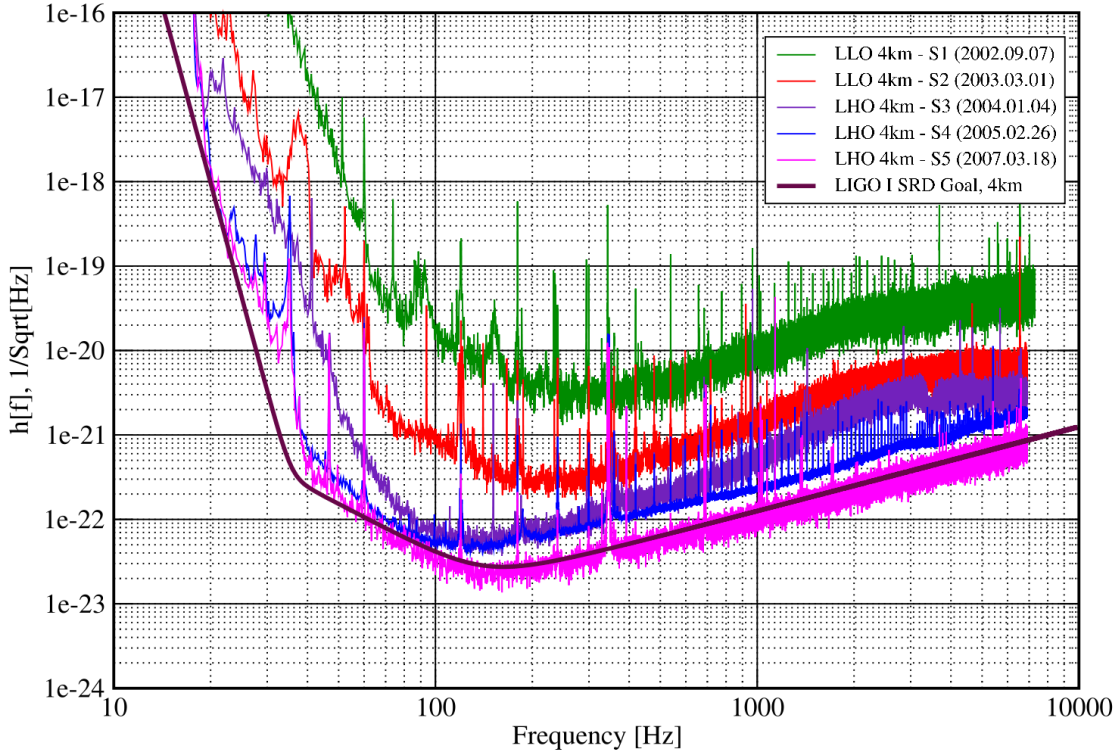
Figure 1.4: LIGO noise amplitude spectral density. The low frequencies are dominated by seismic motion. The high frequencies noise are dominated by shot noise. 40-2000Hz is the effective bandwidth where LIGO is sensitive to the systems with characteristic strain described by equation (1.1). Some massive binary systems will not reach 40Hz in gravitational-wave frequency and are thus not detectable (see chapters 2 and 4.

Non-stationary noise can have a time-dependent PSD. LIGO noise is generally non-stationary over some time scales. The remainder of this work will somewhat artificially describe two time scales over which the noise is non-stationary. The long time scale is one where the non-stationary features are longer than the correlation time, τ. For example, LIGO detectors have different sensitivity during the night than during the day because of man-made noise during business hours. By measuring the PSD over minute time scales the transition from day-to-night sensitivity is comparatively slow such that the noise during each estimate of the PSD is roughly stationary. Data can be analyzed over these short time scales to capture the slowly varying non-stationary characteristics. It is also possible for the noise to be non-stationary over shorter time scales than the PSD estimate. If the non-stationarity is much shorter than τ it does not influence the PSD (especially if averaging is done) but can cause serious problems in data analysis. These short non-stationary noise components are referred to as glitches or transients. Glitches can mimic gravitational-wave signals and are responsible for higher than expected false alarm rates from stationary noise in LIGO searches for compact binary coalescence (see chapters 2, 5 and 6).

1.3 The LIGO Scientific Collaboration

The LIGO Scientific Collaboration (LSC) is an international collaboration with presently over 600 members from nearly 60 institutions (18). The primary functions of the LSC are summarized in this excerpt of the LSC charter (19),

LSC Mission: *The LIGO Scientific Collaboration (LSC) is a self-governing collaboration seeking to detect gravitational-waves, use them to explore the fundamental physics of gravity, and develop gravitational-wave observations as a tool of astronomical discovery. The LSC works toward this goal through research on, and development of techniques for, gravitational-wave detection; and the development, commissioning and exploitation of gravitational-wave detectors. No individual or group will be denied membership on any basis except scientific merit and the willingness to participate and contribute as described in this Charter.*

LSC Responsibilities: *The LSC is the entity within LIGO that carries out LIGOs scientific research program. Memoranda of Understanding between member groups and the LIGO Laboratory establish the individual group responsibilities to allow the LSC to perform the following functions:*

    a. establish the overall data analysis strategy, goals, and time-line, and carry out the data analysis program

    b. identify priorities for research and development, and carry out the R&D program

    c. carry out an outreach program to communicate LIGOs activities and goals to the public, and to provide educational opportunities for young people

    d. disseminate the results of the data analysis program and the R&D program

    e. participate in the scientific operations of the LIGO detectors

    f. perform internal evaluation of progress in data analysis and R&D, making adjustments as necessary

The LSC has four astrophysics working groups that are involved in data analysis, interpretation, and the preparation of publications and presentations of the results to the general public. The working groups are roughly based on the types of gravitational-wave sources mentioned previously. The four groups focus on, but are not limited to,

Compact binary coalescence – This working group searches for gravitational-waves emanating from the inspiral and merger of binary compact objects.

Continuous wave sources – This working group attempts to find continuous gravitational-wave sources such as those arising from deformed neutron stars (pulsars). This group conducts directed searches for known pulsars and all sky searches.

Stochastic sources – This working group attempts to find a stochastic gravitational-wave background, which could be the sum of multiple unresolved sources, or the remnants of gravitational-waves created in the early universe.

Unmodeled burst sources – This working group searches for short duration, but otherwise unmodeled gravitational-wave signals. These could arise from super nova, gamma ray bursts, or some other unknown phenomenon.

My role in the LSC thus far has been to work in the compact binary coalescence group conducting searches and interpreting results. A large fraction of the material in this thesis will describe work I conducted within the LSC. However, the opinions presented are my own and do not reflect those of the collaboration.

1.4 Description of the Remaining Chapters

The following chapters describe how to search for compact binary coalescence in non-stationary LIGO data and how to interpret the results. Chapter 2 describes a search for sub solar mass compact binaries in LIGO's fourth science run (S4). The search resulted in no plausible gravitational-wave candidates (16). However, it did result in establishing an upper limit on the rate of such events in the universe. Chapter 3 describes a key part of the astrophysical interpretation of searches - as rate upper limits - in terms of the nearby host galaxies for such systems. It also discusses how to extend the rate upper limit calculations as searches become more sensitive. Chapter 4 discusses one way in which modern advances in numerical relativity, and theory, can impact LIGO searches for compact binary coalescence by better predicting the end of inspiral phases for binary systems. The result is that longer inspiral phases may result in a more detectable signal for some binaries. One of the recurring themes in chapter 2 is the non-stationarity of LIGO noise and its effect on searches for compact binary coalescence. Chapters 5 and 6 discuss ways to combat the ill effects of non-stationarity in searches for compact binary coalescence. Chapter 5 discusses how to use one of LIGO's auxiliary data channels to measure times of transient noise sources and veto candidate events at those times. Chapter 6 examines new computationally efficient ways of performing chi-squared tests on the data to check the goodness of fit with the expected wave forms. Chapter 7 provides some concluding remarks.

2. Search for Sub-Solar Mass Compact Objects in LIGO's Fourth Science Run

2.1 Introduction

As mentioned in chapter 1, LIGO is sensitive to the gravitational radiation emitted by the inspiral phase of compact binary coalescence (CBC) from combinations of neutron stars (NS) and black holes (BH) for systems with total mass $\lesssim 100 M_\odot$ (16). The inspiral phase is a succession of shrinking quasi-circular orbits driven by angular momentum loss from gravitational radiation that ends when the binary has reached an innermost-stable-circular-orbit (ISCO) (22) (see chapter 4). The binary then begins to plunge resulting in either a single heavy neutron star or black hole. If the merger product is a black hole, it will oscillate and radiate more gravitational-waves at its quasi-normal mode frequencies until radiation damps the excitation (23). The gravitational-waves produced by the ring down are also visible to LIGO for higher mass systems $\sim 10 - 400 M_\odot$ (24). All systems above $\sim 500 M_\odot$ will merge and ring down at frequencies too low to detect with current-generation LIGO (see chapter 1).

One of the LIGO Scientific Collaboration's (LSC) goals is to detect gravitational radiation from inspiraling compact objects or some other astrophysical source. Upon detection, LIGO can provide confidence intervals on the rate of NS-NS, NS-BH and BH-BH mergers in the nearby universe (33). In the absence of detection, LIGO can set upper limits for the rate of compact binary coalescence (33; 16). The upper limit on rate is inversely proportional to the observation time and to the population of binaries surveyed by LIGO. NS-NS binary populations are expected to be proportional to the blue light luminosity of a galaxy, which is measured in units of $L_{10} \equiv 10^{10} \times L_{B,\odot}$ in this work (see chapter 3). Knowing the blue luminosity of galaxies within LIGO's range provides the expected population of binaries (34). Rates are a function of mass because the expected astrophysical merger rate is not independent of mass nor is LIGO sensitive to all masses equally.

For LIGO's third (S3: Oct. 31, 2003 – Jan. 9, 2004) and fourth (S4: Feb. 22 – Mar. 24, 2005) science runs the search parameter space of compact binaries was broken into three mass ranges (16): {0.35-1.0} $M_\odot$ systems were called primordial black holes (PBH); {1.0-3.0} $M_\odot$ systems were called binary neutron stars (BNS); {3.0-40} $M_\odot$ systems were considered to be binary black holes (BBH). However, these searches would be sensitive to any compact objects in the mass range, (e.g. the BNS search would be sensitive to stellar mass black holes). Primordial black holes are called such because no stellar evolution process can produce a black hole with a mass below about 1.4 $M\odot$ (28). However it is possible that density fluctuations in the early Universe could lead to regions that collapsed into black holes of somewhat arbitrary size depending on the model (29). It was thought that PBH could explain the Massive Compact Halo Objects observed from micro-lensing (30) and the implications for gravitational-wave detection were explored assuming that $\sim 0.5 M_\odot$ PBHs were in high abundance in our Galaxy (31). However this assumption is controversial (32) Constraints on the masses of neutron stars observed in pulsar binaries are rather sharp and may be about $1.35 \pm 0.04 M_\odot$ (27). But even allowing for other models, the present LIGO search range should be quite sensitive to neutron star binaries. Binary black holes have not been directly observed. But black holes of a few solar masses are expected products of stellar

evolution (though there is a maximum size since stars do not form on the Main Sequence above $\sim 120 M_\odot$ and their remnants will be much smaller (28)).

The S4 data set, which contained 576 hours of data sensitive to a range of ~ 10 Mpc, yielded no detections but did provide rate upper limits for characteristic equal mass systems with total masses $\{1.5, 2.8, 10\}$ $M_\odot$ of $\{4.9, 1.2, 0.5\}$ yr^{-1} L_{10}^{-1} (16).

These rate upper limits can be compared to expected rates for these systems from population synthesis models and binary pulsar observations. NS-NS binaries are expected to merge at a rate of about $\sim 50 \times 10^{-6} \mathrm{yr}^{-1} L_{10}^{-1}$ (35; 16), whereas BH-BH merger rates may be $\sim 1 \times 10^{-6} \mathrm{yr}^{-1} L_{10}^{-1}$ (36; 16). Clearly the upper limits provided by the fourth science run are far from the expected astrophysical rates, thus making a detection unlikely with the present LIGO detector. The two basic ways to increase the chance of detection and lower the rate upper limit is to observe for a longer time, or to increase LIGO's sensitivity. The upper limits are most effected by changes in sensitivity because a 10 times greater range gives 1000 times more space volume, and thus roughly 1000 times more L_{10}s and 1000 times higher rate. There are currently plans to enhance LIGO and produce more sensitive detectors in the coming years (39). Even without advanced detectors the sensitivity of a search can be improved by reducing the false alarm rate. The CBC rate upper limit is based on the loudest event that results from the search (37; 38). Non-stationary noise can impact the rate upper limit negatively by producing a loud event caused by a spurious noise source. Correctly accounting for data quality and introducing advanced signal processing techniques helps to reduce the significance of the loudest event (see chapters 5 and 6) and increases the sensitivity of the search.

In general attaining the best search efficiency and the lowest background event requires advanced pipelines and intricate tuning (40). The focus of this chapter will be to show the LIGO CBC search pipeline in action using the S4 PBH search, which I lead, as an example. This chapter shows the matched-filtering-based CBC detection pipeline (41), which cross correlates detector data with a template waveform, augmented by coincidence between detectors, advanced signal processing techniques and sophisticated ways to measure the background events. These techniques would not be necessary if LIGO's noise was stationary. This chapter steps through the data analysis process used in the LIGO S4 search for primordial black holes (PBH) leading to the rate upper limit result.

2.2 Pipeline

The LIGO CBC pipeline is a multi-stage process whereby intermediate data products are produced then compared with other data products and eventually migrated downstream resulting in a set of candidate events. The hierarchy is required because of the computational burden of CBC searches in non-stationary LIGO detector data. Figure 2.1 shows the process schematically.

2.2.1 Stage 1: Data Acquisition

As mentioned in chapter 1, a gravitational-wave incident on the LIGO detector will cause a change in the relative optical path length in each arm. LIGO is normally locked into a "dark fringe" by servo control loops, which apply the necessary forces to the mirrors, causing the light in each arm to destructively interfere as it is recombined at the beam splitter (44; 45; 46). The signals used in the control process capture the effects of a passing gravitational-wave and counter the strain by moving the mirrors. The error and control signals are recorded. While the recorded signals encode the gravitational-wave strain, they do not do so directly.
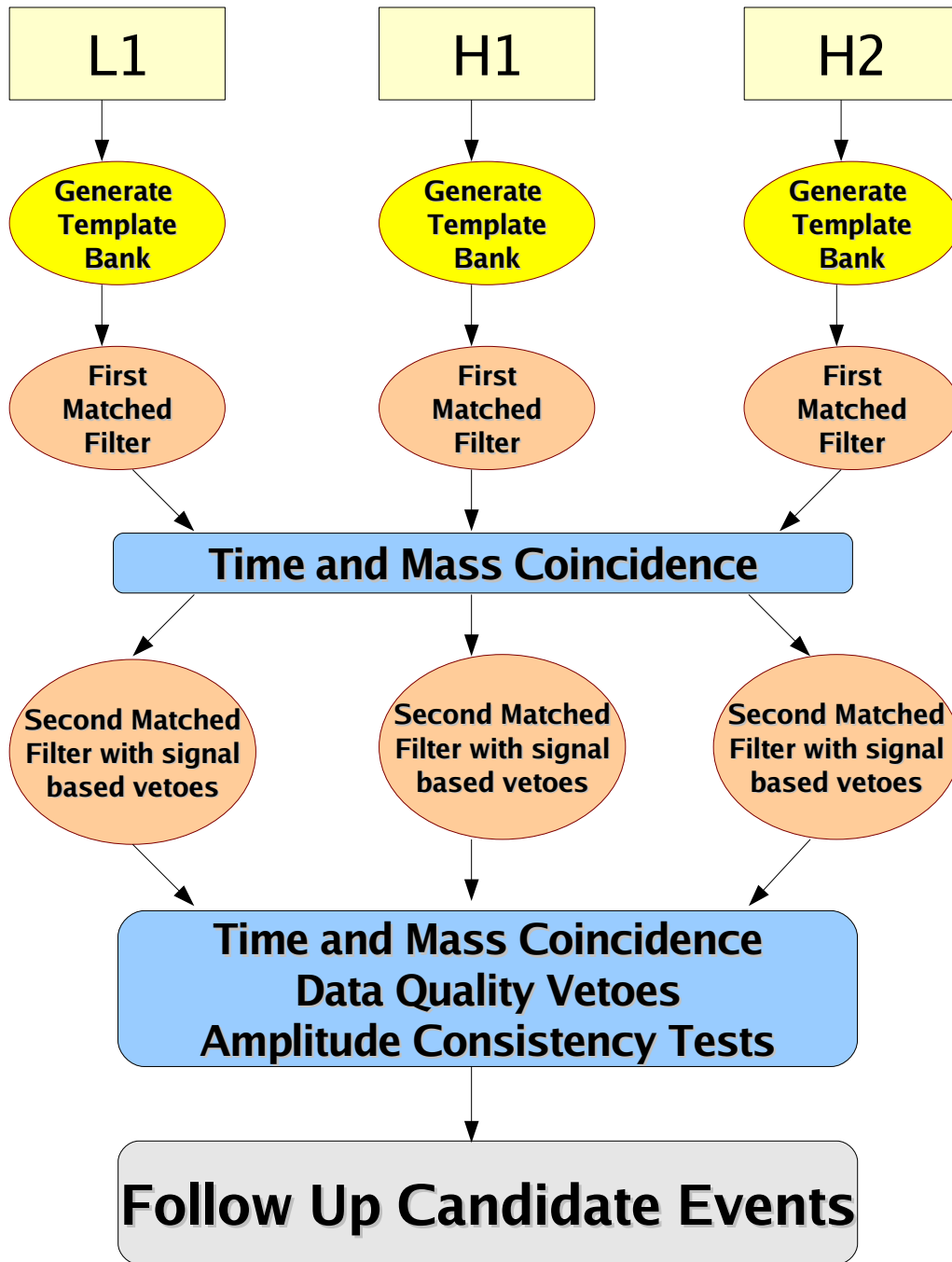
Figure 2.1: Pictorial flow of the S4 PBH analysis pipeline.

The effect of the strain is changed as it propagates through the servo loops by the optical response of LIGO's Fabry-Perot cavities and by the various analog and digital electronics involved in the control process. For this reason the signal must be calibrated (44; 45; 46). Once the appropriate response function is applied to the recorded signal, it represents the strain to sufficient accuracy for data analysis (43). From here forward I'll assume that the appropriate calibration has been applied to the data stream and will henceforth refer to LIGO data in units of strain.

LIGO data is digitally sampled at 16384Hz and recorded contiguously. For the S4 PBH search the data is further down-sampled to 4096Hz. The contiguity of data useful for science is broken when the interferometer goes out of lock or suffers from some known pathology (issues of data quality will be discussed later, see table 2.4). Most inspiral data analysis is done "off line" on relatively small blocks of archived data. All blocks are the same size and the size is determined by two criteria: 1) the duration of the inspiral signal in the measurable band (about 40-2000Hz), which is ~ 1 minute for a solar mass binary, and 2) the estimation of the noise power spectral density (PSD). These blocks form the basic unit of the power spectral density estimate introduced in chapter 1. The S4 PBH search used 2048 second blocks.

All inspiral analysis routines rely on an accurate measure of the power spectral density (47). It is important that the power spectral density is not biased by the gravitational-wave signal or by glitches. The PSD is estimated using longer blocks of data than the signal but shorter than the long scale time variations in sensitivity as discussed in chapter 1. For inspiral data analysis the PSD is estimated by taking the median of 15 50%-overlapping segments each 256s long in a 2048s block of contiguous data. If a signal or glitch exists in just one of the segments it will not bias the estimate of the median PSD (47) over the block. The block is the main unit of data analysis and is passed into the remaining stages of the data analysis pipeline. A schematic of the pipeline is given in figure 2.2. A plot of the S4 noise ASD - which is the square-root of the PSD - is shown in figure 1.4.

Each LIGO detector has its own data set and therefore its own PSD. Several stages of the pipeline (template bank generation, matched filtering and signal based vetoes) require the PSD estimate of the individual detectors. The next section will address how various systems are searched for by constructing banks of template waveforms that match the expected astrophysical signal. The construction of these banks relies on the noise PSD and will be based on the 2048s block introduced above.

2.2.2 Stage 2: Template Banks

LIGO is not equally sensitive to all binary inspirals with a similar incident flux of gravitational radiation. LIGO's sensitivity to a system depends on how long the system is expected to radiate at frequencies *with the lowest noise* ($\sim 40 - 2000$Hz). PBH, BNS, and BBH inspirals all begin their evolution well below 40Hz but their merger frequencies are quite different. Some systems merge before ever reaching LIGO's sensitive region, and some merge after they have already left. Merger frequencies can be estimated by the innermost stable circular orbit (ISCO) (see chapter 4), which for a test particle orbiting a Schwarzschild black hole is parametrized by total mass as $f_{\text{ISCO}} = 1600\text{Hz} \times (2.8 M_\odot / M_{\text{total}})$ (33). For this reason, there is a clear upper bound in mass that LIGO can detect (i.e., merger frequencies much below 40 Hz will not be detectable). However merger frequency is not the only factor in determining detectability; signal duration also depends on mass ratio and asymmetric mass systems radiate longer in the span between 40 Hz and ISCO. A binary system with a total mass of $\sim 40 M_\odot$ will coalesce at ~ 100Hz for all component mass configurations, but a {39, 1} $M_\odot$ pair lasts for over 2s, whereas an equal mass {20, 20} pair lasts only 0.2s. Longer
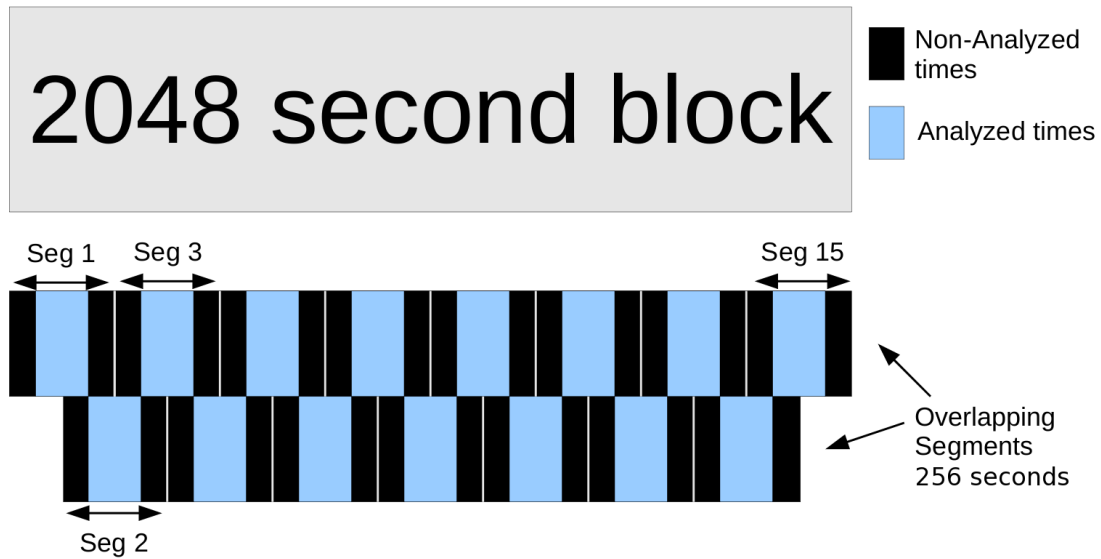
Figure 2.2: Diagram of how strain data is used for inspiral data analysis. The 2048s block is the main unit of data throughout the pipeline. The PSD is estimated from the median of overlapping 256s segments. Signals are searched for within the overlapping regions. The 2048s blocks used in PSD estimates are necessary because LIGO's noise changes over relatively short time scales. The PSD measured at one time can significantly differ from the PSD measured at another time. This is the first way in which non-stationary noise impacts LIGO searches for compact binary coalescence.

signals that span the same frequency range are generally more detectable if their amplitude is similar. However equal mass binaries radiate the most energy and are thus more detectable in a given volume of space than their asymmetric counterparts.

Current searches for compact binary coalescence use matched filtering, which requires template waveforms to characterize the *expected* signal from compact binary coalescence (16). Searches for primordial black holes rely on the post-Newtonian method which parametrizes the general relativistic interaction of two bodies in powers of $v = M\Omega$ where M is mass and Ω is the orbital frequency. For PBH searches, the second order approximation (2PN) suffices to generate accurate template waveforms. Because matched filtering is computationally most efficient in the frequency domain, it is useful to have waveforms available in the frequency domain to avoid the computational cost of having to Fourier transform time domain waveforms. The PN model has a frequency domain representation via the stationary phase approximation (49; 50). The waveforms are

$$\tilde{h}(f) = \left(\frac{1\text{Mpc}}{D_{\text{eff}}}\right) \mathcal{A}_{1\text{Mpc}} f^{-7/6} e^{i\Psi(f;M,\mu)} \tag{2.1}$$

$$\mathcal{A}_{1\text{Mpc}} = \frac{(\pi M)^{1/3} G^{5/6}}{c^{3/2}} \left(\frac{5\mu}{24}\right)^{1/2} \tag{2.2}$$

$$\Psi(f;M,\mu) = 2\pi f t_0 - 2\phi_0 - \pi/4$$
$$+ \frac{3}{128} \left[\nu^{-5} + \left(\frac{3\,715}{756} + \frac{55}{9}\eta\right)\nu^{-3} - 16\pi\nu^{-2}\right]$$
$$+ \frac{3}{128}\nu^{-1} \left[\frac{15\,293\,365}{508\,032} + \frac{27\,145}{504}\eta + \frac{3\,085}{72}\eta^2\right] \tag{2.3}$$

$$\nu = \left(\frac{GM\pi f}{c^3}\right)^{1/3}. \tag{2.4}$$

where M is the total mass of the binary $m_1 + m_2$, μ is the reduced mass defined as,

$$\mu = \frac{m_1\, m_2}{M} \tag{2.5}$$

η is the symmetric mass ratio defined as,

$$\eta = \frac{m_1\, m_2}{(m_1 + m_2)^2} \tag{2.6}$$

and ϕ_0 is the coalescence phase (47).

An example of the waveform is given in figure 2.3. The quantity D_{eff} is the distance in Mpc at which an optimally oriented and located binary would produce the strain given by Eq. 2.1. It is related to the binary's physical distance by orientation of the binary plane and the detector response:

$$D_{\text{eff}} = \frac{D}{\sqrt{F_+^2(1 + \cos^2\iota)^2/4 + F_\times^2(\cos\iota)^2}} \tag{2.7}$$

$$F_+ = -\frac{1}{2}(1 + \cos^2\theta)\cos 2\phi \tag{2.8}$$

$$F_\times = \cos\theta \sin 2\phi \tag{2.9}$$
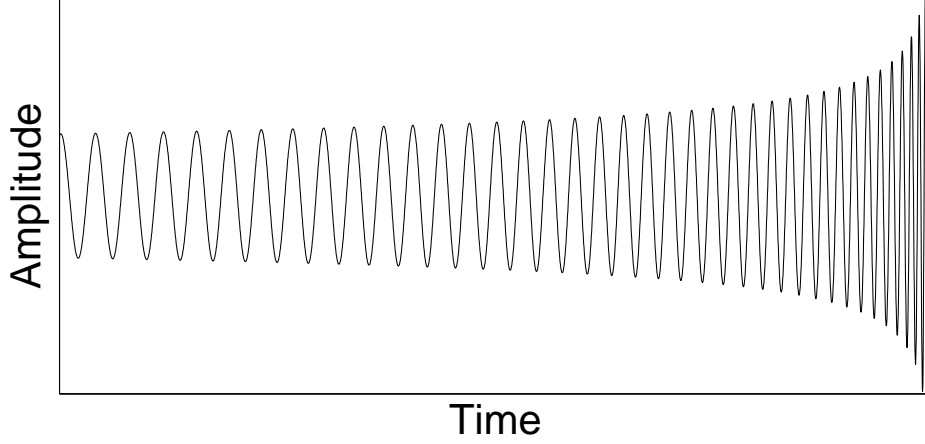
Figure 2.3: The waveform described in equation (4.12). The loss of angular momentum from gravitational radiation causes the orbit to shrink and the frequency to increase. The closer objects radiate even more and the frequency and amplitude of the gravitational wave increases and the signal "chirps". Because LIGO is sensitive to relatively high frequencies the compact objects must be close before LIGO can detect their gravitational radiation. Typically the radiation lasts at most a few minutes in LIGO's frequency band.

where F_+ and $F_\times$ are LIGO's antenna response function to the plus and cross polarizations (52), D is the binary's actual distance, ι is the inclination and θ, ϕ are the spherical coordinates of the sources sky position with respect to axes defined by LIGO's arms. The next chapter will discuss how effective distance is important in the calculation of merger rates using LIGO.

The template bank stage of our data analysis pipeline generates a discrete bank of the waveforms described by equation (4.12) for each detector and each block. The bank samples a user-defined mass parameter space, which is generally limited on the low mass end by the computational cost of filtering long templates and on the high mass end by the fact that the merger frequencies become too low to be detectable with LIGO. The template spacing is chosen by imposing a threshold on the expected loss of SNR for a signal that falls in between one of the discretely chosen filters(83). For example the SNR loss allowed in the S4 PBH search was 5% over a mass range of {0.35-1.0} $M_\odot$. An instance of an S4 PBH template bank is provided in figure 2.4.

In order to make the template bank placement more quantitative I'll define the following inner product between template waveforms $\tilde{h}_i(f)$ and $\tilde{h}_j(f)$,

$$\langle\, \tilde{h}_i(f; M_i, \mu_i) \,|\, \tilde{h}_j(f; M_j, \mu_j) \,\rangle = \int_{f_{\text{low}}}^{f_{\text{cut}}} \frac{e^{i(\Psi(f; M_i, \mu_i) - \Psi(f; M_j, \mu_j))}}{f^{-7/3}\, S_n(f)} \, \mathrm{d}f \qquad (2.10)$$
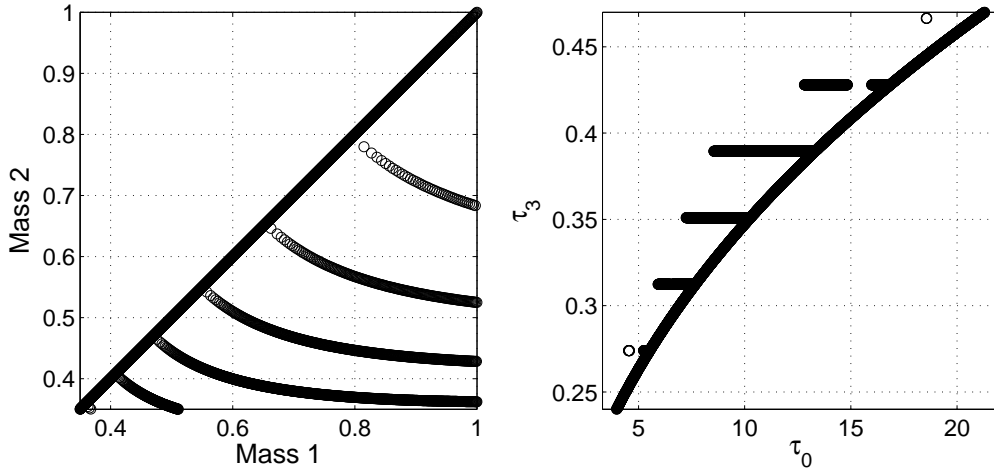
Figure 2.4: Template banks are chosen to cover a parameter space (e.g. component masses between $0.35M_\odot$ and $1M_\odot$) such that a real signal that falls in-between the discrete template spacing would still produce > 1-δ of a perfect match SNR. The resulting spacing is a function of mass, left. It is possible to find a coordinate transformation that make the spacing nearly rectilinear, right. The coordinates are $\tau_0 \propto m_1 m_2\, m^{-5/3}$ and $\tau_3 \propto m_1 m_2\, m^{-2/3}$.

The loss in SNR between two templates is related to the mismatch (83), or the orthogonal part of one template waveform to another. In other words we require,

$$\frac{\langle\, \tilde{h}_i(f; M_i, \mu_i)\, |\, \tilde{h}_j(f; M_j, \mu_j)\, \rangle}{\sqrt{\langle\, \tilde{h}_i(f; M_i, \mu_i)\, |\, \tilde{h}_i(f; M_i, \mu_i)\, \rangle\langle\, \tilde{h}_j(f; M_j, \mu_j)\, |\, \tilde{h}_j(f; M_j, \mu_j)\, \rangle}} = 1 - \delta \qquad (2.11)$$

that δ be a small number (0.05). Holding δ constant means that the template spacing can be a function of the integration limits, masses and the noise PSD since each of these effects the inner product. The lower cut off frequency was chosen to be 100Hz, instead of a possible 40Hz, in order to reduce the size of the template banks required to meet the minimal match condition of $\delta = 0.05$ for the S4 PBH search [1]. The peculiar spacing in the mass-mass plane, as shown in figure 2.4, can be made more regular by a change in coordinates (83), which makes it easier to choose the template spacing.

As mentioned before, most of the complication of LIGO's inspiral analysis pipeline comes from the complications of non-stationary noise. The fact that the template bank has to be computed every block is an example of this. When the noise PSD changes the inner product between templates changes and the size of the bank required to meet a given SNR loss requirement changes, see figure 2.5. Perhaps ironically, I'll demonstrate in chapter 6 how the rigorous template placement scheme, which is here complicated by non-stationarity, can actually be used to reject spurious triggers caused by non-stationarities. A table with a summary of the S4 PBH template bank properties is given in table 2.1 (16).

---

[1] The number of templates could have been reduced by increasing δ. However, we will see later that this can reduce the power of signal based vetoes, which are used to reject false alarms. Additionally changing the low frequency cut off had less impact on the sensitivity of the search than the equivalent change in δ
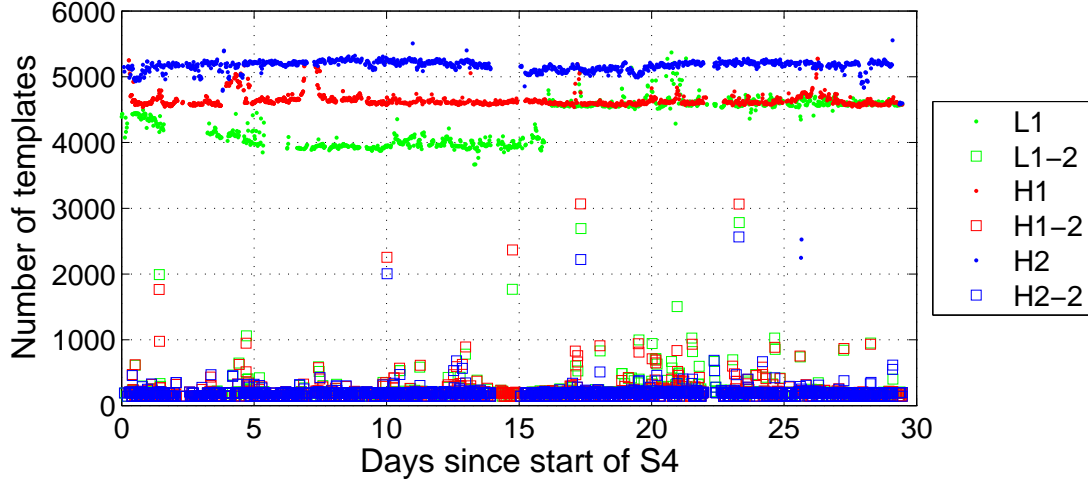
Figure 2.5: Template bank size fluctuations in S4 PBH searches. Template banks are re-computed for each 2048 s block of science time since template spacing depends on the noise power spectrum. The circles represent the template bank sizes of each detector for each 2048 s block analyzed, and the squares represent the sizes of the triggered template bank used in the second inspiral stage.

Table 2.1: Summary of template bank properties. The template bank size, for a constant δ is a function of the component mass range, lower integration limit and template length. The S4 PBH search is the most computationally burdensome search of the ones compared because it requires the most templates.

Search	Min. mass	Max mass ($M_\odot$)	f_{low} (Hz)	$\langle\#\rangle$	Min. length	Max length (s)
S3,S4 PBH	0.35	1.0	100	4500	3.9	22.1
S3 BNS	1.0	3.0	70	2000	1.6	10.0
S4 BNS	1.0	3.0	40	3500	7.1	44.4
S3 BBH	3.0	40.0	70	600	–	1.6
S4 BBH	3.0	80.0	50	1200	–	3.9

2.2.3 Stage 3: Matched Filtering

Once template banks are generated they are passed to the next stage of the pipeline, which is matched filtering the data. The LIGO matched filter engine cross correlates each template waveform in the bank, $h_i(f)$, weighted by the inverse of the noise PSD, $S_n(f)$, with the Fourier transformed detector output, $s(f)$. If the correlation crosses a set threshold then a trigger is generated and its parameters are stored for later stages of the pipeline. More on the details of matched filtering can be found in chapter 6. For now it is sufficient to know that the matched filter produces a complex output from the Fourier transformed template and detector output

$$z(t) = 4 \int_{f_{\text{low}}}^{f_{\text{final}}} \frac{\tilde{s}(f)^* \tilde{h}(f) e^{2\pi i f t}}{S_n(f)} df, \tag{2.12}$$

where the limits of integration, f_{low} and f_{final}, are determined from the low frequency sensitivity, which is fixed for a given search (see table 2.1), and the ending frequency of the template waveform respectively. This output combined with the template normalization

$$\sigma^2 = (\tilde{h}(f), \tilde{h}(f)) \equiv 4\text{Re} \int_{f_{\text{low}}}^{f_{\text{final}}} \frac{\tilde{h}(f)^* \tilde{h}(f)}{S_n(f)} df \tag{2.13}$$

defines the matched filter SNR, ρ,

$$\rho = \frac{|z|}{\sigma}. \tag{2.14}$$

The ending frequency is typically chosen to be the frequency of the innermost stable circular orbit of the Schwarzschild black hole having the total mass of the binary system. Chapter 4 discusses changing this restriction.

As mentioned before each template in the bank is filtered. Once a local maximum of the filter output is found above some threshold a trigger is recorded. We only allow one trigger to be recorded every 16s *for a single template*, (which is the correlation time of PSD used in the matched filtering.) However since the templates are constructed to be highly correlated (eq. 2.11), a single event may cause threshold crossings in many templates. An additional maximization over the loudest trigger across the template bank for 10ms was done for the S4 PBH search. Figure 2.6 shows the triggers for one LIGO detector after the above described clustering. Table 2.2 shows the key summary information recorded with a trigger. Figure 2.7 shows the histogram of H1 triggers vs SNR.

In Gaussian, stationary noise the signal-to-noise ratio (SNR) given by a matched filter is a sufficient indicator of significance. A trigger is generated when the SNR crosses a set threshold for a given filter and the threshold is directly related to the false alarm probability. The higher the threshold, the more likely it is that a trigger is real. In order to estimate the false alarm probability in LIGO CBC searches consider the definition of SNR, $\rho = |z|/\sigma$. In Gaussian noise $z/\sigma = a + bi$ where each a and b are normally distributed random variables with unity variance (see chapter 6 for proof of this in simplified case that it is real). z^2 is $a^2 + b^2$, which is chi-square distributed with two degrees of freedom and the absolute value of z is therefore chi distributed with 2 degrees of freedom (53). This results in a probability density function for the ρ of a single template which is a Rayleigh function (53)

$$\text{p}(\text{SNR} = \rho) = \rho e^{-\rho^2/2} \, d\rho \tag{2.15}$$

Therefore the probability of getting a single template SNR greater than ρ is

$$\text{P}(\text{SNR} > \rho) = e^{-\rho^2/2} \tag{2.16}$$

Table 2.2: S4 PBH parameters recorded with an example trigger. Other important parameters are derivable from these.

Parameter	Value	Units
end time	793202970.07007	GPS seconds
template duration	7.01479	seconds
effective distance	3.7297	Mpc
coalescence phase	-0.2603	radians
mass 1	0.9193375	solar mass
mass 2	0.5221967	solar mass
final frequency	3050.344	Hz
SNR	16.0550	dimensionless
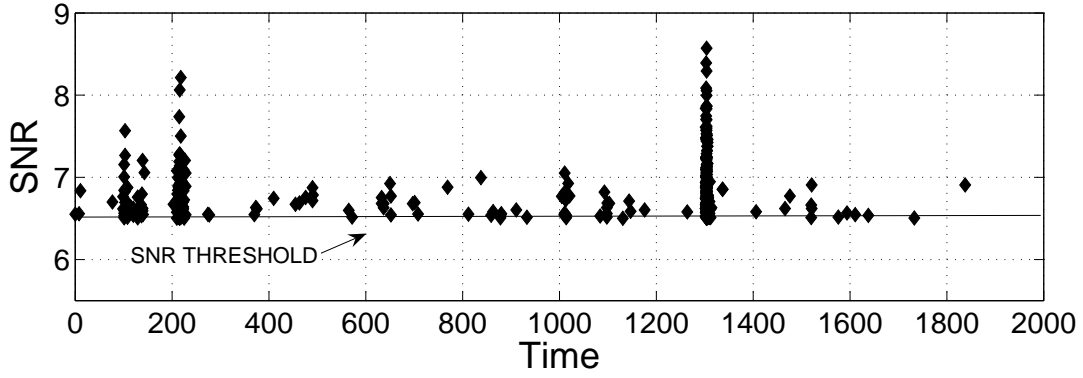
Figure 2.6: Typical S4 PBH SNR vs. time for a single detector.
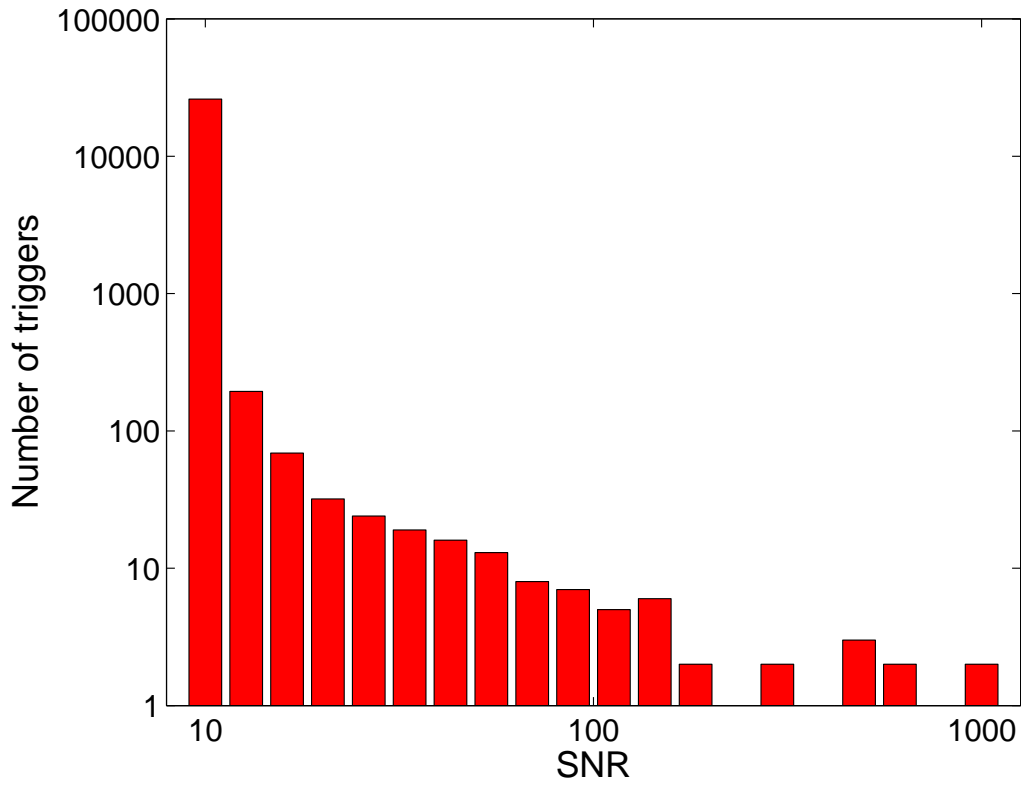
Figure 2.7: Histogram of triggers vs SNR for S4 PBH in H1 only (537 hours of data). Non-stationary noise produces a high number of large SNR false triggers. Our ability to make detections would suffer without coincidence, signal based vetoes and data quality checks described in the next sections.

The probability of obtaining x templates with an SNR greater than ρ out of n trials is (54)

$$P(x; \text{SNR} > \rho, n) = \frac{n!}{x!(n-x)!} e^{-x\rho^2/2}(1 - e^{-\rho^2/2})^{n-x} \qquad (2.17)$$

Now to answer how often a single trial out of n has an SNR greater than ρ we can first evaluate the probability that none of them do and realize that the probability we seek is simply what is left over. In other words the probability that at least one template out of n trials has an SNR greater than ρ is

$$\begin{aligned} P(\text{SNR}_\text{n} > \rho) = 1 - P(0, \text{SNR} > \rho, n) &= (1 - e^{-\rho^2/2})^n & (2.18) \\ &\approx ne^{-\rho^2/2} & (2.19) \end{aligned}$$

Where the last line holds in the limit that $e^{-\rho^2/2} \ll 1$ (or $\rho \gtrsim 3$). This gives the probability that at least one template will have and SNR greater than ρ in n trials of Gaussian noise. The S4 PBH search used 4500 templates[2] in 537 hours of H1 data at 4096Hz sampling rate, which means that the SNR was calculated for $n = 4500 \times 537h \times 3600s/h \times 4096Hz$ trials. The number of triggers above SNR 6.5 for the S4 PBH search in H1 alone is about 24000. This is consistent with the number observed in figure 2.7. However, there should be no triggers above SNR 8 from Gaussian-stationary noise by the above argument. This is clearly not what is observed. Non-stationarity causes the excess number of high SNR triggers.

2.2.4 Stage 4: Coincidence

Once triggers are found in a single detector by matched filtering they are checked for parameter consistency and time delay with triggers from the other detectors; a set of triggers having consistent parameters is considered an event. Requiring coincidence between the triggers of separated detectors lowers the false alarm rates significantly because random noise should be uncorrelated between geographically separated detectors (LHO and LLO are separated by $\sim$ 3000 km). We need to know what to expect of real signals in the pipeline in order to tune our coincidence tolerances. Statistical or systematic errors could cause the observed signal in one detector to have slightly different parameters than the signal observed in another detector. We also want to know what to expect for triggers that are clearly not gravitational-waves in order to reject as many of those triggers as possible during the coincidence stage. The effect of real signals in coincidence is measured by a simulation process known as "injection", and the effect of background triggers is measured by a process called time sliding. Both will be discussed in the following two sub-sections.

2.2.4.1 Measuring Background with Time Slides

In order to estimate the false trigger rate found in coincidence we identify accidental coincidences created when sliding one detector's data set against another in time (which we call time slides) and varying the different coincidence rules. We can then measure how the false trigger rate changes as a function of time and mass coincidence parameters. This gives an accurate false rate since all time shifts are considerably longer than the travel time of a

---

[2]Considering the templates to be independent is reasonable because the bank spans a duration of $\sim$ 18 seconds which means it spans 18*4096 independent points in frequency space (see chapter 6) Thus it only covers $\sim$ 1/18 of the space making it likely that many of them are linearly independent.

gravitational wave between detectors. In the absence of correlated noise this method works well.

Time slides are done over coincident detector time by holding one detector's data set constant and shifting the other data sets by 5 seconds between H1 an L1 and 10 seconds between H1 and H2. In order to obtain reasonable statistics we perform 100 time shifts. In order to keep the time analyzed constant in each shift the slides are done as if they were on a ring (i.e. the data sets are wrapped around from the end to the beginning in order to preserve the length of each time slide). The mean and standard deviation of the 100 time slides give us an estimation of the background. Unfortunately the co-located H1 and H2 detectors have correlated noise and time slides do not sufficiently estimate the background for searches only using H1 and H2.

2.2.4.2 Measuring Detection Efficiency With Injections

The coincidence stage requires simulations to gauge the effects of a real signal in LIGO noise and assess our abilities to make a detection with a given set of parameters. One simulation method, known as hardware injection, is performed by actuating the test mass of LIGO's arms using a specific waveform that is consistent with the expected strain caused by a compact binary inspiral (55). This method provides the most accurate and realistic way to simulate a signal. However, hardware injections reduce the data set available to analyze. It is therefore impractical to gauge the effects of coincidence with hardware injections. The hardware injections serve more to diagnose the instrument than to tune the detection pipeline, though they are useful for the latter as well in some cases such as determining safe methods of vetoing false alarms using auxiliary data channels, since the hardware injections, like real GWs, should only be visible in the GW data channel. If hardware injections influence other channels those channels are not considered to be safe for defining vetoes. See chapter 5 about one way hardware injections can be used. No hardware injections of PBH waveforms were performed during S4. However the search was sensitive to BNS injections and sine-Gaussian waveform injections as is shown in figure 2.8.

The second method of simulating binary inspiral signals is to add waveforms to the data stream as it is read in by the analysis software. Such "software injections" have no effect on the live-time of the detector and can be repeated as many times as necessary within computational time constraints (16). We vary the coincidence criteria and assess how software injections behave in the pipeline as a function of time and mass coincidence. We make every effort to minimize our chance of false dismissal by ensuring that nearly all injections at detectable amplitudes survive coincidence. The ratio of injections found in coincidence to the total number injected gives a detection efficiency. Detection efficiency is key in the astrophysical interpretation of a search as described in the last section of this chapter.

2.2.4.3 Tuning Coincidence Windows

We tune the coincidence thresholds in end time t, chirp mass, $\mathcal{M}$ and symmetric mass ratio, η for the triggers by using software injections and time slides. Chirp mass is defined as

$$\mathcal{M} = \frac{(m_1 \, m_2)^{3/5}}{(m_1 + m_2)^{1/5}} \tag{2.20}$$

In order to tune coincidence windows we histogram the end time difference Δt, chirp mass difference, $\Delta \mathcal{M}$ and symmetric mass ratio difference $\delta \eta$ between detectors for injections and time slides. We then choose thresholds that allow all of our injections to pass while rejecting
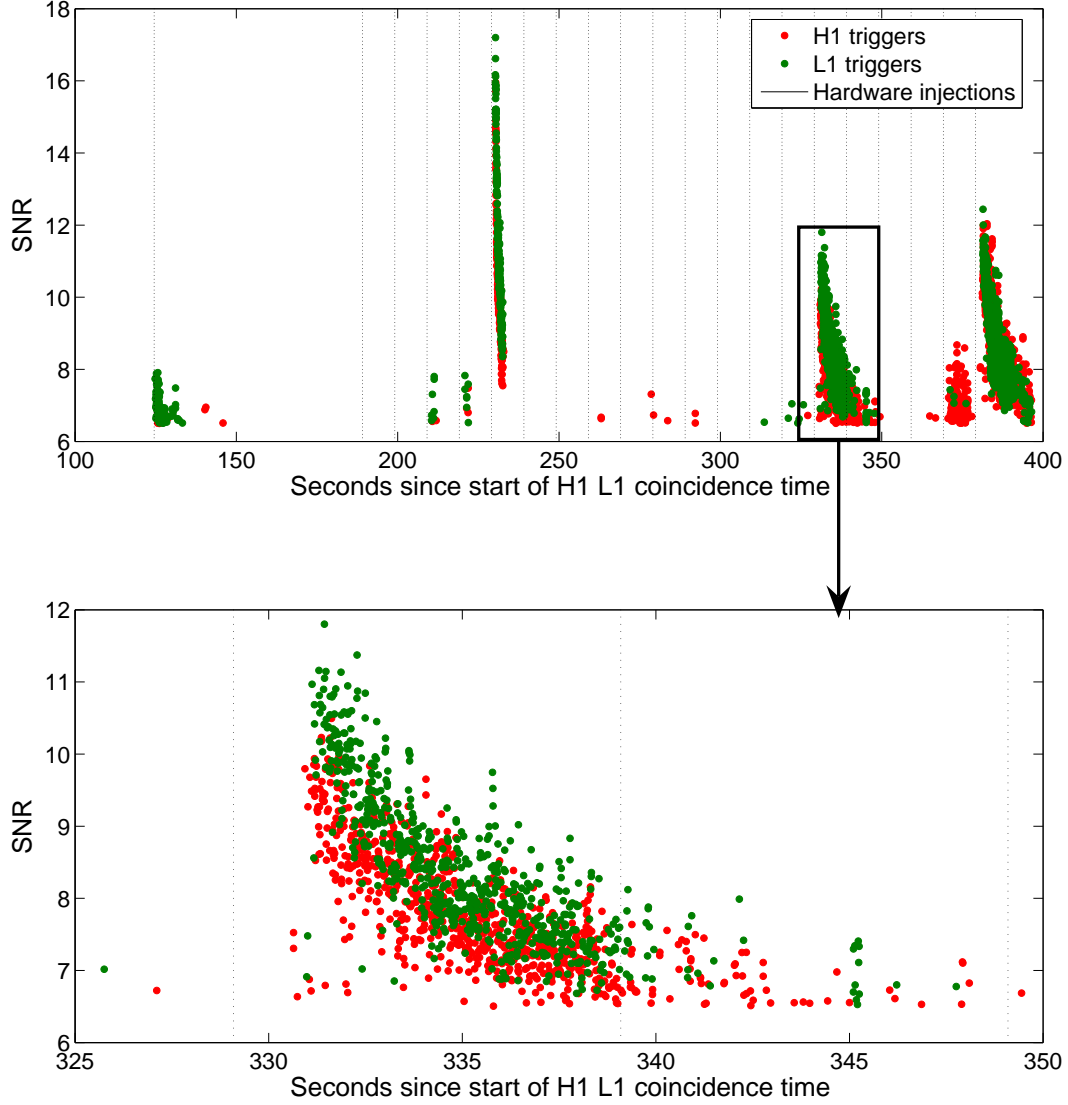
Figure 2.8: S4 PBH Triggers caused by hardware injections (vertical dotted lines) in partially overlapping blocks of H1 (red) and L1 (green) data. These triggers survive the 16s per template maximization and the 10ms template bank maximization. Trigger sets like this proceed to the coincidence stage of the pipeline where they will be compared in time and mass parameters. No PBH waveforms were injected into the detector during S4 (though many software injections were done). The first injection (first dashed line) was a neutron star binary waveform ($1.4\,M_{\odot}$ component mass). Although the PBH search was not intended to detect such signals it did produce some triggers. The remaining hardware injections were sine-Gaussian bursts. The S4 PBH search found some burst injections because they had a very high injected amplitude, but most were not seen. This plot shows how a single glitch could produce multiple triggers.

the largest number of time slides. This method assures that we lower our false trigger rate without effecting our detection efficiency. Figure 2.9 shows these histograms and table 2.3 summarizes the parameters chosen.

Table 2.3: Coincidence windows for the S4 PBH search. Windows are often a function of mass, so other searches are shown for comparison. $\eta = 0.06$ is actually the full range of the template bank. We are therefore not able to distinguish symmetric mass ratio accurately. However chirp mass is known to a high accuracy.

Search	ΔT	$\Delta \mathcal{M}$	$\Delta \eta$
S4 PBH [0.35-1 M$_\odot$]	0.004 s	0.004	0.06
S3 BNS [1-3 M$_\odot$]	0.005 s	0.01	0.10
S4 BNS [1-3 M$_\odot$]	0.005 s	0.01	0.10
S3 PBH [0.35-1 M$_\odot$]	0.004 s	0.004	0.06

The false alarm probability of coincidence is given by the probability that the same template has SNR greater than ρ twice. This is

$$P([\mathrm{SNR_{i,n}}\,,\,\mathrm{SNR_{j,n}}] > \rho) \;=\; n^2 e^{-\rho^2} \qquad (2.21)$$

Coincidence between detectors can happen between different templates, which increases the trial factor again. Assuming that template i can be coincident with m different templates j the probability is (repeating the above analysis)

$$P([\mathrm{SNR_{i,n}}\,,\,\mathrm{SNR_{j,n}}] > \rho) \;=\; mn^2 e^{-\rho^2} \qquad (2.22)$$

In order to estimate the factor m note that the chirp mass half width is 0.004. The 4500 template bank spans 0.57 in chirp mass. Thus as a crude estimate, there are $0.57/.008 = 71$ coincidence "regions" for chirp mass in the bank. The time coincidence regions are fewer because of the 10ms clustering over the bank. About 18ms is allowed for coincidence between sites. This makes the time coincidence trial factor ~ 1.8. The number of trials that arises from coincidence is then roughly $m = 1.8 \times 4500/71 = 114$. This means that the total number of trials in the 576 hours of coincident S4 PBH time is $mn^2 = 576h \times 3600s/h \times 4096Hz \times 4500^2 \times 114$ giving 9 expected triggers above SNR 6.5, with no triggers expected above an SNR of 6.7[3].

2.2.5 Stage 5: Matched Filtering Again, with Signal Based Vetoes

Once a suitable set of coincident triggers is found the next stage is to repeat the matched filtering, *with additional signal processing techniques called signal based vetoes.* These vetoes were too computationally expensive to apply to the template bank produced by the first stage. During this stage a template bank is made from only triggers found in coincidence and is typically 10 times smaller than the original bank as seen in figure 2.5. The filtering stage

---

[3] (42) assumed a different matched filtering prescription and coincidence criteria resulting in a different false alarm rate than what is currently used in LIGO data analysis.
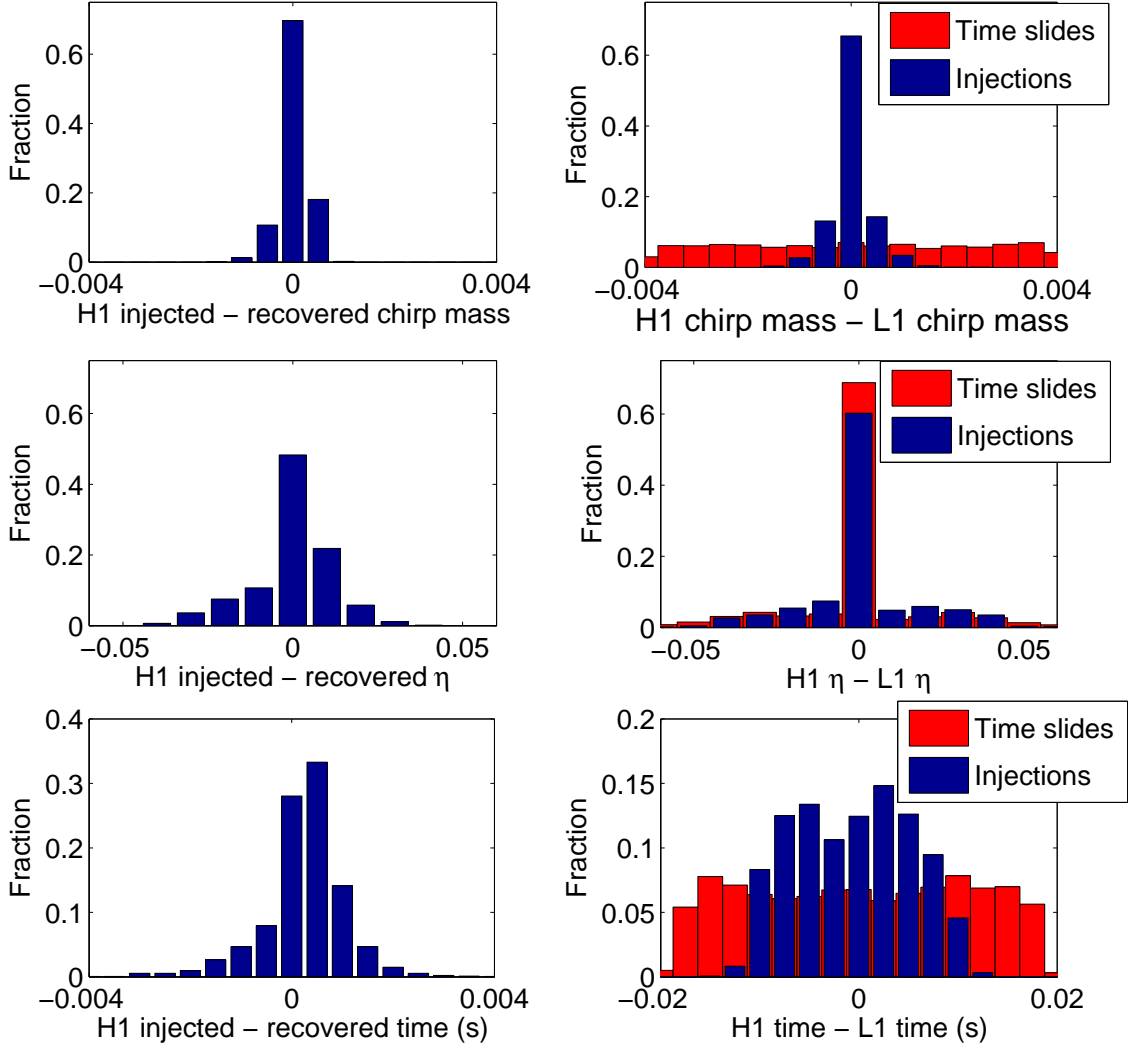
Figure 2.9: S4 PBH parameter difference histograms. Top left: The H1 injections are recovered with accurate chirp mass. Top right: The H1, L1 coincident injections are found with similar chirp mass accuracy. Middle left: The symmetric mass ratio is poorly recovered for H1 injections (the bank only spans 0.18-0.25). Middle right: The symmetric mass ratio found between H1 and L1 is also poor (i.e. it is the same for injections as it is for time slides.) Bottom left: The end time is recovered to within 4ms for H1 injections. Bottom right: The time difference between sites has an extra 10ms possible delay from the GW travel time. Therefore the time difference is roughly 4ms plus the 10ms delay.

is run only on times when coincident triggers were found. The result is that computationally expensive vetoes can be applied without drastically increasing the computational time for the search. I stress again that the need for such tests, and this stage of the pipeline arises purely from the non-stationary characteristics of LIGO noise. Chapter 6 will address new signal based vetoes that are computationally efficient enough to be applied early in the pipeline.

One of the signal based vetoes currently used is the χ^2 waveform consistency test (56; 48) The χ^2 test involves re-filtering each template as a small bank of p sub templates. This would be computationally more expensive than the first matched filtering stage by a factor of p if coincidence did not eliminate many of the templates already.

The χ^2 test establishes how well a signal matches a template by examining its projection onto an orthogonal decomposition of the template (56; 48; 32). If a template, $\tilde{h}(f)$ is normalized, then an orthogonal complete set of p templates $\tilde{h}(f)_i$ will satisfy

$$\langle \tilde{h}(f)_i \,|\, \tilde{h}(f)_j \rangle = \frac{\delta_{ij}}{p} \tag{2.23}$$

$$\sum_{i=1}^{p} \langle \tilde{h}(f)_i \,|\, \tilde{h}(f)_i \rangle = 1. \tag{2.24}$$

A signal that perfectly matches the template $\tilde{h}(f)$ at some SNR ρ would then be expected to have ρ/p SNR in each projection $\tilde{h}(f)_i$. That expectation forms the basis for the χ^2 test which checks the fit of $\Delta\rho_i = \rho_i - \rho/p$ by computing the χ^2 value over a discrete number of bins, p:

$$\chi^2 = p \sum_{i=1}^{p} (\Delta\rho_i)^2. \tag{2.25}$$

In Gaussian noise this test is χ^2 distributed with an expectation value $\langle \chi^2 \rangle = p - 1$. It follows that one would expect a signal in the presence of Gaussian noise to have the same distribution. However the use of a discrete template bank causes a slight mismatch to most *signals* by construction. The mismatch between templates causes the χ^2 test expectation for signals to scale quadratically with SNR (56).

In order to remove the SNR dependence of a signals expectation value we threshold on a quantity ξ defined as

$$\xi = \frac{\chi^2}{p + \rho^2\delta} \tag{2.26}$$

where δ accounts for any possible mismatch and also for the possibility that the real signal does not match the waveform model exactly. Figure 2.10 demonstrates this. δ is tuned so that we do not reject detectable simulated signals. The number of bins p can also be tuned (48). The S4 PBH search used 16 bins.

In addition to providing a hard cut on events that lie above a threshold ξ^*, the χ^2 test also allows for better detection statistics for those below the threshold (16). We have found that an effective SNR defined as

$$\rho_{\text{eff}} = \frac{\rho}{\left[\left(\frac{\chi^2}{2p-2} \right) \left(1 + \frac{\rho^2}{\rho_c} \right) \right]^{1/4}} \tag{2.27}$$

provides far better separation of simulated signals from background noise events than using SNR alone. An example of this is given in figure 2.11.
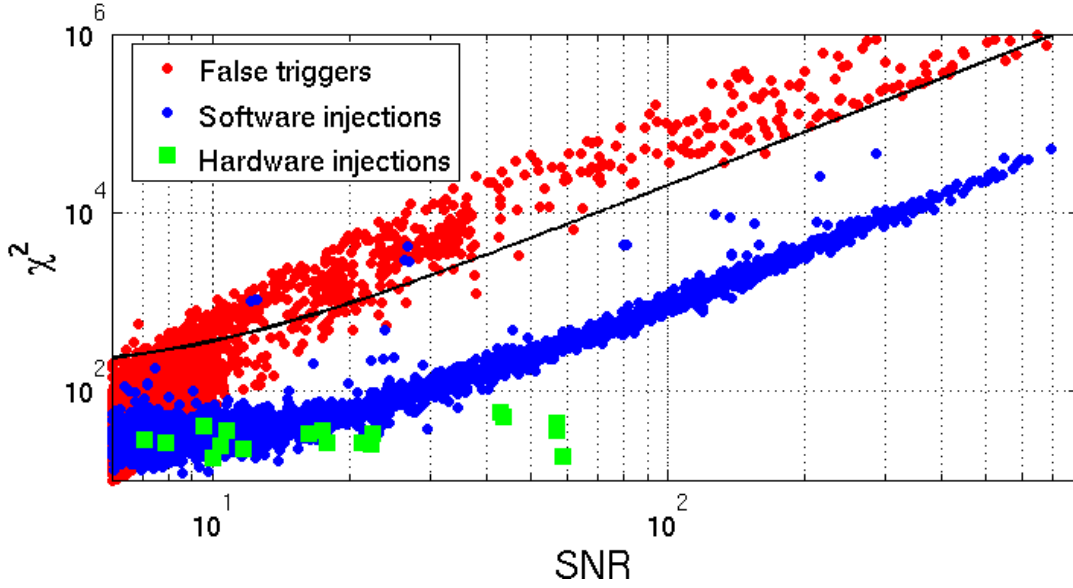
Figure 2.10: χ^2 versus SNR for simulated signals and false triggers. Both simulated signals and false triggers have a χ^2 that scale quadratically in SNR. By transforming to ξ simulated signals lose their SNR dependence making it easy to set a threshold that keeps injections while rejecting false triggers. This is S4 data with a template bank spanning component masses from 1.2-1.6$M_\odot$ because PBH hardware injections were not done. Choosing $\xi^* = 10$ and $\delta = 0.2$ (black line) gives a threshold that keeps most software injections and all hardware injections.
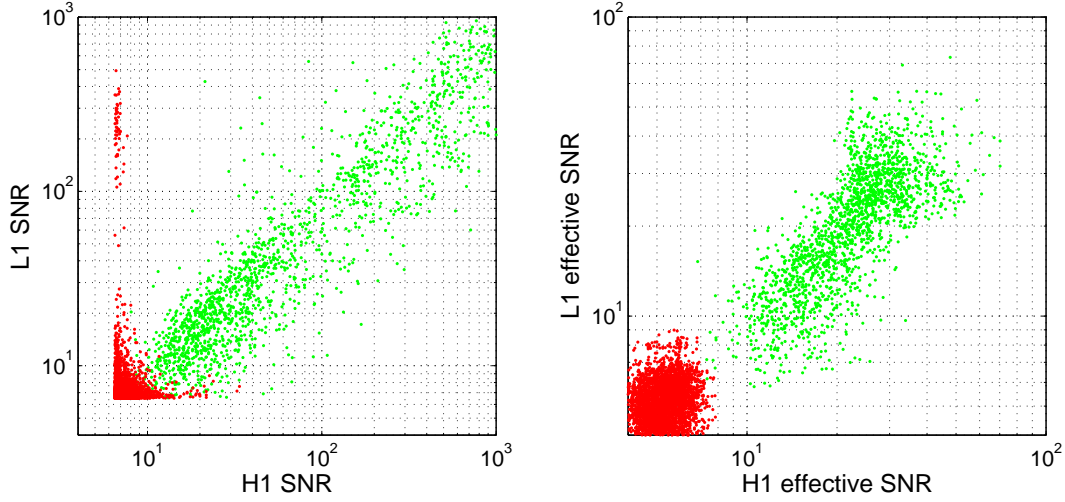
Figure 2.11: Left: S4 PBH H1L1 SNR scatter plot. Right: S4 PBH H1L1 effective SNR scatter plot. False triggers (time slides) are better separated from injections by effective SNR than by the standard matched filtering definition of SNR.

Triggers with a ξ value above some threshold are eliminated at this stage in the pipeline. We choose the value of $\xi*$ and δ to assure that nearly all simulated signals are detected by the pipeline. We tend to choose a very conservative $\xi*$ threshold to assure that real GW events, which undoubtedly will not exactly fit our search templates are not rejected. For example, although we filter the data using waveform templates for non-spinning binaries, we want our pipeline to be sensitive to spinning systems as well. We therefore test our non-spinning detection pipeline with simulated spinning waveforms to choose a $\xi*$ threshold high enough that most spinning systems are not rejected while simultaneously weighing the effects of the higher false alarm rate. For the remaining triggers that pass the χ^2 test, the χ^2 information is still used through the effective SNR.

The χ^2 statistic is calculated as a time series and provides information about the data around a given trigger. Simulations show that an inspiral signal spends less time above the χ^2 threshold in a short window prior to the end time than does a false trigger as shown in figure 2.12. The r^2 test checks the time series $r^2 \equiv \chi^2/p$ for consistency with simulated signals. For the S4 PBH search we found that examining the duration that the r^2 series was above 15 for a 2 second window prior to the end time of a trigger was a powerful discriminator between false triggers and injections. The distribution of is given in figure 2.13.

Triggers that survive the second filtering stage of the pipeline are again checked for coincidence as described in the next section.

2.2.6 Stage 6: Second Coincidence

Triggers that survive the second filtering stage of the pipeline are again checked for coincidence. The procedure is similar to the one described previously. Some additional checks are made however. One test assures that a coincident signal has an amplitude ratio which is consistent with the detectors' sensitivity for the co-located, co-aligned detectors H1 and H2 (48). Spurious noise triggers tend to have inconsistent amplitudes in H1,H2 and are
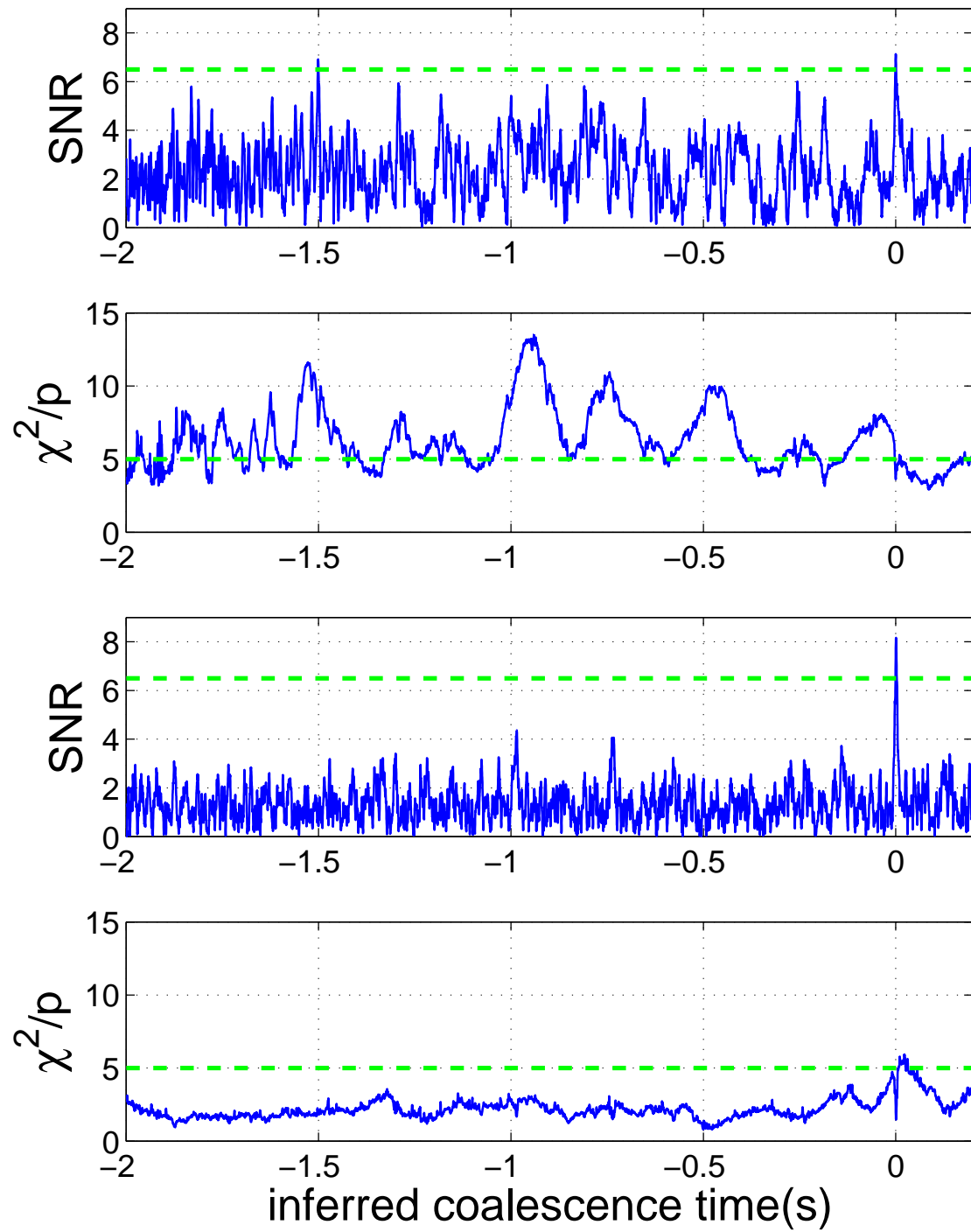
Figure 2.12: SNR and r^2 times series for an injection and a false trigger (courtesy of Andres Rodriguez). An injection spends less time above a given $r^2 = \chi^2/p$ threshold than does a false trigger for some window before the end time (inferred coalescence time) of the signal.
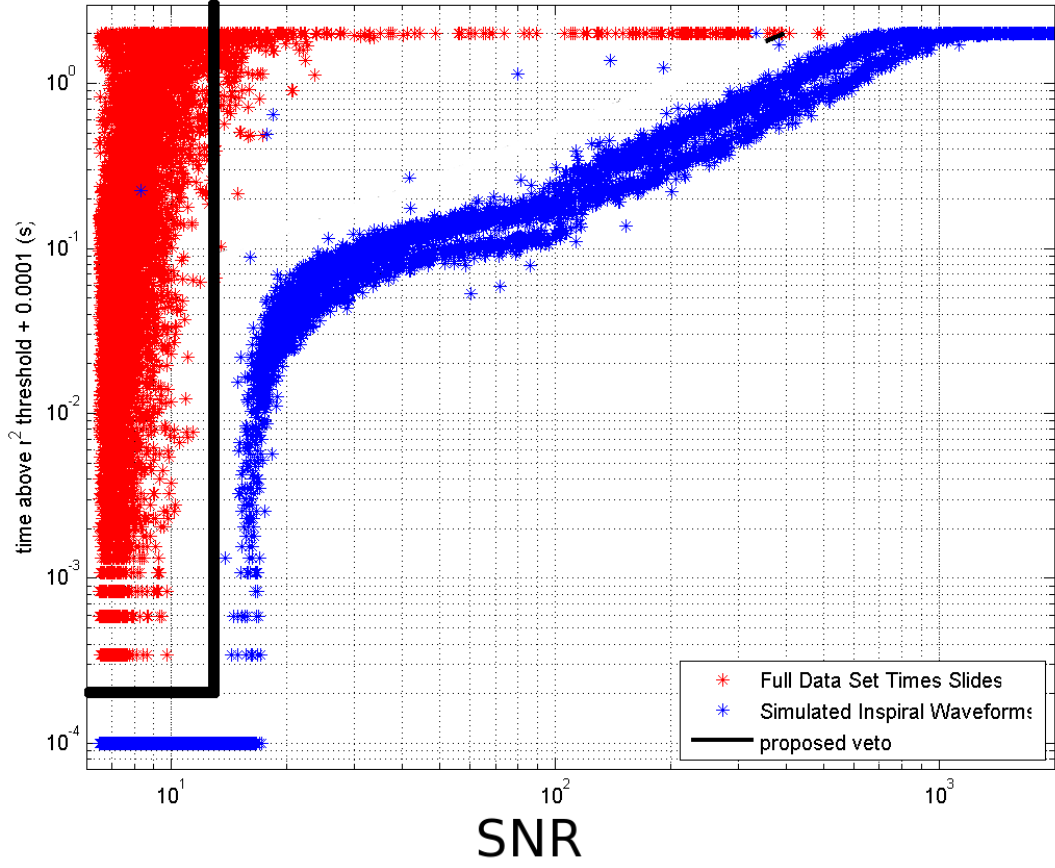
Figure 2.13: Time above r^2 threshold for S4 PBH simulations and time slides (courtesy of Andres Rodriguez). For SNRs below 12 we veto all triggers that have an r^2 above 15 for more than 2ms in a 2s window prior to the end time.
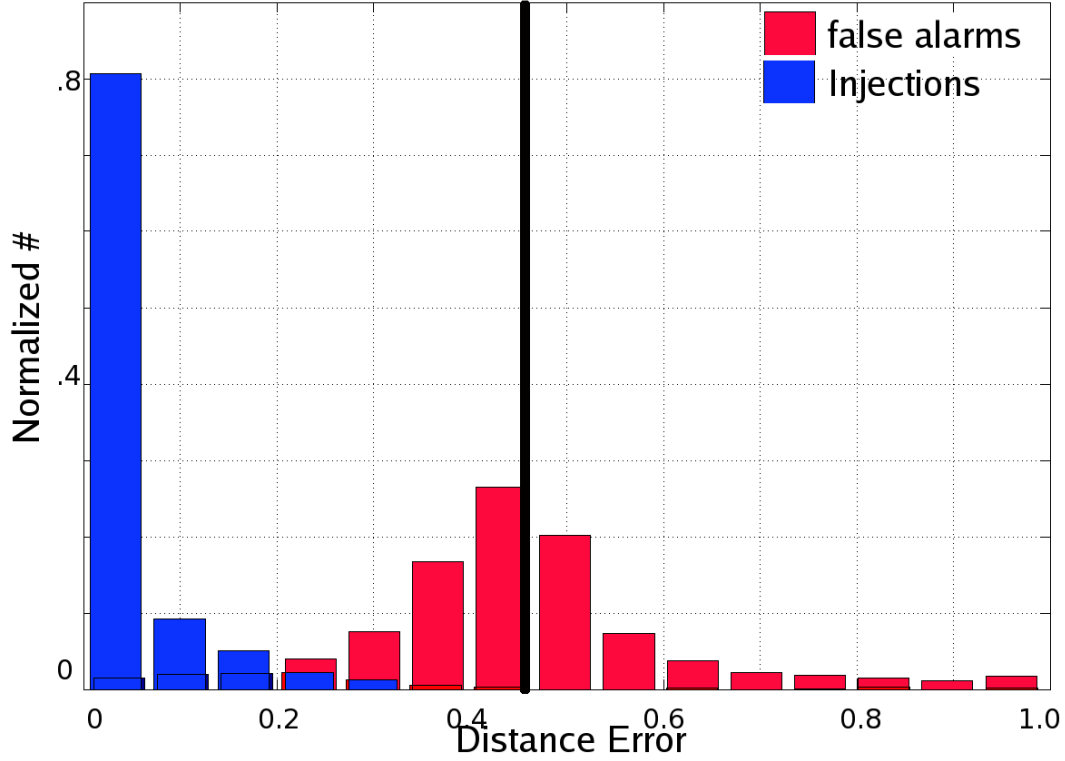
Figure 2.14: S4 PBH effective distance ratio κ for false triggers and injections. Choose a threshold $\kappa = 0.45$ reduces the false triggers while keeping injections.

therefore discounted by this test. For PN templates there is a natural definition of amplitude as an *effective distance* which is the distance at which an optimally oriented binary would be detected with a given SNR.

If an event does not have both an H1 and H2 trigger above the detection threshold then it is still possible to check amplitude consistency between H1 and H2. Knowing the relative sensitivity of both detectors provides an expectation for the relative SNR of a real signal. For example if the relative sensitivity of H1/H2 is 2 then an event that had an SNR in H1 of 20 *should* have an SNR of ~ 10 in H2. If no H2 triggers were found above threshold the confidence of that event being a real signal may be reduced. We set a threshold κ on the quantity,

$$\frac{2|D_{\mathrm{eff,H_1}} - D_{\mathrm{eff,H_2}}|}{D_{\mathrm{eff,H_1}} + D_{\mathrm{eff,H_2}}} < \kappa \tag{2.28}$$

which is tuned by examining the effective distance ratios for false triggers and injections. Figure 2.14 shows the distribution of κ for injections and false triggers. We found that choosing $\kappa = 0.45$ was sufficient (16)

During the second coincidence stage we also check data quality by examining environmental and auxiliary channels in the detectors. Poor data quality generally implies a larger

false alarm rate. A nice summary of the data quality used in S4 can be found in sections 3.6-3.9 of (40) and also in (16). An example of a specific application of data quality checks can be found in chapter 5. Data quality is broken into veto categories. Category 1 data quality is applied before any analysis is done and is the criteria for choosing contiguous data blocks as mentioned before. This category checks basic things such as the status of the detectors (e.g., that they were on and taking science data). Category 2 data quality represents known times of instrumental problems, which are short duration and times where hardware injections were performed. The triggers found in figure 2.8 would be included in this category. These times are short enough that we still desire to analyze data around them and they do not influence PSD estimation or other portions of the analysis pipeline significantly. At this stage triggers found during these category 2 times are vetoed. We also have category 3 and 4 vetoes which are not used in rejecting triggers for the rate upper limit calculations, but are used to follow up candidates. We look for candidates before and after each application of data quality to assure that we do not accidentally reject a plausible signal. It is important that data quality vetoes do not reject too much time, since the loss of science time will adversely effect rate upper limits and may carelessly toss out a real signal. For this reason the tuning of data quality veto windows is an important matter that requires much care. The loss of time caused by data quality vetoes is known as dead-time, t_d and is given in percentage of the time analyzed. A table summarizing data quality vetoes and dead-times is given in table 2.4.

2.2.7 Results

Triggers that survive to the final stage of the pipeline are examined as candidate events. **No plausible gravitational-wave events were found in the S4 PBH search** (16). In figure 2.15 the candidates are histogramed cumulatively as a function of effective SNR squared along with the false triggers found from time slides. We show all combinations together, e.g. H1/L1 candidates, H1/H2 candidates, H2/L1 candidates. No candidates were found in triple coincidence for the S4 PBH search. The mean and standard deviation of the 100 time slides in each bin of effective SNR provides a measure for the significance of the candidate events. The S4 PBH histogram is shown in figure 2.15. This plot shows that the candidate events are consistent with the time slide estimates for background.

2.3 Astrophysical Interpretation

As mentioned in the introduction it is possible to constrain the rate of coalescing compact objects from observations made by LIGO even in the absence of a detection. In order to get a rate upper limit we need a few pieces of information (16; 38; 33):

- The time analyzed, which is a combination of times when two and three detectors were operating.

- The volume of space surveyed: This is actually computed by combining the efficiency to simulated signals – found with an SNR greater than the loudest candidate event of the search – with a galaxy catalog with the blue light luminosity and distance to nearby galaxies. More on the galaxy catalog and motivation for the normalization is given in chapter 3.

- The probability that the loudest event is a false trigger.

Table 2.4: Data quality vetoes and associated dead-times, t_d in % of time analyzed. Category 2 vetoes are used to veto false triggers before the rate upper limit is deduced. Category 3,4 vetoes are used after the rate upper limit to follow up detection candidates (40).

Category 2 Veto	H1 t_d	H2 t_d	L1 t_d
INJECTION_INSPIRAL -inspiral hardware injection	0.54	0.53	0.40
INJECTION_STOCHASTIC - stochastic GW background injection	0.32	0.37	0.61
INJECTION_PULSTART - the start of pulsar GW injection	0.02	0.02	0.006
INJECTION_BURST - burst hardware injection	0.33	0.33	0.30
ADC_OVERFLOW - analog-to-digital converter exceeded its range.	0.11	0.69	0.32
CALIB_LINE_V01 - time of large fluctuations in calibration	0.09	–	0.03
CALIB_LINE_V04_1_SEC - fluctuations of calibration, 1s time scale	0.003	0.04	0.02
CALIB_LINE_DROPOUT - time when calibration signal stopped	0.02	0.03	0.02
CALIB_LINE_SAMPLE_DROP - one sample of calibration missing	0.005	0.005	0.004
SEISMIC_0D4_0D9 - unusually high seismic noise at 0.4-0.9Hz	0.04	0.04	–
SEISMIC_0D9_1D1 - unusually high seismic noise at 0.9-1.1Hz	0.70	0.61	–
SEISMIC_1D8_2D4 - unusually high seismic noise at 1.9-2.4Hz	0.04	0.04	–
SEISMIC_2_20 - unusually high seismic noise at 2-20Hz	0.017	0.29	0.09
H1UP_H2UNLOCKED - time when H1 was locked but H2 was not; stray light from H2 causes transients	5.80	–	–
H2UP_H1UNLOCKED - time when H2 was locked but H1 was not; stray light from H1 causes transients	–	3.23	–
JET - jet airplane overhead	0.01	0.01	–
KW VETOES – correlations with auxiliary channels (see chapter 5)	0.03	0.008	–
Total dead-time incurred:	8.1	6.0	1.8
Category 3 Veto	H1 t_d	H2 t_d	L1 t_d
LIGHTDIP_04PERCENT - light power in arm dropped 4%	0.01	–	–
LIGHTDIP_05PERCENT - light power in arm dropped 5%	–	0.61	0.71
LIGHTDIP_06PERCENT - light power in arm dropped 6%	0.26	–	–
LIGHTDIP_07PERCENT - light power in arm dropped 7%	–	–	0.67
ASDC_MIDDLE_THRESH - excess power at anti-symmetric port	0.11	–	0.27
ASDC_HIGH_THRESH - excess power at anti-symmetric port	0.02	–	0.035
ASI_KW_VETO - ASI veto (see chapter 5)	0.5	–	2.3
DUST_HIGH - excess dust on optics table	4.51	–	–
HIGH_PIXEL_FRACTION_2KHZ - excess 2Khz time-freq. pixels	1.01	–	–
Total Cat 3:	5.9	0.61	2.86
Category 4 Veto	H1 t_d	H2 t_d	L1 t_d
ASDC_LOW_THRESH - excess power at anti-symmetric port	0.85	–	1.63
HIGH_PIXEL_FRACTION_1KHZ - excess 1KHz time-freq. pixels	1.67	4.23	2.52
ACOUSTIC_ELEVATED - excess acoustic noise measured	4.01	–	9.19
DUST_ELEVATED - excess dust on optics table	12.89	10.75	–
SEISMIC_0D8_2D0 - unusually high seismic noise at 0.8-2.0Hz	–	6.01	4.79
WIND_OVER_30MPH - wind speed over 30 MPH	–	0.77	–
Total Cat 4:	18.0	16.8	16.2
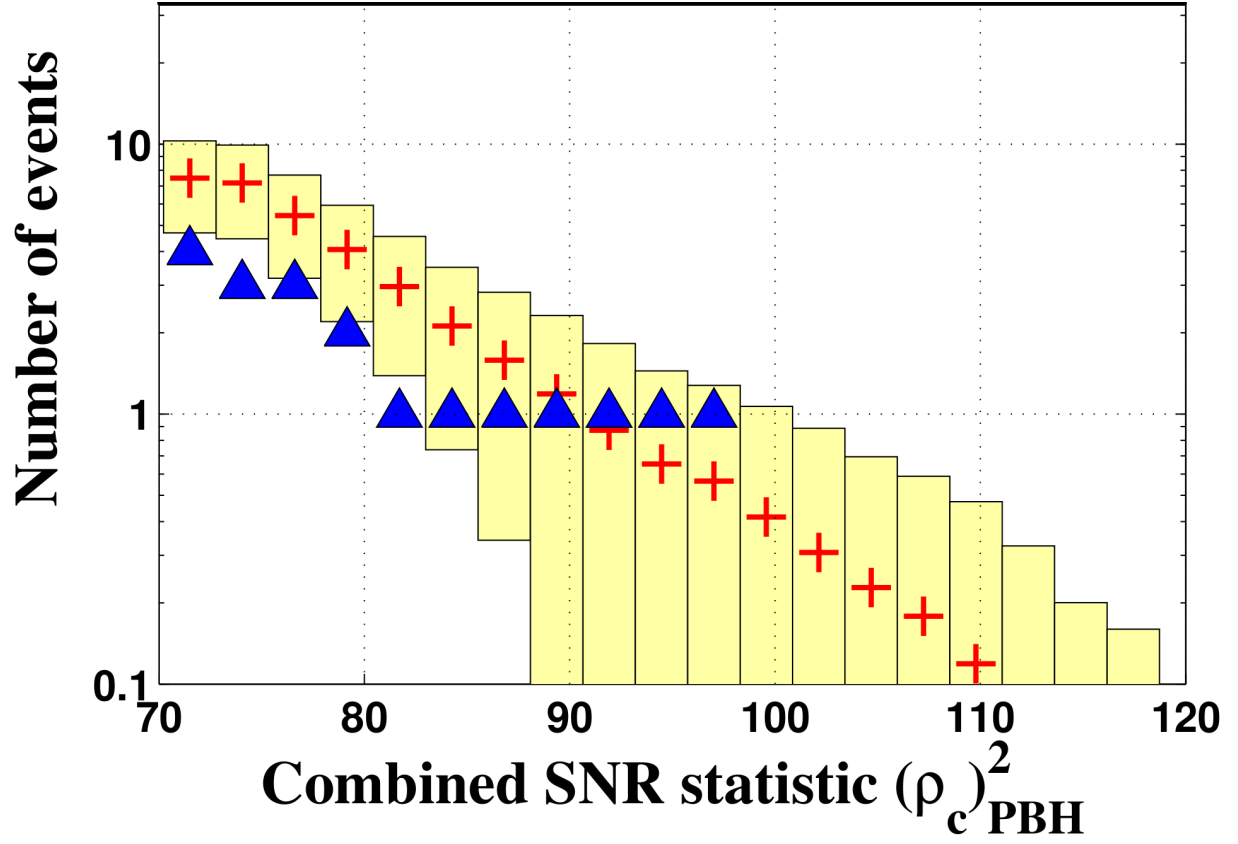
Figure 2.15: Cumulative histogram of candidate events for the S4 PBH search after category 2 vetoes. The candidate events are consistent with the false triggers found by performing time shifts. No plausible gravitational-wave candidates were found.

From this information we can compute the upper limit of PBH rates set by the analysis of the S4 data set using the following expression (16; 33),

$$1 - \alpha \;=\; e^{-RTC_L} \left[1 + RTC_L(\rho^*) \left(\frac{1 + \Lambda}{\Lambda} \right) \right] \tag{2.29}$$

$$\Lambda \;=\; \frac{C_L(\rho^*) \, C_L(\rho^*)'}{P_B(\rho^*) \, P_B(\rho^*)'} \tag{2.30}$$

where α is the confidence level (e.g. at 90% confidence it is 0.9), R is the rate we are solving for, T is the time analyzed, C_L is the cumulative blue luminosity available to the search and P_B is the probability that the loudest event is a false trigger.

In order to compute the cumulative luminosity we need to know the efficiency of the S4 PBH search to simulated signals as a function of distance. This is done by counting the number of simulated signals found above the loudest event snr, ρ^* in a given distance bin and dividing it by the total number of injections made. In a previous analysis (48) we injected signals from a population model (i.e., we recreated the parameters from a population of binary inspirals expected in galaxies with a rate proportional to the galaxy's blue luminosity (34).) However, efficiency can be evaluated purely as a function of effective distance and mass allowing the selection effects of a real population to be analyzed *post facto* (34). Therefore, we developed a more general injection strategy than the one used for S2; We chose to inject signals in a manner that adequately spanned the science run and covered a broad parameter space. This was done by injecting signals which were uniform across the sky, uniform in distance (or log distance), uniform in mass, and not associated with any one galaxy. Real population considerations were used to derive upper limits on astrophysical rates from measured efficiencies per unit distance (38; 34). Since the search is sensitive to the effective distance mentioned earlier it is useful to calculate the efficiency that way. The efficiency is also calculated as a function of mass. By converting the galaxy catalog into effective distances (see chapter 3) the efficiency and blue light luminosity can both be evaluated as a function of effective distance. The integral over the product of blue light luminosity and efficiency provides the cumulative luminosity C_L. An example of the cumulative luminosity and efficiency as a function of H1 and L1 effective distance is shown in figure 2.16.

The cumulative luminosity can be computed while varying the loudest event (33), which changes the efficiency. Having the cumulative luminosity as a function of ρ^* is necessary for computing Λ which requires the derivative of the cumulative luminosity with respect to ρ^*. The probability that the event is caused by a false trigger is also required. In order to obtain this value we compute the loudest events found in the 100 time slides. The histogram of this gives a probability density that a given loudest event is caused by a false trigger background. The background probability density and probability are given in figure 2.17.

The culmination of all of this work leads to a rate upper limit for the S4 PBH search calculated as a function of total mass given by figure 2.18. The statistical and systematic errors have been analyzed and the upper limit marginalized over those errors is also presented. For a nice description of the errors see (33; 34).

2.4 Conclusion

The non-stationary characteristics of LIGO noise require a complicated analysis pipeline in order to detect the inspiral and merger of compact objects. This pipeline is based on matched filtering, which is capable of detecting weak signals, but easily effected by noise transients. In order to reduce the level of false triggers coincidence is required between sites
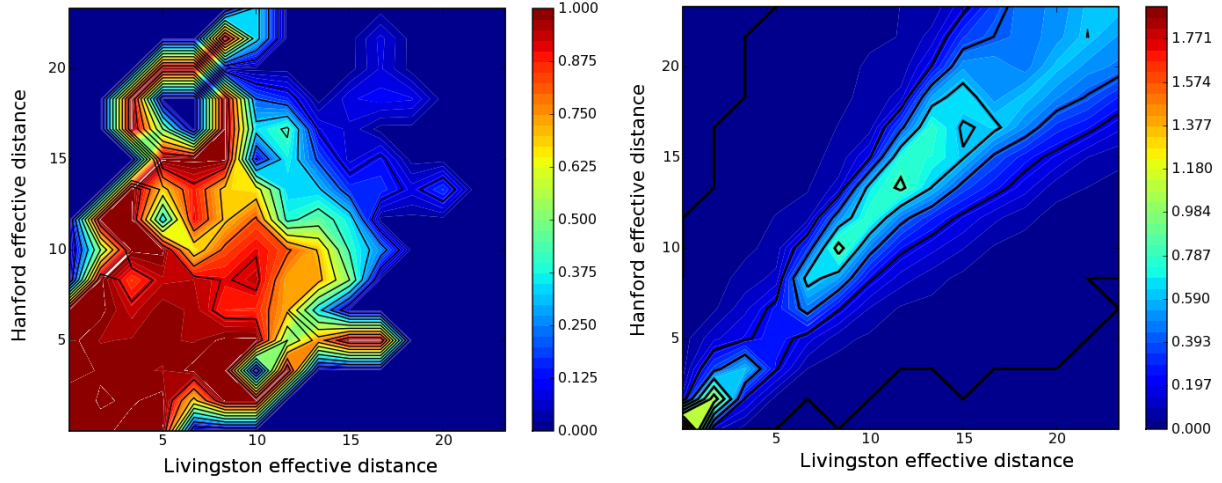
Figure 2.16: Left: S4 PBH efficiency vs effective distance in Hanford and Livingston sites. The efficiency depends on mass and has been normalized to a 1.4, 1.4 $M_\odot$ system in this plot (we use this as a canonical mass for the PBH and BNS searches in order to make direct comparisons that are less waveform dependent). The product of the efficiency and blue light luminosity obtained from a galaxy catalog is integrated over effective distance in order to obtain the cumulative luminosity C_L. Right:S4PBH luminosity density vs effective distance. The distance and blue light luminosity from a galaxy catalog (34) is binned up into effective distance bins for the Hanford and Livingston detectors. This luminosity density is integrated with the efficiency to produce the cumulative blue luminosity available to the search C_L.
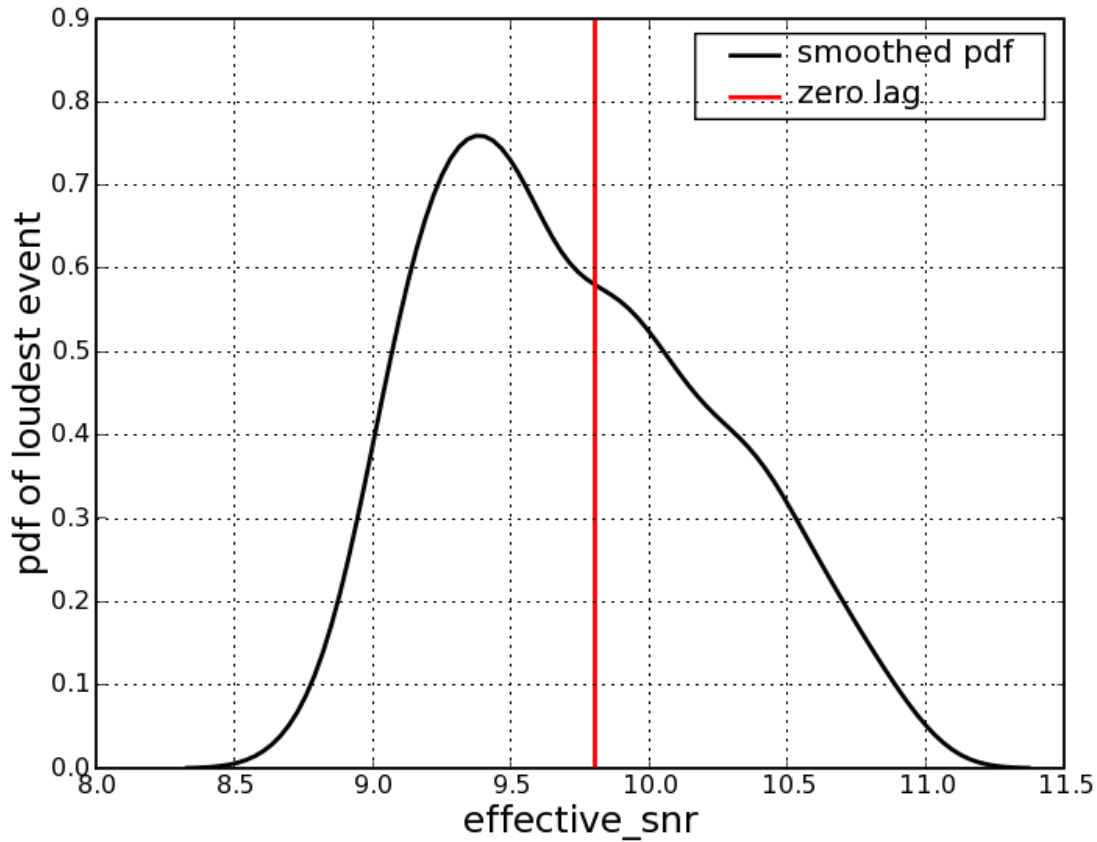
Figure 2.17: S4 PBH probability density that the loudest event was a false trigger. By histograming the loudest event from 100 time slides we obtain a probability density function that when integrated can give the probability that an event was a false trigger. The "zero lag" loudest event (the one from the truly coincident data that is a candidate event) is shown as a red line. About 35% of the time slides had a loudest event greater than the one found in the S4 PBH search. The pdf and probability are both required for the upper limit calculation.
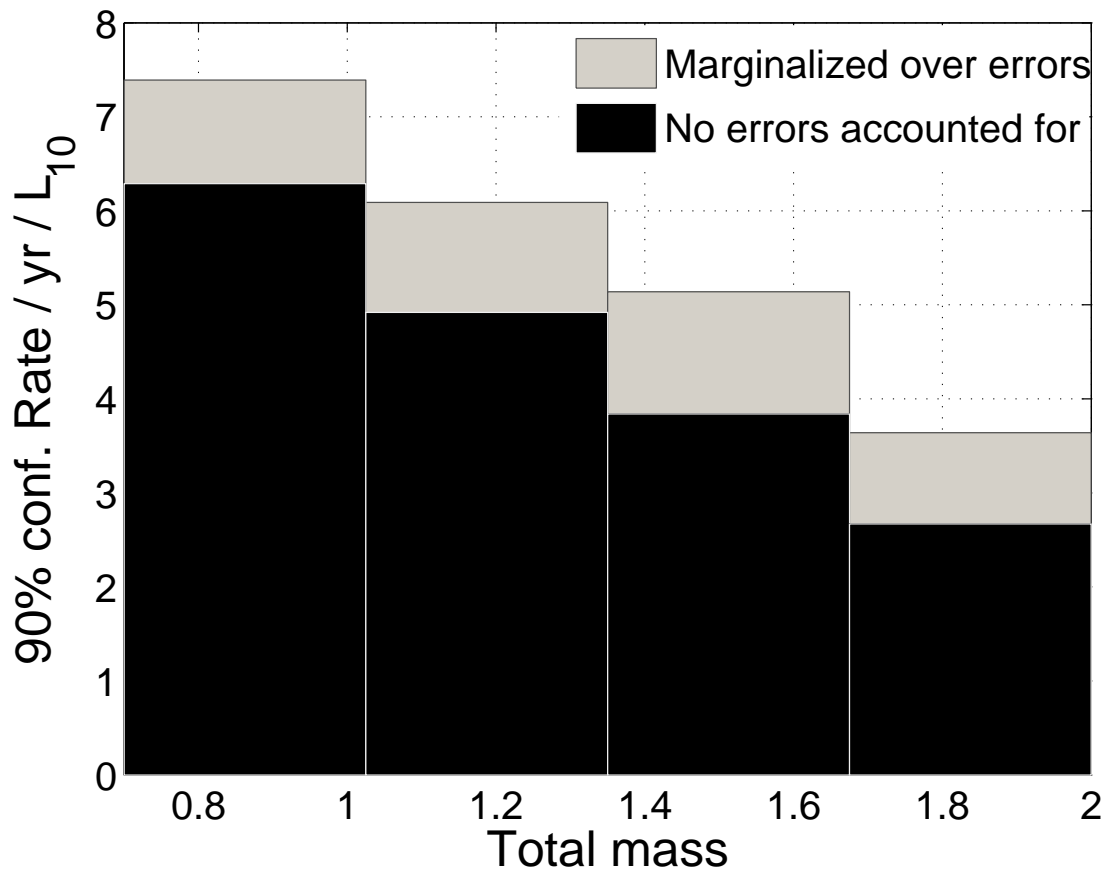
Figure 2.18: S4PBH rate upper limit at 90% confidence as a function of total mass. This calculation is based on the cumulative luminosity and approximately 576 hours of analyzed data. This rate is still significantly higher than the expected rates for neutron star or black hole mergers derived from other methods (16). Increased sensitivity and observation time will some day make LIGO the most sensitive instrument for establishing these rates.

for any candidate events. Additionally more powerful signal processing tools, called signal based vetoes, are used to reject false triggers.

The result of the pipeline is a list of candidate events. No plausible gravitational-waves were found for the S4 PBH search. The search can be used to establish a rate upper limit. This requires the evaluation of the detection efficiency through simulated signals, called injections. The efficiency gives a notion of the volume of space that the search is sensitive too. By integrating the efficiency with a galaxy catalog of nearby galaxies it is possible to assess the cumulative blue luminosity that the S4 PBH search is sensitive to. The assumption that binary populations scale with the blue luminosity of a galaxy is used to derive an upper limit for the S4 PBH search that is 4.9 yr^{-1} L_{10}^{-1} for a {0.75, 0.75} pair.

3. Host Galaxies Catalog Used in LIGO Searches for Compact Binary Coalescence Events [1]

3.1 Introduction

The previous chapter discussed a search for compact binary coalescence with LIGO data. The result was that in the absence of a detection it was still possible to set an upper limit on the merger rates. This chapter describes an important part of the upper limit calculation - calculating the expected population of binary mergers based on a catalog of nearby galaxies.

The LSC science runs S3, S4 and S5 have reached significant extragalactic distances (16) into the nearby Universe - beyond the Virgo Cluster. To interpret the results of the searches for signals from compact binary coalescence it is necessary to use information about the compact object populations in the nearby galaxies, as well as how the population scales at larger distances. The nearby galaxy catalog discussed here represents the distribution of such extragalactic populations, and the procedures described are used for LIGO data analysis, such as assigning an astrophysically meaningful upper limits to the rate of coalescing systems in the Universe, in a search that did not yield a detection as was done in chapter 2. An accurate upper-limit that correctly incorporates our best information about galaxy distributions requires a model of the nearby overdense region because the current LIGO network's range probes this overdensity.

Binary compact objects are usually produced from the evolution of massive stellar binaries. Since short-lived, massive stars emit more blue light than all other stars in a galaxy combined, blue light is a well-known tracer of star formation in general and the birthrate of these massive stars in particular. Given the short lifetimes of the known Milky Way double compact object population and the slow rate of change in star formation expected in nearby and distant galaxies, Phinney (58) has argued that a galaxy's blue luminosity should linearly scale with its compact binary coalescence rate, although more sophisticated normalizations exist (34).

The sensitivity of LIGO to compact binary coalescence signals depends on the distance and sky position of the coalescing binary system and therefore, the distribution of known nearby galaxies in blue luminosity and in space is the minimum information needed to properly interpret searches of the LIGO data sets.

We have used mostly publicly available astronomical catalogs of galaxies to compile a catalog used in the analysis of S3, S4 and S5 LIGO data. We discuss the methodology used to compile this galaxy catalog and briefly describe how this information feeds into LIGO rate estimates. In §3.2, we describe all the elements involved in compiling the galaxy catalog and assessing the relevant errors and uncertainties. In §3.3, we derive a correction factor to account for incompleteness in the catalog guided also by the blue-light volume density estimated from the Sloan Digital Sky Survey and earlier surveys. In §3.4, we discuss how the corrected catalog and resulting blue light distribution as a function of distance is used to bound the rate of compact binary coalescence using data from the recent LIGO science runs. If the maximum distance to which a search could detect a compact binary coalescence is known, then the expected number of detectable events can be derived.

---

[1]Reprinted by permission of the AAS (34).

3.2 Compilation of Galaxy Catalog

We have compiled a catalog[2], the *compact binary coalescence galaxy* catalog or CBCG-catalog, of nearby galaxies which could host compact binary systems. For each galaxy out to 100 Mpc, the catalog provides the equatorial coordinates, distance to the galaxy, and the blue luminosity corrected for absorption. Estimates of the errors on distance and luminosity are also provided.

The CBCG-catalog is compiled from information provided in the following four astronomical catalogs: (i) the Hubble Space Telescope (HST) key project catalog used to measure the Hubble constant (64), (ii) Mateo's dwarf galaxies of the local group catalog (65), (iii) the HyperLeda (LEDA) database of galaxies (66), and (iv) an updated version of the Tully Nearby Galaxy Catalog (67).

When combining these catalogs, distances and luminosities reported in the HST, Mateo and Tully catalogs were generally adopted over those in the LEDA catalog. This is because these catalogs use accurate distance determination methods compared to LEDA. Nevertheless, LEDA served as the baseline for comparisons in the range 10-100 Mpc since it is the most complete.

3.2.1 Distances

One of the primary objectives of the HST key project was to discover Cepheid variables (stars which have periodic variations in brightness) in several nearby spiral galaxies and measure their distances accurately using the period-luminosity relation for Cepheids. Cepheid distance determination to nearby galaxies is one of the most important and accurate primary distance indicators. The distance information from the HST key project is considered to be the most accurate in the CBCG-catalog; there are 30 galaxies in our catalog for which we adopt distances from the HST key project.

Mateo's review (65) of properties of the dwarf galaxies in the Local Group provides distance and luminosity information for each galaxy considered. Since the parameters in this catalog were derived from focused studies on each individual galaxy, we consider it the most accurate next to the HST measurements for nearby galaxies. Moreover it has reasonably comprehensive information on the Local Group's dwarf galaxies; there are 18 sources in the CBCG-catalog which adopt distances (and luminosities) from Mateo's compilation.

It becomes increasingly difficult to use primary distance estimators like Cepheid stars in more distant galaxies. Therefore secondary distance methods are used to measure larger distances. Tully's catalog has up to three types of distances for each source: (i)*Quality distance* (D_{Q}) is based on either Cepheid measurements, surface brightness fluctuations, or the tip of the red giant branch. There are 409 galaxies with such a distance in the CBCG-catalog. (ii) *HI luminosity-line-width* distances (D_{HI}) are obtained from the Tully-Fisher relation, where the maximum rotational velocity of a galaxy (measured by the Doppler broadening of the 21-cm radio emission line of neutral hydrogen) is correlated with the luminosity (in B, R, I and H bands) to find the distances. There are 553 galaxies in the catalog with such a distance. (iii) *Model distance* (D_{M}) is derived from an evolved dynamical mass model that translates galaxy radial velocities into distances. This model is an update of the least action model described by (68) and takes into account the deviations from a perfect Hubble flow due to a spherically symmetric distribution of mass centered on the Virgo Cluster. All galaxies have a calculated model distance. Whenever available, D_{Q}

---

[2]http://www.lsc-group.phys.uwm.edu/cgi-bin/cvs/viewcvs.cgi/lalapps/src/
inspiral/inspsrcs100Mpc.errors?cvsroot=lscsoft

distances are the most preferred due to their smaller uncertainties, then the D_{HI} followed by D_{M}.

The remaining galaxies come from LEDA which does not provide distances explicitly, but instead provides measured radial velocities corrected for in-fall of the Local Group towards the Virgo cluster (v_{vir}). We obtain the LEDA distance (D_{L}) using Hubble's law with the Hubble constant $H_0 = 73\,\mathrm{km\,s^{-1}\,Mpc^{-1}}$ reported by (69). Although corrections to the recessional velocity were made, this method of calculating distances is still highly uncertain. Hence, we use Hubble's law to evaluate the distances only to the galaxies for which $v_{\mathrm{vir}} \geq 500$ km/s (7Mpc) when peculiar velocities are expected to be more of a perturbation.

The error in a distance depends strongly on the method used to measure that distance. The HST sources, though a small contribution to the galaxy catalog, have the smallest errors ($< 10\%$) (64). The three different distance methods in Tully's catalog have different errors. D_{Q} also has a low error (10%) followed by the D_{HI} (20%). To obtain an estimate for the errors of D_{M}, we compare them with D_{Q} for the set of galaxies that have both types of distance estimates. The best Gaussian fit (see Fig. 3.1) to the logarithm of fractional errors has a one sigma width of 0.24 which when subtracted in quadrature with D_{Q} error gives, 0.22 distance error associated with D_{M} (see appendix 7).

Because errors in v_{vir} are not given in LEDA, we follow a similar procedure to find LEDA distance errors, D_{L}. We compare the calculated D_{L} with D_{Q} for galaxies in both catalogs to obtain uncertainty estimates in D_{L}. The plot in Fig. 3.2 shows the best fit Gaussian to the logarithm of fractional errors with a one sigma width of 0.27 which, subtracted in quadrature with D_{Q} distance errors, gives a total distance error 0.25.[3]

3.2.2 Blue Luminosities

The distribution of binary compact objects in the nearby universe is expected to follow the star formation in the universe and a measure of star formation is the blue luminosity of galaxies corrected for dust extinction and reddening (58). Hence, for each galaxy, we calculate the blue luminosity L_{B} from the absolute blue magnitude of the galaxy M_{B} (corrected for internal and Galactic extinctions). For convenience, blue luminosity is provided in units of $L_{10} \equiv 10^{10} L_{\mathrm{B},\odot}$, where $L_{\mathrm{B},\odot} = 2.16 \times 10^{33}$ ergs/s is the blue solar luminosity derived from the blue solar magnitude $M_{\mathrm{B},\odot} = 5.48$ (70). We do not consider galaxies with luminosities less than $10^{-3} L_{10}$ because they do not contribute significantly to the total luminosity – see §3.3.

The Mateo, Tully and LEDA catalogs provide information on apparent B-magnitudes corrected for extinction. The galaxies in the HST key project catalog have only distance information, so for those we extract the corresponding apparent magnitude values (m_{B}, corrected for internal and Galactic extinction) in the B-band from the Tully catalog to find M_{B}. Table 3.1 summarizes relevant properties of each of these catalogs and the fraction of the total luminosity within 100 Mpc that each contributes. The LEDA database quotes uncertainties in apparent magnitude. Figure 3.3 shows the distribution of LEDA assigned apparent magnitude variances for the galaxies in the CBCG-catalog. The RMS error is $\Delta m_B = 0.42$. Galaxies from Tully's catalog have a smaller observational error $\Delta m_{\mathrm{B}} = 0.30$ (67).

---

[3]For searches of the S3 and S4 LIGO data (16) with smaller ranges, a more conservative uncertainty of 40% was used for LEDA distances.
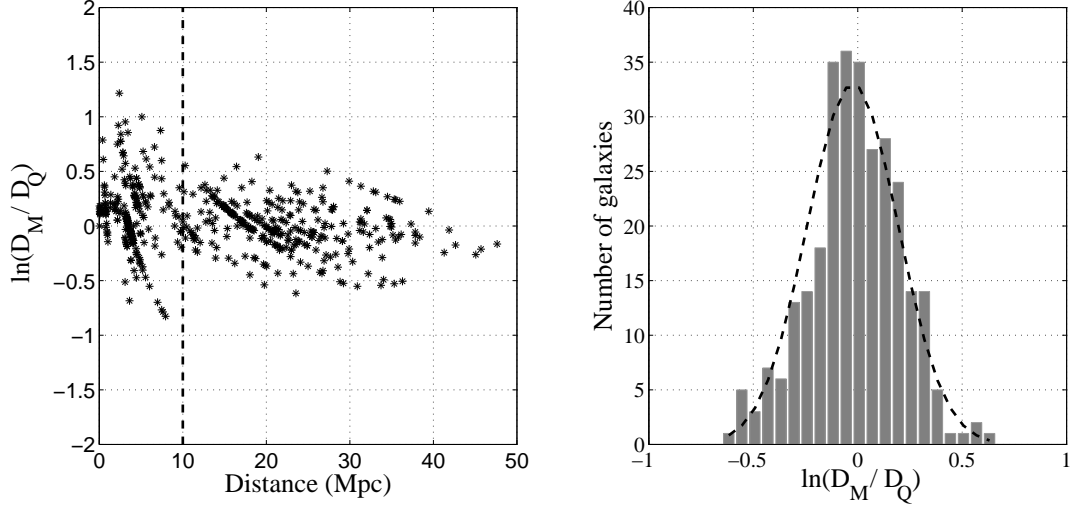
Figure 3.1: In order to obtain reasonable estimates for Tully's model distances we compare galaxies that have values for both. We only consider galaxies beyond 10 Mpc since model distances and LEDA distances are not reliable below this value. All galaxies below 10 Mpc have better distance estimates. The Tully quality distance has roughly a 0.1 logarithmic error. The best fit Gaussian for $\ln[D_M/D_Q]$ implies a fractional error σ of 0.24 in log. Subtracting these uncertainties in quadrature gives an error of 0.22 for Tully model distances.
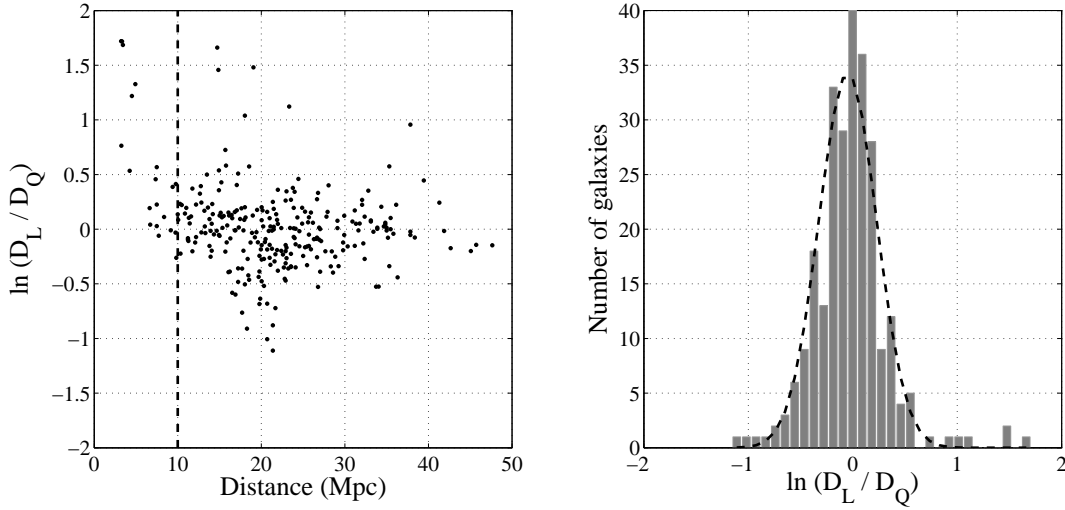
Figure 3.2: Fractional error analysis as in Fig. 3.1 for LEDA distances. By comparing the fractional error between LEDA distances and Tully we obtain a ~ 0.25 log distance error for LEDA.
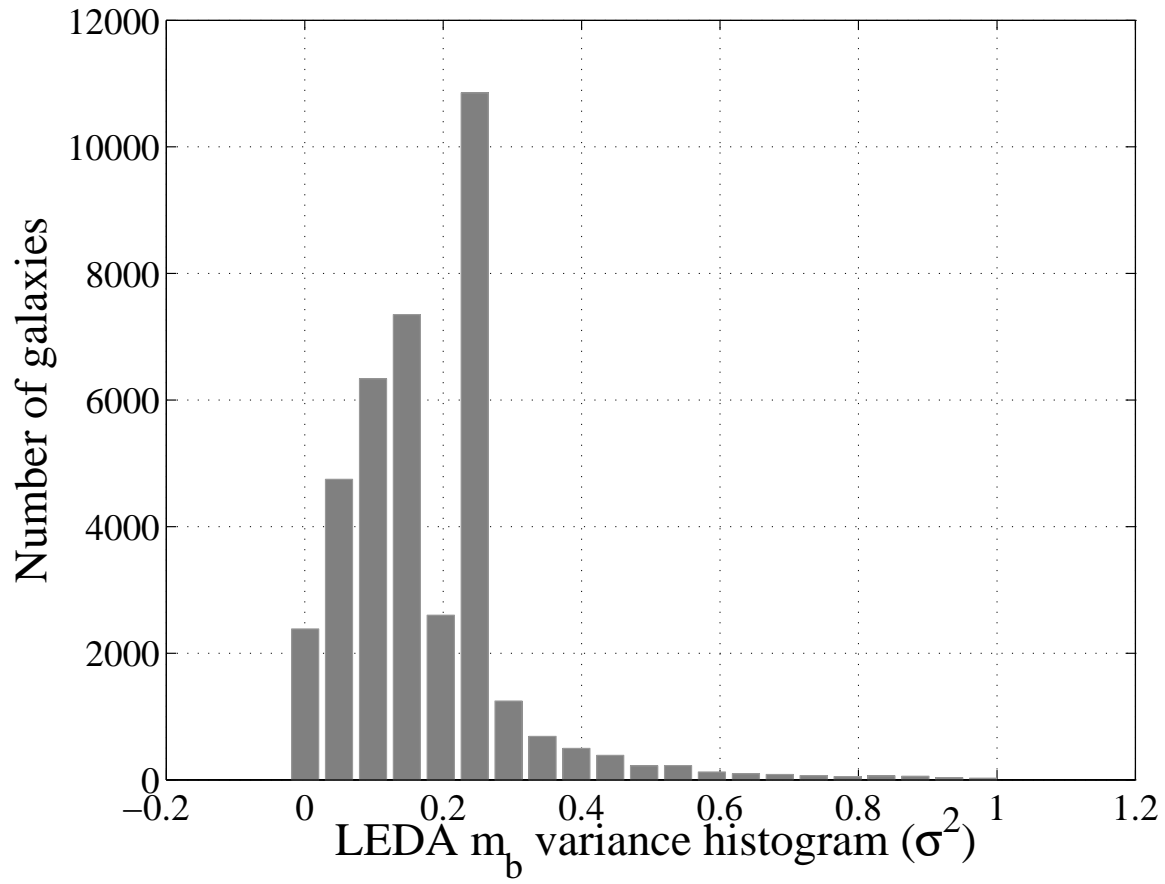
Figure 3.3: LEDA provides uncertainties in apparent magnitudes. The histogram above shows the m_b variance distribution for each LEDA galaxy. The RMS error is 0.42.

Table 3.1: Summary information about the four astronomical catalogs used to develop the CBCG-catalog. We report the number of galaxies for which the catalog was the primary reference and fraction of the total CBCG-catalog blue luminosity accounted for by those galaxies.

	Catalog	# of galaxies	L_{10} $(10^{10}L_{\mathrm{B},\odot})$	Fractional luminosity	Reference
(i)	HST	30	57.3	0.1%	(64)
(ii)	Mateo	18	0.4	<0.001%	(65)
(iii)	Tully	1968	2390	5.3%	(67)
(iv)	LEDA	36741	42969.4	94.6%	(66)
	Total	38757	45417.1	100.0%	

3.3 Completeness

Observations of faint galaxies are difficult even in the nearby universe and lead to systematic incompleteness in galaxy catalogs. Studies of galaxy luminosity functions can provide insight into how many galaxies are missing from a catalog (and hence the corresponding blue luminosity). Using the CBCG-catalog, we can generate a luminosity function $N(L, D)$ which is the number of galaxies with luminosities within a luminosity bin from L to $L + \Delta L$ normalized to the spherical volume within radius D. Specifically, we write

$$N(L, D)\Delta L = \left(\frac{3}{4\pi D^3}\right)\left[\sum_j l_j\right]$$ (3.1)

where

$$l_j = \begin{cases} 1 & \text{if } (L < L_j < L + \Delta L) \text{ and } (D_j < D) \\ 0 & \text{otherwise} \end{cases}$$

and the sum over j runs through all the galaxies in the catalog. The quantities L_j and D_j are the luminosity and distance of each galaxy. Similarly we can compute the luminosity function in terms of blue absolute magnitudes as a function of distance $N(M_{\mathrm{B}}, D)$. The dashed and dot-dashed lines in Fig. 3.4 show several realizations of $N(M_{\mathrm{B}}, D)$ for different distances D plotted as a function of M_{B}.

To estimate the degree of incompleteness in the CBCG-catalog, we use an analytical Schechter galaxy luminosity function (71)

$$\phi(L)dL = \phi^*\left(\frac{L}{L^*}\right)^\alpha \exp\left(\frac{-L}{L^*}\right)d\left(\frac{L}{L^*}\right)$$ (3.2)

where $\phi(L)dL$ is the number density (number of galaxies per unit volume) within the luminosity interval L and $L + dL$, L^* is the luminosity at which the number of galaxies begins to fall off exponentially, α is a parameter which determines the slope at the faint end of

the luminosity function, and ϕ^* is a normalization constant. In terms of (blue) absolute magnitudes, M_{B}, the Schechter function becomes

$$\tilde{\phi}(M_{\mathrm{B}})dM_{\mathrm{B}} = 0.92\,\phi^* \exp\left[-10^{-0.4(M_{\mathrm{B}}-M_{\mathrm{B}}^*)}\right]\left[10^{-0.4(M_{\mathrm{B}}-M_{\mathrm{B}}^*)}\right]^{\alpha+1}\,dM_{\mathrm{B}}\ . \tag{3.3}$$

To estimate the total luminosity function, we use results from the Sloan Digital Sky Survey (SDSS) as reported by (72). Although the SDSS sky coverage is inadequate in RA and DEC, it provides excellent coverage throughout our desired distance and beyond. We therefore use the green luminosity function Schechter fit given in Table 2. of (72) and convert it into blue band using the expression given in Table 2. of (73). Adopting a Hubble constant value of $73\,\mathrm{km\,s^{-1}\,Mpc^{-1}}$ (69) and correcting for reddening,[4] the Schechter parameters are $(M_{\mathrm{B}}^*, \tilde{\phi}^*, \alpha) = (-20.3, 0.0081, -0.9)$. The solid line in Fig. 3.4 shows the Schechter function $\tilde{\phi}(M_{\mathrm{B}})$ derived from these values. Since this function is obtained from deep surveys, it does not account for the local over-density of blue light coming primarily from the Virgo cluster. For distances up about to 30 Mpc, the CBCG-catalog's luminosity function $N(M_{\mathrm{B}}, D)$ exceeds $\tilde{\phi}(M_{\mathrm{B}})$.

We can now derive a completeness correction that arises at the faint end beyond about 30 Mpc, where the Schechter function exceeds the catalog $N(M_{\mathrm{B}}, D)$. We integrate the CBCG-galaxy-catalog luminosity function $N(L, D)$ over L and subtract it from the Schechter fit as a function of distance. Hence, the total corrected cumulative luminosity L_{total} within a volume of radius D is given by

$$L_{\mathrm{total}}(D) = L_{\mathrm{CBCG}}(D) + L_{\mathrm{corr}}(D) \tag{3.4}$$

where

$$L_{\mathrm{CBCG}}(D) = \int_0^D dD' \sum_{\mathrm{j}} L_{\mathrm{j}}\delta(D' - D_{\mathrm{j}}) \tag{3.5}$$

$$L_{\mathrm{corr}}(D) = \frac{4\pi}{3}D^3 \int_{L_{\mathrm{min}}}^{L_{\mathrm{max}}} L\,dL\ \Theta\left[\phi(L) - N(L, D)\right]\ \left[\phi(L) - N(L, D)\right]\ . \tag{3.6}$$

Here, the index j runs through all galaxies in the catalog, δ is the Dirac delta function, Θ is the step function and $\phi(L)$ is the adopted Schechter function (distance independent) assumed to represent the complete luminosity distribution. We note that $L_{\mathrm{max}} = 52.481\,L_{10}$ ($M_{\mathrm{B}} = -23.83$) is the maximum luminosity in the CBCG-catalog and we choose $L_{\mathrm{min}} = 10^{-3}L_{10}$ ($M_{\mathrm{B}} = -12.98$) because luminosities below this value do not contribute significantly to the net luminosity. The quantity L_{CBCG} in Eqs. (3.4) and (3.5) is the uncorrected cumulative luminosity from the CBCG-catalog; the quantity L_{corr} is the completeness correction. Note that the completeness correction term is always zero or positive regardless of the choice of Schechter function.

In Fig. 3.5, we show the cumulative blue luminosity as a function of distance as obtained directly from the CBCG-catalog (solid line) as well as with the completeness correction applied (dashed line). It is evident that the correction becomes significant at distances in excess of about 40Mpc.

---

[4]We correct the value of M_{B}^* to be consistent with the reddening correction described in §3.3.1
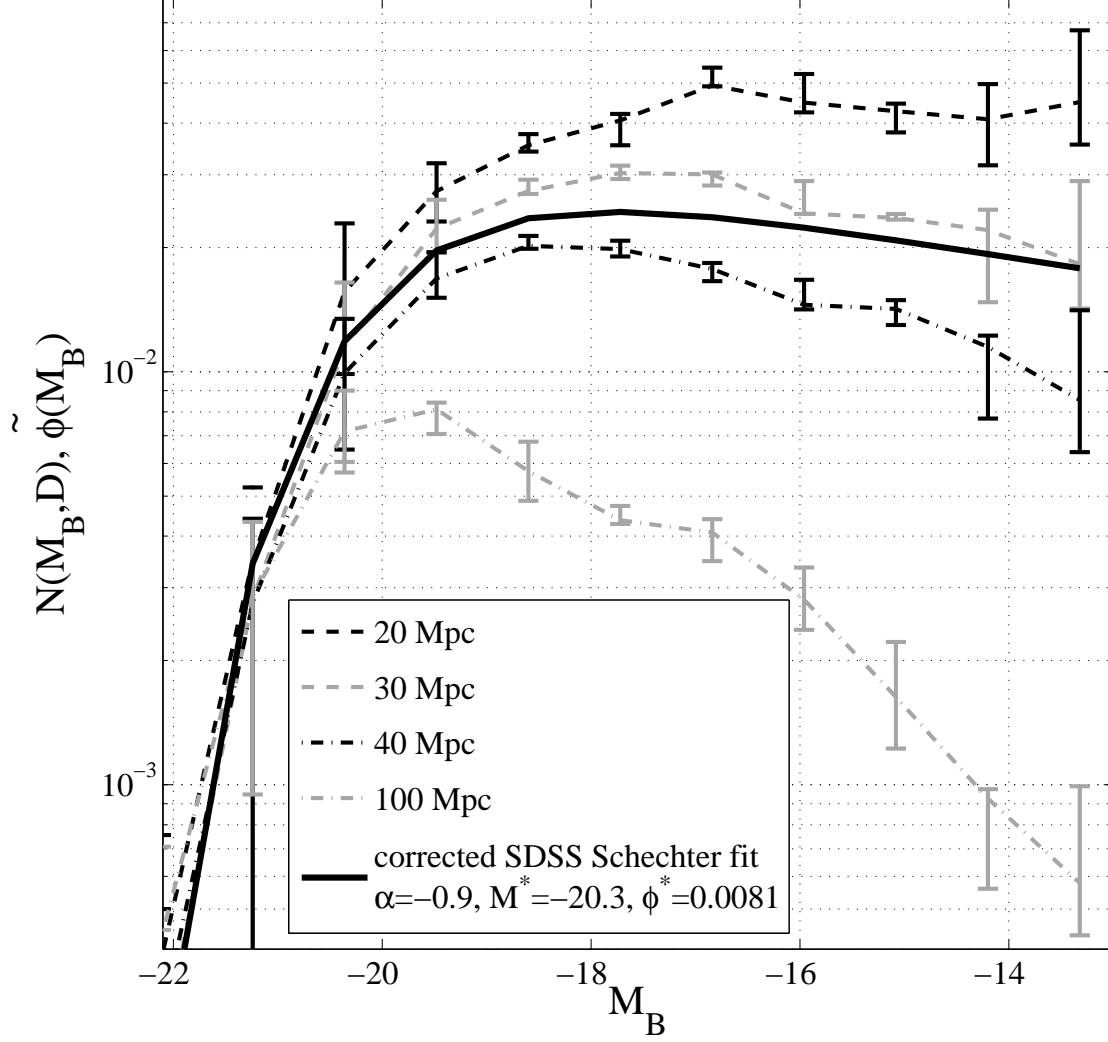
Figure 3.4: The luminosity function of CBCG catalog at various distances (dashed and dot-dashed lines) and a Schechter function fit (solid line) given in Eq. (3.3) based on (72). We compensate for the incompleteness of the CBCG-catalog by applying an upward correction to the luminosity bins that are below the Schechter function fit (solid line), according to Eqs. (3.4) and (3.6). Error bars are found by sliding the magnitudes of each galaxy according to the mean errors and recomputing the luminosity function.

3.3.1 Comparison with Other Results

To compare our method of correcting for completeness with other methods, we consider the direct computation of a reddening corrected luminosity density based on (72) which could be used at large distances. We adopt a blue luminosity density of $(1.98\pm0.16)\times10^{-2}L_{10}/\mathrm{Mpc}^3$ calculated as follows:

- The blue luminosity density, in terms of blue absolute magnitudes per cubic Mpc, is -14.98 locally (redshift $z = 0$) and -15.17 for $z = 0.1$ [Table 10 (72)]. This is for a standard cosmology with $\Omega_{\mathrm{M}} = 0.3$ and $\Omega_{\Lambda} = 0.7$. We use $z = 0.1$ so that the results will be valid for advanced detectors.

- We convert the $z = 0.1$ blue magnitude density (-15.17) to luminosity units $1.33 \times 10^{-2}L_{10}/\mathrm{Mpc}^3$ and assign systematic errors ($\simeq 10\%$) associated with the photometry to obtain a luminosity density of $(1.33 \pm 0.13) \times 10^{-2}L_{10}/\mathrm{Mpc}^3$.

- We also correct for processing of blue light and re-emission in the infrared (IR) following (58) and (74). We use the analysis of (75), upward correct by 30% their far IR ($40\mu m - 100\mu m$) luminosity density to account for emission down to $12\mu m$ (74), and convert to L_{10} to obtain an IR luminosity density of $L_{\mathrm{IR}} = (0.65 \pm 0.1) \times 10^{-2}L_{10}/\mathrm{Mpc}^3$.

- Adding both luminosity densities above and accounting for the errors, we obtain a blue light luminosity density corrected for extinction equal to $(1.98\pm0.16)\times10^{-2}L_{10}/\mathrm{Mpc}^3$

We use this blue luminosity density and its uncertainty and plot the implied cumulative blue luminosity as a function of distance (cubic dependence) in Fig. 3.5 (gray-shaded region). This uniform density distribution agrees well with the completeness corrected luminosity given above.

We can compare our results for the cumulative blue luminosity as a function of distance to similar results obtained by (76), especially their Figure 1. The results for the uncorrected catalog agree qualitatively. However, the catalog described here is more up-to-date compared to the one compiled by (76) by virtue of the updates to LEDA and by the inclusion of the current Tully catalog. The incompleteness correction derived here is also more physically and empirically motivated than the one constructed in that earlier paper. We note that the cumulative luminosity shown as the dashed line in their Figure 1 is too low by a factor of $4\pi/3$ due to a numerical error. Additionally, their luminosity density is $\sim 25\%$ lower than ours resulting from our use of the more recent results presented by (72).

3.4 Compact Binary Coalescence Rate Estimates

For neutron star binaries, the observed binary pulsar sample can be used to predict the coalescence rate $\mathcal{R}_{\mathrm{MW}}$ in the Milky Way (77; 78). The coalescence rate within a sphere of radius D is then simply given by

$$R = \mathcal{R}_{\mathrm{MW}} \left(\frac{L_{\mathrm{total}}(D)}{L_{\mathrm{MW}}} \right) \tag{3.7}$$

where $L_{\mathrm{total}}(D)$ is the total blue luminosity within a distance D and L_{MW} is the blue luminosity of the Milky way, $1.7L_{10}$ (74). If the rate R of a binary neutron star coalescence
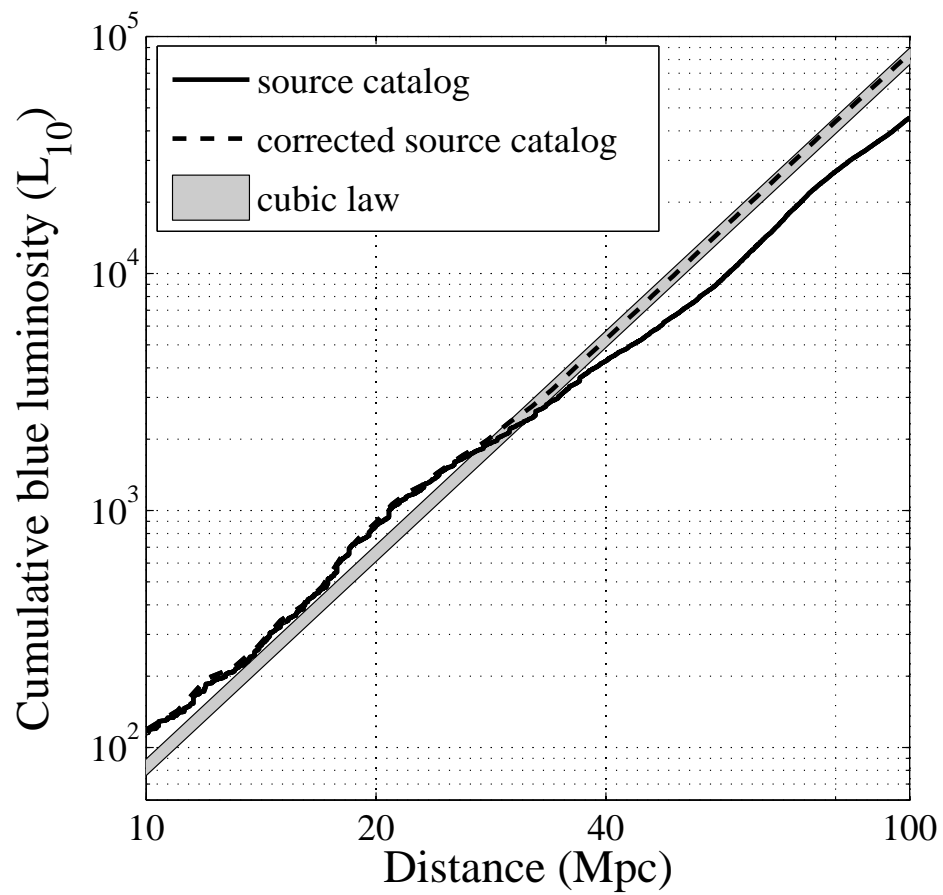
Figure 3.5: Cumulative luminosity as a function of distance from CBCG-catalog uncorrected for incompleteness (solid line), corrected for incompleteness (dashed line) and the cubic extrapolation from the assumed constant blue luminosity density corrected for extinction (gray-shaded region).

could be measured directly, it would provide an independent estimate of the rate of coalescence per unit of blue luminosity. Together these two measurements would deepen our understanding of stellar and binary evolution. Furthermore, the current understanding of binary evolution and compact object formation leads us to anticipate the formation of black hole binaries that will merge within a Hubble time (79; 80). Experiments like LIGO will provide a direct measure of the compact binary coalescence rate and will impose constraints on the theoretical models of stellar evolution and compact binary formation.

3.4.1 Rate Estimates and Systematic Errors in Gravitational-Wave Searches

In its simplest form, the rate estimate derived from a gravitational-wave experiment like the one described in chapter 2 will take the form

$$\mathcal{R} = \frac{\text{constant}}{T\,\mathcal{C}_L} \qquad (3.8)$$

where the constant depends on the precise outcome of the search and the statistical method used in arriving at the rate estimate, $\mathcal{C}_L$ is the cumulative blue luminosity *observable* within the search's sensitivity volume measured in L_{10}, and T is the time analyzed in years. In general the sensitivity volume is a complicated function which depends on the instrument and the gravitational-waveforms searched for. Here, we focus on the influence of the host galaxy properties and the distribution of blue light with distance.

The gravitational-wave signal from a compact binary inspiral depends on a large number of parameters. It is convenient to split these parameters into two types for our discussion. Of particular interest here are the parameters which determine the location and orientation of the binary. We denote these collectively as $\vec{\lambda} := \{D, \alpha, \delta, \iota, \psi, t\}$: the distance D to the binary, its Right Ascension α and declination δ, inclination angle ι relative to the line of sight, polarization angle ψ of the waves, and the time t when the binary is observed, respectively. Other parameters, including the masses and the spins, which are used to build template banks for the search, are denoted $\vec{\mu}$. Recognizing that the spatial luminosity distribution can be written as

$$L(\alpha, \delta, D) = \sum_j L_j\, \delta(\alpha_j - \alpha)\, \delta(\delta_j - \delta)\, \delta(D_j - D)\,, \qquad (3.9)$$

we write the cumulative luminosity as

$$\mathcal{C}_L = \int L(\alpha, \delta, D)\, p(\text{detection}|\vec{\mu}, \vec{\lambda})\, p(\vec{\mu})\, p(\iota)\, p(\psi)\, p(t)\, d\vec{\mu}\, d\vec{\lambda} \qquad (3.10)$$

Assuming that binary coalescences are uniformly distributed in time, and their orientation is random, we take the corresponding prior probabilities: $p(\iota) = \sin(\iota)/2$, $p(t) = 1/\text{day}$, and $p(\psi) = 1/2\pi$.

Systematic errors associated with the derived rate estimates are naturally associated with the errors in cumulative luminosity $\mathcal{C}_L$. The two most relevant errors in the galaxy catalog are in apparent magnitude m_B and distance D. Sky positions are known so precisely that small errors in RA and DEC do not change the detection probability of a particular binary in any significant way; for this reason, such errors are not included in the LIGO analyses (16). The errors induced on the spatial luminosity function in Eq. (3.9) take the form (33)

$$[L + \Delta L](\alpha, \delta, D) = \sum_j L_j \, 10^{-0.4\Delta m_{Bj}} \left(1 + \frac{\Delta D_j}{D_j}\right)^2 \delta(\alpha_j - \alpha)\, \delta(\delta_j - \delta)\, \delta(D_j + \Delta D_j - D)\,.$$

(3.11)

3.4.2 A Simplified Model for Estimating Expected Event Rates

The sensitivity of a search for gravitational-waves from compact binary coalescence is determined primarily by the amplitude of the waves at the detector. For a non-spinning binary (i.e., the spins of each compact object are much smaller than their general-relativistic maximum value of m_i^2) with given $\vec{\mu}$, the amplitude is inversely proportional to the *effective distance* D_{eff} defined in chapter 2 as (47)

$$D_{\text{eff}} = \frac{D}{\sqrt{F_+^2(1 + \cos^2 \iota)^2/4 + F_\times^2 \cos^2 \iota}}$$

(3.12)

where D is the physical distance to the binary, F_+ and $F_\times$ are the response amplitudes of each polarization at the detector which depend upon the location of the binary system (81):

$$F_+ = -\frac{1}{2}(1 + \cos^2 \theta) \cos 2\phi \cos 2\psi - \cos \theta \cos 2\phi \sin 2\psi$$

(3.13)

$$F_\times = \frac{1}{2}(1 + \cos^2 \theta) \cos 2\phi \sin 2\psi - \cos \theta \sin 2\phi \cos 2\psi\,.$$

(3.14)

Here θ and ϕ are the spherical co-ordinates of the source defined with respect to the detector and, as before, ι and ψ are the inclination and polarization angles. Since θ and ϕ are detector dependent, the effective distance is different for geographically separated detectors that are not perfectly aligned and, for a fixed source location, changes as the Earth rotates through a sidereal day. Additionally, the effective distance is always at least as large as the physical distance.

For simplicity in understanding the sensitivity of gravitational-wave searches, consider the case in which $\vec{\mu}$ is fixed, i.e. $p(\vec{\mu}) = \delta(\vec{\mu} - \hat{\mu})$. For example, these might be the parameters appropriate to a neutron star binary. The sensitivity of a detector is given by its horizon distance, which is defined as the maximum effective distance that a neutron star binary system can be detected at signal-to-noise ratio of 8. Consider a search which can perfectly detect these binaries if they have an effective distance $D_{\text{eff}} < D_{\text{horizon}}$ at a particular detector. Then

$$p(\text{detection}|\hat{\mu}, \vec{\lambda}) = \Theta(D_{\text{eff}}(\vec{\lambda}) < D_{\text{horizon}})$$

(3.15)

and we can write

$$\mathcal{C}_L(D_{\text{horizon}}) = \int L(\alpha, \delta, D)\, \Theta(D_{\text{eff}}(\vec{\lambda}) < D_{\text{horizon}})\, p(\iota)\, p(\psi)\, p(t)\, d\vec{\lambda}\,.$$

(3.16)

Thus, the cumulative blue luminosity accessible to such a detector is the blue luminosity within an effective distance sphere of radius D_{horizon}, averaged over the time of day and possible orientations of the binary. The lower curve in Fig. 3.6 shows $\mathcal{C}_L(D_{\text{horizon}})$. Figure 3.6 also illustrates the significant difference between the cumulative luminosity $\mathcal{C}_L(D_{\text{eff}})$ and

total luminosity $L_{\text{total}}(D)$ at a given distance. If galaxies are distributed uniformly in space the ratio between these is $\simeq 11.2$; this is the factor by which the detection rate would be reduced and arises purely from the LIGO detector response, averaged over all possible source orientations with respect to the detector.

When estimating the rate based on gravitational-wave observations, one can marginalize over uncertainties (33) in the galaxies' distances and apparent magnitudes. Specifically, by making use of the modified spatial distribution function Eq. (3.11) and the distributions for ΔD_j and Δm_{Bj} reported here, we can obtain a probability distribution for the cumulative luminosity $p(\mathcal{C}_L | \Delta m_{Bj}, \Delta D_j)$ from Eq. (3.10). For each value of the cumulative luminosity, a probability distribution $p(R|\mathcal{C}_L)$ for the event rate can be calculated. Finally, the rate is marginalized over errors in the galaxy catalog by computing

$$p(R) = \int d\mathcal{C}_L \; p(\mathcal{C}_L | \Delta m_{Bj}, \Delta D_j) \; p(R|\mathcal{C}_L) \,. \tag{3.17}$$

This distribution is then used to obtain a rate interval or upper limit on the occurrence of binary coalescences in the universe.

While this approach provides a reasonable estimate of the observable blue light luminosity in a single detector, it does not provide the whole story. For example, the $16°$ difference in latitude between the LIGO Observatories in Hanford, Washington and Livingston, Louisiana, implies the $\mathcal{C}_L(D_{\text{horizon}})$ depends on the site used. Figure 3.7 shows two-dimensional contours of this function.

Based on the galaxy catalog presented in this article, the cumulative blue luminosity $\mathcal{C}_L$, measured in L_{10}, accessible to a search with a given horizon distance sensitivity can be derived from Fig. 3.6 and is tabulated in Table 3.2. We can combine the calculated cumulative blue luminosity with estimates of $\mathcal{R}$, the rate of binary mergers per L_{10}, to estimate the number of compact binary merger events N detectable in a given LIGO search with an observation time T:

$$N = 10^{-3} \left(\frac{\mathcal{R}}{L_{10}^{-1} \; \text{Myr}^{-1}} \right) \left(\frac{\mathcal{C}_L}{10^3 L_{10}} \right) \left(\frac{T}{\text{yr}} \right) \tag{3.18}$$

If the horizon distance of a search is larger than 50 Mpc, we can use the following approximation, from a cubic law:

$$N \approx 7.4 \times 10^{-3} \left(\frac{\mathcal{R}}{L_{10}^{-1} \; \text{Myr}^{-1}} \right) \left(\frac{D_{\text{horizon}}}{100 \; \text{Mpc}} \right)^3 \left(\frac{T}{\text{yr}} \right) \tag{3.19}$$

Estimated rates of binary neutron star (BNS) mergers in our Galaxy are based on the observed sample of binary pulsars. The rates depend on the Galactic distribution of compact objects. In (35), the most recent reference estimating rates, the most likely Galactic rate for their reference model 6 is $83 \, \text{Myr}^{-1}$, with a 95% confidence interval $17 - 292 \, \text{Myr}^{-1}$. The most likely rates for all the models used in (35) are in the range $4 - 220 \, \text{Myr}^{-1}$ for the Milky Way.[5]

For the 4km LIGO detectors currently operating, $D_{\text{horizon}} \approx 30$ Mpc for BNS. Thus, the predicted number of BNS events is in the range $N_6 \approx 2 - 30 \times 10^{-3} \, \text{yr}^{-1}$ with the most likely number being $N_6 \approx 1/(100 \, \text{yr})$ [we use the subscript $_6$ to indicate these rates use reference

---

[5]The rates quoted here are in units of rate per Milky Way per Myr; to get the rate per L_{10}, we divide by 1.7 which is the estimated blue luminosity of the Milky way in L_{10} units, assuming the blue absolute magnitude of the Milky Way to be -20.11 (74).
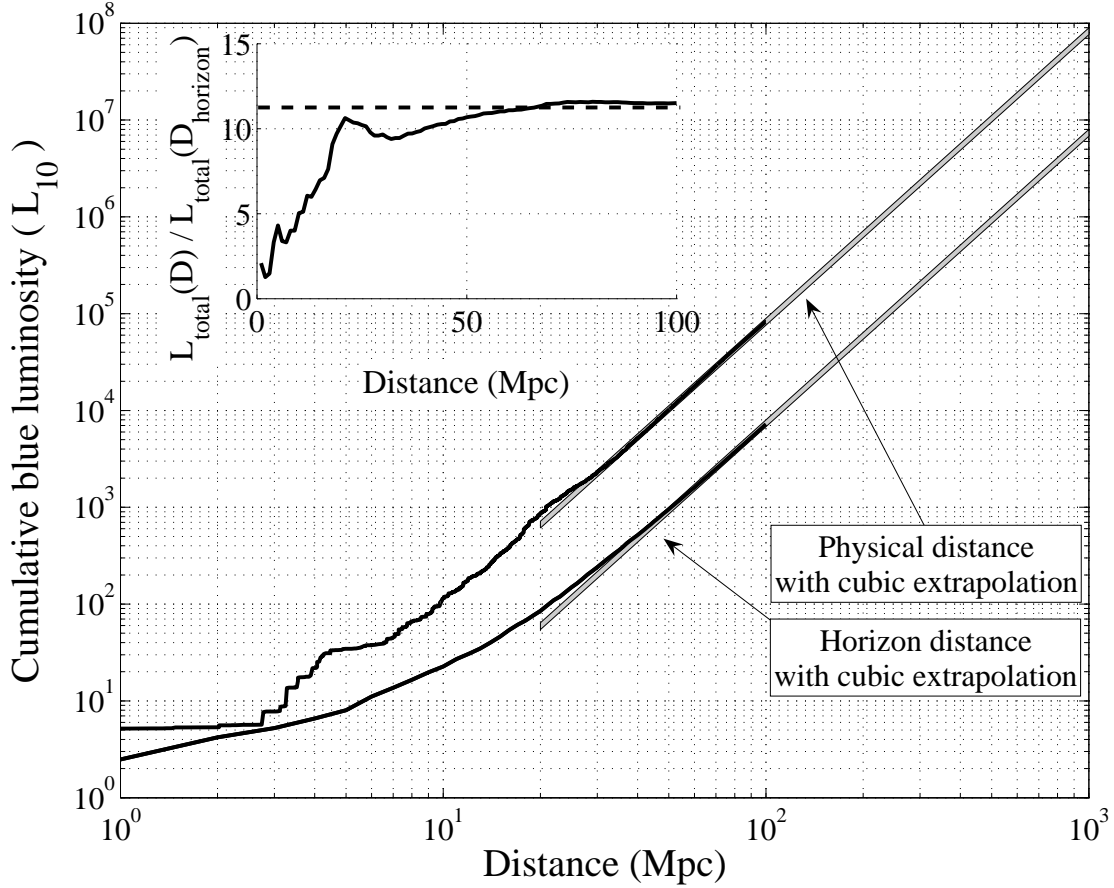
Figure 3.6: Cumulative luminosity as a function of physical distance (top line) and horizon distance (bottom line). The horizon distance D_{horizon} is defined as the physical distance to an optimally oriented and located binary system that would be detected with a signal-to-noise ratio of 8. (Instrumental sensitivity range is sometimes quoted in terms of the radius of a sphere with the same volume as the non-uniform region probed by the instrument, this sensitivity range D_s is related to the horizon distance by $D_s \simeq D_{\text{horizon}}/\sqrt{5}$. The gray shaded lines are cubic extrapolations (§3.3) derived for both cases. Given a LIGO horizon distance one can immediately get the cumulative blue luminosity from the bottom curve. To obtain an approximate rate upper limit one could calculate $\mathcal{R}_{90\%}\,[\,\text{yr}^{-1}L_{10}^{-1}] = 2.3/(\mathcal{C}_L \times T)$ where $\mathcal{C}_L$ is taken from this plot at a given range in horizon distance. *Inset:* Ratio of the cumulative luminosity for the physical and horizon distance from the completeness corrected CBCG-catalog illustrates the non-uniform distribution at smaller ranges (< 20 Mpc) and asymptotes to the expected uniform distribution ratio (dashed line) for larger distances.
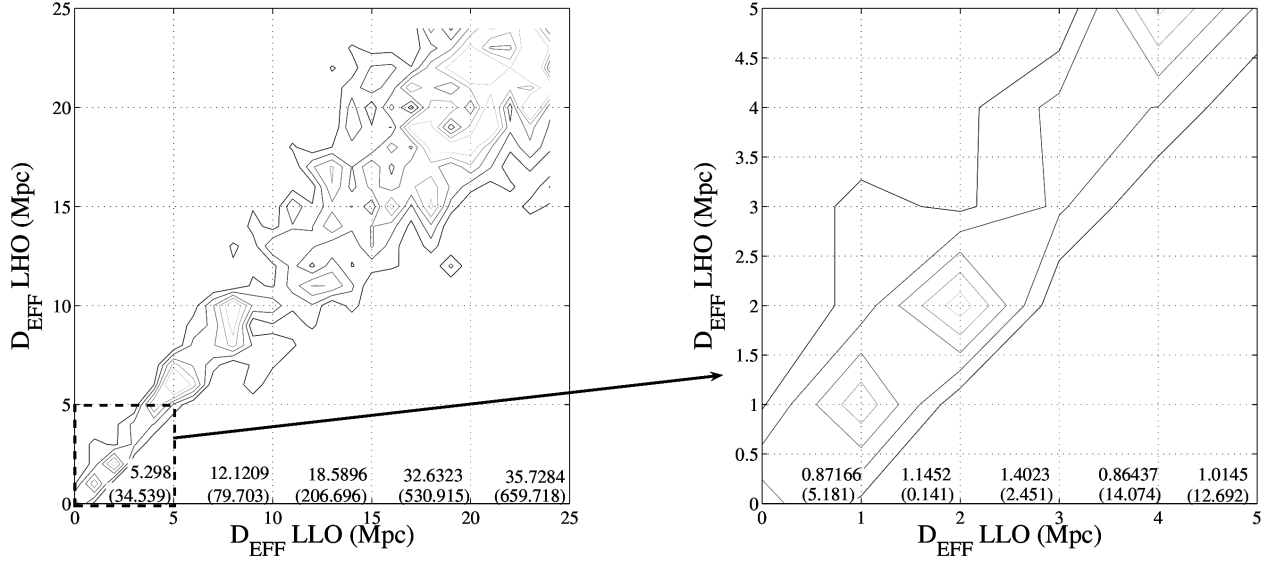
Figure 3.7: Luminosity contours per effective distance bin in the two LIGO sites. The effective distance to a source in one galaxy is different between the two detectors, changes as a function of the sidereal day and also on the orientation of the particular source. Since the effective distance is always larger than the real distance the luminosity available within a given effective distance bin is considerably smaller than the luminosity within the physical distance bin. The upper horizontal numbers refer to the luminosity per bin in effective distance. The parenthetical lower numbers refer to the luminosity per physical distance bin. It is also possible to have a systematically different luminosity between detectors as is indicated in the right panel zoom of the first 5 Mpc. The available luminosity within 5 Mpc (mostly from Andromeda) is slightly better located for LLO and therefore stretches the contours to higher effective distances for LHO. LIGO rate upper limits for searches with limited range thus depend on the non-uniformity of the Local Group.

Table 3.2: Table showing the cumulative blue luminosity $\mathcal{C}_L(D_{\mathrm{horizon}})$ accessible to a search with horizon distance D_{horizon} given in the first column. For $D_{\mathrm{horizon}} > 100$ Mpc, the cumulative blue luminosity accessible to a search is given approximately by $C_L(D_{\mathrm{horizon}}) \approx 7.4 \times 10^3 \; (D_{\mathrm{horizon}}/100\mathrm{Mpc})^3$.

D_{horizon} (Mpc)	$\mathcal{C}_L(D_{\mathrm{horizon}})$ (L_{10})
10	23
20	85
30	240
50	953
100	7200
200	59200
300	200000
500	926000

model 6 from (35)]. A search that reaches twice the distance (such as enhanced LIGO), yields a most likely rate $N_6 \approx 1/(10 \text{ yr})$. And a search that would be 15 times more sensitive to coalescences of binary systems than the current LIGO detectors (such as Advanced LIGO) would yield a most likely rate of $N_6 \approx 40.0 \text{ yr}^{-1}$.

3.5 Conclusion

Whether one wishes to compute expected detection rates for LIGO searches, or to interpret LIGO searches as rate upper limits (or eventually detection rates), we require at the simplest level accurate accounting of the total observable blue luminosity $\mathcal{C}_L$. As mentioned in the previous sections, a galaxy catalog complete with sky positions and distances is important for first generation LIGO detectors because the blue luminosity is not uniformly distributed in the sky within the search range. An upper limit which takes in to account the most up-to-date information on galaxy distribution can be obtained by accurately modeling the local overdense region. For searches with ranges well beyond current sensitivity the universe is uniform and rate estimates depend primarily on accurate blue luminosity densities corrected for reddening. We have introduced a method to bridge the gap between the well known nearby galaxy distribution and the expected long range distribution through a completeness correction based on SDSS luminosity functions (72).

This paper provides the most up to date accounting of nearby galaxies within 100Mpc as well as errors in the apparent magnitude (corrected for reddening) and distance and demonstrates how the errors propagate into rate calculations. Astrophysical errors are a significant contribution to the eventual systematic error associated with coalescence rate upper limits (33) and must be included. This paper provides a survey of the asymptotic and local uncertainty. Motivated by the use of effective distance to account for the antenna pattern of the LIGO detectors, we demonstrate the need to compute the average blue light luminosity within a given effective distance sphere. For ranges within 50Mpc there is a nontrivial relationship between cumulative blue luminosity within an effective distance sphere and within a physical distance sphere. Beyond 50Mpc the relationship is well behaved leading to the simple scaling for the number of detected events N given in Eq.(3.19). We would like to point that the catalog provided can also be used on other astronomical analysis of populations that scale with galaxy blue luminosity, such as the local Type II supernova rate or the rate of nearby SGR bursts that show up as short GRBs.

We provide sufficient description of our methods for others to apply new rate models to future LIGO data. Although this catalog will serve as a reference for current and future LIGO data analysis, we look forward to future work that may transcend the simple blue light rate normalization that we have discussed. One way to go beyond blue light rate normalization, (necessary to ascertain the degree to which old stars contribute to present day mergers) is with multiband photometry of nearby galaxies which can reconstruct their mass, morphology and metallicity dependent star formation history. With this information in hand LIGO detections could be applied more stringently to assess the relative contribution that progenitors of different ages provide to the present day merger rate.

These first three chapters described searches for compact binary coalescence and interpretation of the results. The remaining three chapters will turn to discussing improvements to compact binary searches. Chapter 4 discusses improving the template waveform models.

4. Method to Estimate ISCO and Ring-Down Frequencies in Binary Systems and Consequences for Gravitational-Wave Data Analysis[1]

4.1 Introduction

As discussed in chapter 2, the SNR for a binary inspiral search depends on having a template waveform that matches the true signal correctly (83). This chapter examines ways in which searches for compact binary coalescence may be improved by recent advances in waveform modeling with numerical relativity.

Because matched filter templates are weighted by the noise power spectral density of the detector with non-trivial frequency dependence it is important *when* in the binary evolution the template matches well. Numerical simulations are improving our knowledge of the full waveforms emitted during the inspiral, merger and ring-down phases of binary black hole coalescence (86; 87; 88), yet they still do not cover an adequate parameter space for constructing filter banks (89; 88). When the full parameter space is simulated it will be useful to have fully parameterized models of these waveforms and even now many have considered hybrid waveforms that patch together PN and numerical simulations (90; 91; 86; 87; 88) as data analysis templates. Others have introduced a phenomenological fourth order correction to make effective one-body (EOB) waveforms match numerical relativity results near the merger (90; 86) known as *pseudo* 4PN (p4PN).

Before the full parameter space is simulated it is still possible to handle the three binary coalescence epochs - inspiral, merger and ring-down - separately. We will show that a recent calculation (92) which has power to predict the final spin of a binary merger, can provide both insight into when the inspiral phase ends and what the quasi-normal ring-down frequency of the merger product should be for a large, yet un-simulated, parameter space. We will discuss the following consequences of this calculation:

- The calculation of the final spin given in (92) contains an implicit reference to the innermost stable circular orbit (ISCO) of a test particle orbiting the Kerr black hole that results from the merger. We will also discuss the impact of using the new ISCO frequency as a cut off for current gravitational-wave searches that are targeting coalescing compact objects.

- Knowing the final spin gives an estimate for the quasi-normal mode ring-down frequencies. These frequencies could be used in a separate matched filter search (24).

- We can also use the final spin to calculate the light ring (smallest, unstable circular orbit for a photon orbiting a Kerr black hole) and quasinormal mode ringdown frequencies of the final black hole; we will see that the l=2, m=2, n=0 QNM is quite close to the light ring frequency. We will define a merger epoch as the evolution from ISCO to light ring and dicuss how to obtain its time frequency content for yet unsimulated systems.

We define the merger epoch as everything that occurs between the ISCO and ringdown frequencies. We show that the duration of the radiation seems to be well described by the infall duration of a test particle orbitting the merged black hole just below the ISCO. Knowing the duration and bandwith gives a time-frequency volume, which is useful in data analysis for unmodeled signals.

4.2 Formalism

The inspiral phase of two compact objects is generally considered to end when the binary has evolved to an innermost stable circular orbit (ISCO), should it exist. The ISCO can be defined by waveform models and numerical relativity (95; 96; 86). Unfortunately there is a difference in the numbers obtained from different methods. Some LIGO searches for non-spinning systems have taken the conservative approach to use the ISCO defined for a test particle orbiting a Schwarzschild black hole.

Intuitively the space-time of an inspiralling comparable mass binary system will not be well described by a Schwarzschild space-time, and thus the Schwarzschild ISCO will not capture the dynamics correctly. If the merger product is a black hole, it will be a Kerr-like black hole with a final spin that is a function of the masses and spins of the components. Recently (92) has proposed a simple set of assumptions that predict the final spin of the black hole merger product to well within 10% of numerical simulations based on first principle arguments. Implicitly in the derivation of (92) is the ISCO radius of a test particle orbiting a Kerr black hole having a final spin equal to the spin of the merger product. The fact that the ISCO radius used gives the correct answer for the final space-time suggests that it plays an important role in the pre-merger dynamics. We hypothesize that the test particle ISCO of the merged Kerr black hole may describe a way to define the end of the inspiral phase for binaries that produce black holes.

The ISCO solution for a test particle orbiting a Kerr black hole is (98),

$$
\begin{aligned}
Z_1 &\equiv 1 + \left(1 - \frac{a_f^2}{M^2}\right)^{1/3}\left[(1 + \frac{a_f}{M})^{1/3} + (1 - \frac{a_f}{M})^{1/3}\right] \\
Z_2 &\equiv \left(3\frac{a_f^2}{M^2} + Z_1^2\right)^{1/2} \\
r_{\mathrm{ISCO}} &= M\{3 + Z_2 \mp [(3 - Z_1)(3 + Z_1 + 2Z_2)]^{1/2}\} \ ,
\end{aligned}
\tag{4.1}
$$

where M is the total mass of the black hole and a_f is the angular momentum. The final spin is required in order to compute this ISCO. In (92), assuming the amount of mass and angular momentum radiated beyond the ISCO is small, the following implicit formula for the final angular momentum of a black hole a_f with component spins aligned with the orbit is calculated,

$$
\frac{a_f}{M} = \frac{L_{orb}}{M^2}\left(q, \frac{r}{M} = \frac{r_{\mathrm{ISCO}}}{M}, \frac{a_f}{M}\right) + \frac{q^2\chi_1 + \chi_2}{(1 + q)^2} \ ,
\tag{4.2}
$$

where $\chi_i = a_i/m_i$, $q = m_1/m_2 \in [0, 1]$ and $M = m_1 + m_2$ is the total mass. The implicitly found a_f agrees well with numerical simulations (92) and the analysis can be modified to include arbitrary spin angles. L_{orb} is the orbital angular momentum contribution calculated from the orbital angular momentum of a particle at the ISCO of a Kerr black hole with spin

parameter a_f, which has the following expression (98),

$$\frac{L_{orb}}{M^2}\left(q, \frac{r}{M}, \frac{a_f}{M}\right) = \frac{q}{(1+q)^2}\frac{\pm(r^2 \mp 2a_f M^{1/2}r^{1/2} + a_f^2)}{M^{1/2}r^{3/4}(r^{3/2} - 3Mr^{1/2} \pm 2a_f M^{1/2})^{1/2}} \quad , \tag{4.3}$$

where the upper/lower signs correspond to prograde/retrograde orbits. In order to agree with numerical simulations this function has to be evaluated at $r = r_{ISCO}$ given by equation (4.1). Alternative radii in the above prescription – like the photon-ring radius or Schwarzschild radius – give a prediction that is off the numerically obtained value. This fact, combined with the same analysis extended to elliptic binaries, again depending sensitively on the ISCO location (101), suggests the ISCO radius determined by this approach is relevant(102).

In order to get the gravitational-wave frequency at ISCO we use the coordinate angular velocity of a circular orbit (98),

$$\Omega = \pm\frac{M^{1/2}}{r^{3/2} \pm a_f M^{1/2}} \quad , \tag{4.4}$$

with a_f given by the implicit equation (4.2). The gravitational-wave frequency at a given radius is then $f = \Omega/\pi$, and so we define $f_{\text{ISCO[BKL]}}$ as the frequency obtained by solving the system of equations (4.1-4.4) at the Kerr ISCO radius.

The solution space for $f_{\text{ISCO[BKL]}}$ can be written as a function of the final unknown spin a_f. For convenience, we prefer to extend it as a surface parametrized by (a_f, q, χ), as it is shown in figure 4.1. This way the mass ratio dependence of the lines corresponding to different individual spins can be seen explicitly. For the equal mass case without spin the approximate expression for the Kerr test particle ISCO frequency is,

$$f_{\text{ISCO[BKL]}}(M, q) \approx \left(0.8q^3 - 2.6q^2 + 2.8q + 1\right) \times \frac{1}{\pi 6^{3/2}M} \quad , \tag{4.5}$$

which can be compared to the Schwarzschild test particle ISCO $f_{\text{ISCO[SCH]}} = \pi^{-1}6^{-3/2}M^{-1}$.

Once the final spin is known it is possible to compute the last stable photon orbit ("light ring") and the quasi-normal mode ring-down frequencies (94). The light ring for a Kerr black hole is, (98)

$$r_{\text{light}} = 2M\{1 + \cos\left[2/3 \cos^{-1}\left(\mp a_f/M\right)\right]\} \tag{4.6}$$

$$\Omega_{\text{light}} = \pm\frac{M^{1/2}}{r_{\text{light}}^{3/2} \pm a_f M^{1/2}} \quad , \tag{4.7}$$

An approximate fit to the quasinormal mode ringdown frequencies as a function of the final spin is given in (103; 24; 104). For the l=2, m=2, n=0 mode we have,

$$\Omega_{\text{QNM}} \approx \frac{0.5}{M}\left(1 - 0.63(1 - a_f)^{0.3}\right) \quad , \tag{4.8}$$

Others ring-down modes could could be computed as necessary.

Figure 4.2 compares the BKL ISCO for non-spinning binaries with the ISCOs computed from the minimum energy conditions at 3PN order (97) as well as 2PN and p4PN EOB ISCOs (93; 94). BKL and EOB agree exactly with the Schwarzschild ISCO at the extreme
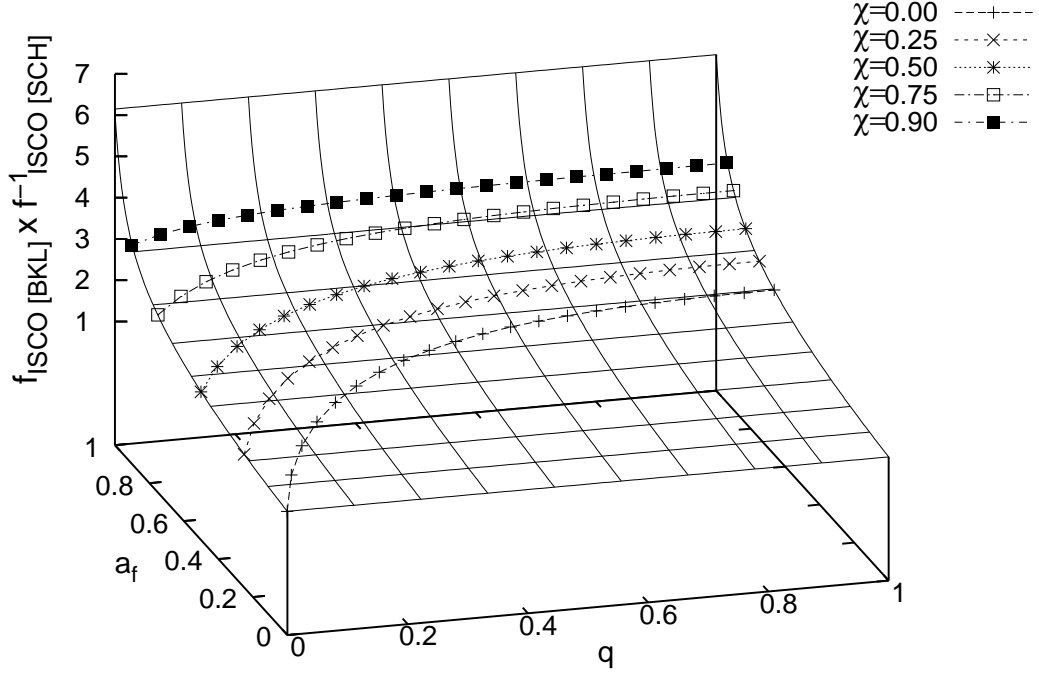
Figure 4.1: The surface of solutions of the frequencies at the ISCO as a function of the mass ratio q and the final spin a_f for components with spins that are aligned with the orbital angular momentum. Also shown, are curves corresponding to the solution of the equal spin case $\chi_1 = \chi_2 = \chi$.

mass ratio limit, but the PN calculations are known to be inconsistent (97) in that regime. Predicting the final spin gives the $l = m = 2$ ring-down mode frequency by (4.8) and the light ring frequency. Both are shown in figure 4.2. The ISCO and light ring set a natural "merger" epoch which can be searched for by burst search techniques (14) *in between* the inspiral and ring-down matched filter searches. The ring-down frequencies shown in (94) agree well with these predictions. Although figure 4.2 is plotted for the non-spinning case the formalism described above can be easily generalized.

It has been shown (81; 105; 107) to be useful to understand un-modeled time-frequency evolutions in gravitational-wave analysis in terms of time-frequency volumes, $\Delta f \, \Delta t$. This concept can provide insight into the merger epochs of various systems. We will consider three timescales for the merger 1) the Newtonian free fall time scale t_{ff}, 2) the quadrupole radiation time scale t_{quad} and 3) the time scale of a test particle following its geodesic just inside the ISCO of the Kerr space-time (corresponding to the merger product). For comparison we also plot the time-frequency volumes found from the figures in (94). The Newtonian free fall
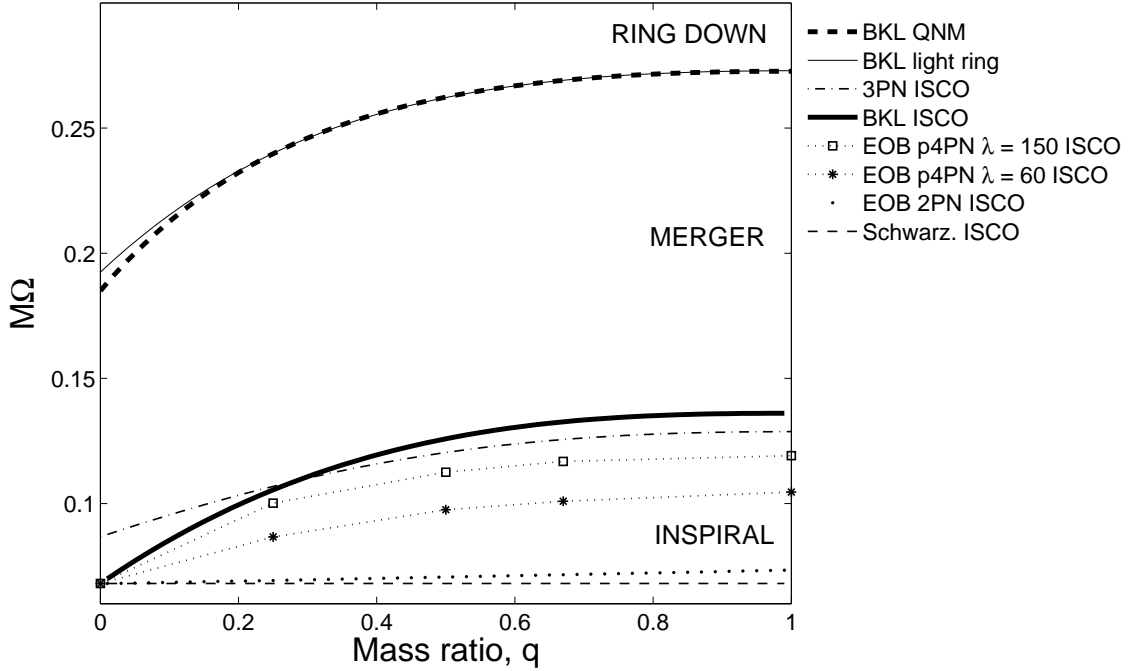
Figure 4.2: ISCO and QNM frequency estimates for non-spinning binaries as a function of mass ratio using different methods. Knowing the final spin of the black hole gives the expected ring-down frequency which agrees with the light ring frequency. The ISCO frequencies are very different depending on the method. The PN minimum energy condition gives an inconsistent result in the extreme mass ratio limit whereas the the other methods (EOB, BKL) agree with the Schwarzschild ISCO at small values of q. The ISCO and QNM frequencies define a natural merger epoch which can be analyzed, albeit sub-optimally, even without knowing the numerical waveform.

time-frequency volume is,

$$\Delta f_{\text{ISCO}} \, \Delta t_{\text{ff}} = \frac{2^{-3/2}}{\sqrt{M\Omega_{\text{ISCO}}}} \quad . \tag{4.9}$$

The quadrupole time-frequency volume is calculated by assuming that an ISCO doesn't exist and that the system continues to be driven by radiation. To calculate this we use the quadrupole approximation to the inspiral waveform given by (106), which gives the frequency evolution as,

$$M\Omega = \left[\frac{5(1+q)^2}{256\,q} \frac{M}{t - t_o} \right]^{3/8} \tag{4.10}$$

This leads to the time frequency volume,

$$
\begin{aligned}
\Delta f_{\text{BKL\,ISCO}}\,\Delta t_{\text{quad}} \;=\; & \frac{5\,(1+q)^2}{256\,\pi\,q}\left[(M\Omega_{\text{ISCO}})^{-8/3}-(M\Omega_{\text{light}})^{-8/3}\right] \\
& \times\left[(M\Omega_{\text{light}})-(M\Omega_{\text{ISCO}})\right] \quad,
\end{aligned}
\tag{4.11}
$$

where the ISCO frequencies and light ring frequencies are obtained from the BKL approximation as in figure 4.2.

The merger evolution will not be purely dominated by radiation by virtue that there are no circular orbits below the ISCO. The numbers obtained by this estimate should greatly over predict the time scale for extreme mass ratios where particles would take an asymptotically infinite time to fall in. The free fall time scale will under predict the time since the system may still complete some (unstable) orbits before merging. The estimate that agrees best with numerical relativity simulations is the infall time of a test particle falling from a circular orbit just below the ISCO to the light ring of the the merged Kerr black hole. Figure 4.3 shows the time-frequency volume for the merger epochs as a function of mass ratio for non-spinning binaries. The figure shows that the numbers taken from the simulations presented in (94) agree well with the predictions from the test particle in the Kerr space-time. By these estimates the mergers from yet un-simulated evolutions (low mass ratio) are likely to have the largest time frequency content and searches may benefit from the numerical simulations of these (105). This information should be useful in conducting IMR searches and also in guiding the construction of analytic full waveform models. It is of course possible to repeat this analysis for arbitrary spin configurations using the above prescription and others (92; 99; 100; 108). We will leave further discussion of these matters to future work and will spend the rest of this work considering the implications of using the ISCO found from the above set of equations as a termination frequency for PN waveforms in initial LIGO data analysis.
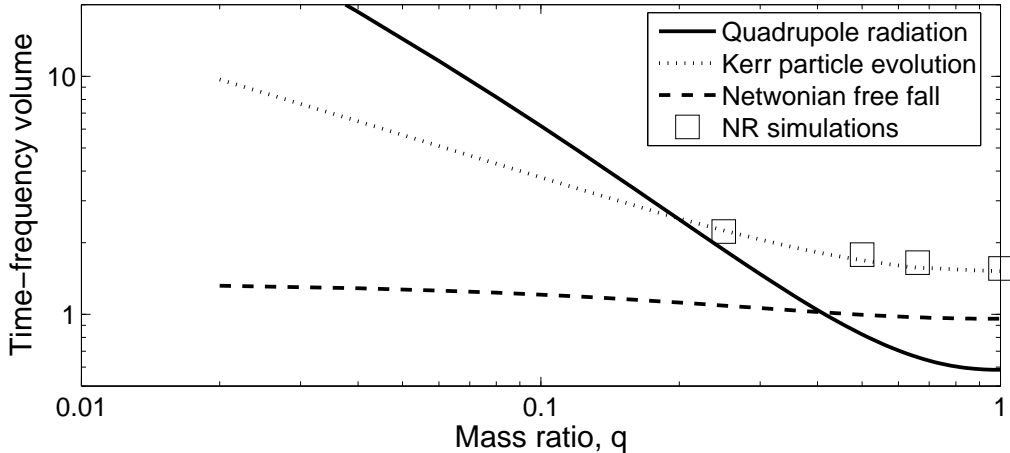
Figure 4.3: An estimate of the time-frequency volume for the merger epoch of non-spinning binary black holes. Numerical relativity results agree well with the time-frequency volume of a test particle falling into the merged Kerr black hole from a circular orbit just inside the ISCO.

4.3 Possible Impact on Data Analysis for the Inspiral Phase of Compact Binary Coalescence Searches

As mentioned previously, there is ambiguity on how to define when the inspiral phase ends. However, what is really necessary is the characteristic frequency at which a given template waveform ceases to resemble the true waveforms, assumed to be well approximated by numerical simulations.. Some searches for low mass binary systems of non-spinning component masses use the ISCO of a test particle orbiting a Schwarzschild black hole (47). Other searches use the ISCOs calculated from explicit PN energy considerations, and some abandon the use of an ISCO altogether and use the Schwarzschild light ring as a termination frequency (93).

For low mass ratio ($q \sim 0$) systems of non-spinning objects, the Schwarzschild test particle limit is a good approximation for the expected ISCO frequency since the merger product will be a Schwarzschild-like black hole. However, for systems with comparable masses and/or spin the true ISCO frequency may be different since the non-trivial contribution from the orbital angular momentum will have a strong impact on the final black hole's spin, and the spacetime in the near merger epoch. Many have addressed how well various PN approximants stay faithful to numerical relativity solutions(117; 90). Most approximants stay faithful through the Schwarzschild ISCO frequency (117). Some approximants fare extremely well beyond this point (117).

The fact that some approximants do remain faithful far beyond the Schwarzschild ISCO leads us to examine using the ISCO frequency described in the previous section, equation (4.5), as the termination frequency for inspiral data analysis. As shown, this frequency is consistent with some of the PN and EOB models for predicting the ISCO in the equal mass regime (fig. 4.2) and is consistent with exact solutions in the test particle limit. It also has the advantage of being waveform model, or fit, independent (based on first principles) and is easy to calculate. We will conservatively model the impact of possible phase errors incurred by using an approximant that doesn't quite match numerical relativity results in our assessment.

We use the stationary phase approximation waveforms, which are often employed in searches, and can be defined as,

$$\tilde{h}(f) \;\; \propto \;\; f^{-7/6} e^{i\Psi(f;M,\mu)} \;\; , \tag{4.12}$$

where M is the total mass and μ is the reduced mass (47). In order to ascertain the phase fidelity we turn to comparisons given in (90) which show for equal mass binary simulations the phase difference between numerical results and 3.5 PN waveforms as a function of frequency. The figures in (90) indicate a good fidelity in phase through the Schwarzschild ISCO frequency. However substantial phase errors may accumulate between the Schwarzschild and BKL ISCO frequencies. In order to accurately predict the impact of integrating PN waveforms to the BKL ISCO we decided to model the possibility that secular phase errors could be $\pm\pi$ or more radians between the Schwarzschild and BKL ISCOs. We propose calculating the SNR ratio of an ensemble of waveforms where phase errors are allowed to accumulate linearly between the Schwarzschild ISCO $f_2(M,q)$ and the BKL ISCO $f_1(M,q)$ given by,

$$\frac{\mathrm{SNR}_{f_1}}{\mathrm{SNR}_{f_2}} = \left\langle \left(\int_{f_{\mathrm{low}}}^{f_1} \frac{e^{\pi i R_n (f_1 - f_2)/f_1 \, \Theta(f_1 - f_2)} \, \mathrm{d}f}{f^{7/3} \, S_n(f)} \right)^{1/2} \left(\int_{f_{\mathrm{low}}}^{f_2} \frac{\mathrm{d}f}{f^{7/3} \, S_n(f)} \right)^{-1/2} \right\rangle \;\; , \tag{4.13}$$

where R_n is a normally distributed variable with mean 0 and variance 1. f_{low} is 40Hz (16). [2] We note that the above calculation is a conservative estimate of the SNR gain for two reasons: 1) A template with different parameters may match the numerical waveforms better, producing better phase agreement. Since search results are maximized over SNR this is an important possibility. 2) The phase errors do not accumulate linearly between these frequencies, most of the phase error occurs near the BKL ISCO. Using the $\{M, q\}$ dependent ISCO frequencies as $f_1(M, q)$ and the Schwarzschild ISCO frequencies as $f_2(M)$ we plot the expected SNR ratio for initial LIGO (109) in figure 4.4, which shows that for some total mass and mass ratio combinations there is an appreciable gain in SNR by integrating to the new ISCO frequencies despite modeled phase errors. This calculation is not intended to suggest that SPA templates cut at the BKL ISCO produce the optimal gain in SNR, since other approximants or frequency cut offs could do better. Instead, it aims to simply illustrate the effect of integrating to the BKL ISCO as a function of M and q for present searches. The mass range is limited to 80 $M_\odot$ so that at least two cycles exist in the waveform between 40Hz and the Schwarzschild ISCO frequency.

4.4 Conclusion

The estimate for the spin of the black hole that results from BH-BH, BH-NS, and some NS-NS mergers found in (92) leads to an estimate for the ISCO, light ring, and quasinormal mode ringdown frequencies of a general compact binary system that is waveform model independent. Both frequencies have impact on searches for the inspiral, merger and ring-down epochs of the gravitational-waves emitted by these systems. We have shown that the most interesting merger-epoch time-frequency volumes are for extreme mass ratios. More work may have to be done to model merger epochs for these systems. The formalism presented here to describe inspiral, merger and ring-down epochs can be extended to arbitrary spin configurations and may help guide the construction of better analytic models.

As for inspiral epoch searches alone, we have shown that for symmetric mass, non-spinning systems with greater than 45 $M_\odot$ total mass there can be a 30% gain in SNR over using the Schwarzschild ISCO radius as is done currently (47) even including conservative phase errors. It is worth noticing that more general fittings can be computed in order to cover the full range of parameters (q, χ_1, χ_2) within the BKL approximation.

As discussed in chapter 2, increasing the SNR will increase the sensitivity of a search. Sensitivity can also be increased by reducing the false alarm rate and lowering the loudest event. The remaining two chapters will discuss ways to lower the false alarm rate by using dataquality vetoes and signal based vetoes respectively.

---

[2]We take $S_n(f)$ to be approximated analytically as,

$$S_n(f) \approx 9 \times 10^{-46} \left[\left(\frac{4.49f}{150} \right)^{-56} + 0.16 \left(\frac{f}{150} \right)^{-4.52} + 0.32 \left(\frac{f}{150} \right)^2 + 0.52 \right] \quad . \tag{4.14}$$
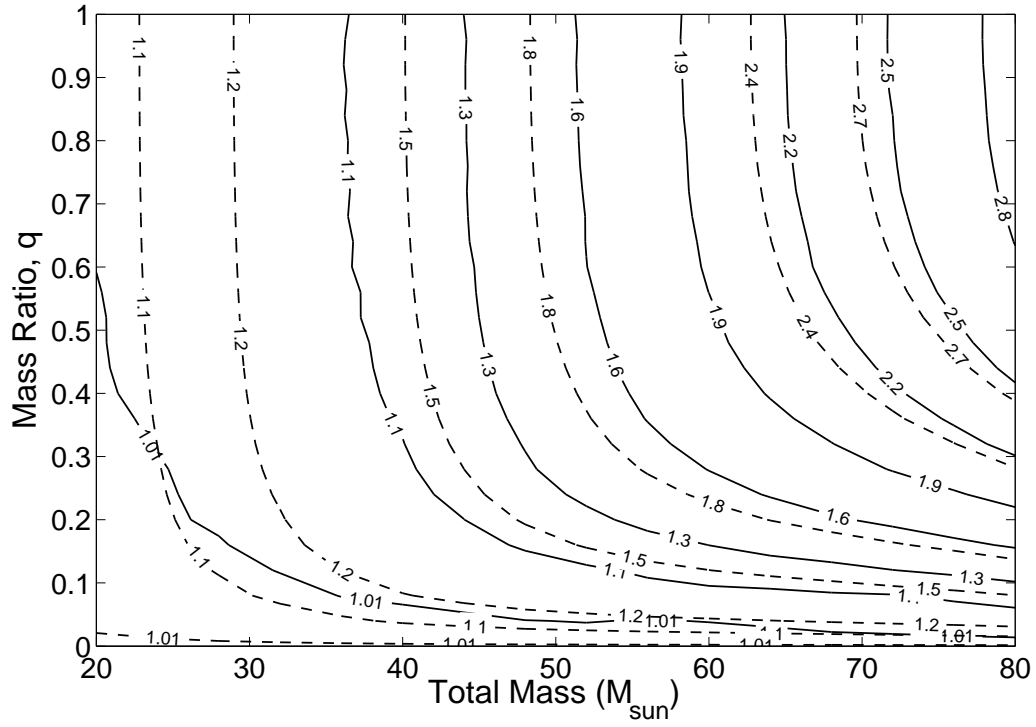
Figure 4.4: The SNR ratio defined by equation (4.13) for the non-spinning case $\chi = 0$. The solid lines include phase errors of the form (4.13) whereas the dashed lines assume perfect phase coherence for comparison.

5. Reducing Gravitational-Wave False Alarms Using Signals at the Antisymmetric Port in LIGO Detectors[1]

5.1 Introduction

Chapter 3 described a key part to interpreting the results of LIGO CBC searches. Chapter 4 provided a way to improve on such searches by altering the model for matched filter templates. This chapter will also discuss how to improve compact binary coalescence searches by reducing false alarms.

As described in chapter 2 the LIGO detectors are sensitive to gravitational-waves but also to disturbances from non-stationary noise sources, commonly referred to as glitches. Chapter 2 discussed the use of data quality vetoes to reject glitches, which are responsible for coincident false alarms. This chapter goes in depth on a specific data quality test. Signal based vetoes were also shown to be powerful discriminators of glitches in chapter 2. The following chapter will go in depth on three types of signal based vetoes.

Even though glitches rarely happen in coincidence between detectors, they may still be coincident with triggers generated from Gaussian noise in other detectors. Accuracy in distinguishing a real GW signal from a glitch is thus necessary for confidence in detection and for setting the best possible rate upper limits.

Since LIGO started taking scientific data, researchers have proposed various methods of using the LIGO's auxiliary channels that record signals from internal sources (such as control servo problems, laser noise, optical misalignments, analog-to-digital converter overflows) and external sources (earthquakes, wind) to reduce the false alarm rate (121; 84; 48; 122; 123). It is difficult to generalize the use of auxiliary channels without risk of false dismissal. This is because glitches have widely varying effects depending on the search method and waveforms that are being searched for. Since LIGO is constantly undergoing improvements, the non-stationary noise sources change character regularly. Therefore, glitch studies must be tailored to specific searches and run periods with a specific set of auxiliary channels (121; 123).

The veto described here uses a specific auxiliary channel to eliminate false alarms for the binary neutron star (BNS) inspiral search (84; 48). It is one example of many possible auxiliary channel vetoes. We will show that glitches in this channel that are coincident with BNS triggers (times when a BNS waveform template has sufficient overlap with the gravitational-wave signal resulting from matched filtering) can be marked as false alarms in a way that minimizes the chance of false dismissal. A similar veto was previously developed and used by members of the British-German GEO600 detector collaboration (123).

5.2 LIGO Modulated Read-Out Scheme

LIGO is a power recycled Fabry-Perot, Michelson interferometer. For the purpose of this chapter I will refer to figure 5.1, which shows a simple Michelson interferometer with two 4km Fabry-Perot cavities in each arm. LIGO's laser input field can be approximated as a

---

plane wave, which is phase modulated such that the field amplitude is (120)

$$
\begin{aligned}
E_{\text{in}}(t) &= E_0 \left[e^{i\omega t + i\Gamma \cos[\Omega t]} \right] & (5.1) \\
&\approx E_0 e^{i\omega t} \left[1 + i\Gamma \cos[\Omega t] \right] & (5.2) \\
&= E_0 e^{i\omega t} \left[1 + i\frac{\Gamma}{2} e^{i\Omega t} + i\frac{\Gamma}{2} e^{-i\Omega t} \right] & (5.3)
\end{aligned}
$$

where the last line holds for small modulation depth, $\Gamma \ll 1$. The result is three fields: a carrier and two sidebands. These fields enter the Michelson interferometer and are split into two arms each providing a possibly different optical path $L1$ or $L2$. Instead of conventional mirrors in the Michelson arms LIGO employs Fabry-Perot cavities. The carrier is resonant in the Fabry-Perot cavities but the sidebands are anti-resonant. The gravitational-wave strain induces a phase ϕ_h on the carrier in the Fabry-Perot cavity that is many orders of magnitude greater than the gravitational-wave phase introduced in the Michelson. Thus only the carrier picks up a differential phase of ϕ_h from a passing gravitational-wave.

I'll introduce a change of coordinates; $2L1 = L + \Delta L$ and $2L2 = L - \Delta L$. The fields that recombine at the beam splitter are then (119),

$$
E_1 = i\frac{E_0}{2} e^{i\omega t - ikL} \left[e^{-ik\Delta L - \phi_h} + i\frac{\Gamma}{2} e^{i\Omega t - ik\Delta L - ik_m(L+\Delta L)} + i\frac{\Gamma}{2} e^{-i\Omega t - ik\Delta L + ik_m(L+\Delta_L)} \right] (5.4)
$$

$$
E_2 = i\frac{E_0}{2} e^{i\omega t - ikL} \left[e^{ik\Delta L + \phi_h} + i\frac{\Gamma}{2} e^{i\Omega t + ik\Delta L - ik_m(L-\Delta L)} + i\frac{\Gamma}{2} e^{-i\Omega t + ik\Delta L + ik_m(L-\Delta_L)} \right] (5.5)
$$

where $k = \omega/c$ and $k_m = \Omega/c$. The combined fields are,

$$
\begin{aligned}
E_1 + E_2 &= i\frac{E_0}{2} e^{i\omega t - ikL} \Big\{ 2\cos\left(k\Delta L + \phi_h\right) \\
&\quad + i\Gamma e^{i\Omega t - ik_m L} \cos\left[(k + k_m)\Delta L\right] \\
&\quad + i\Gamma e^{-i\Omega t + ik_m L} \cos\left[(k - k_m)\Delta L\right] \Big\} & (5.6)
\end{aligned}
$$

The photo detector measures the power of the light field. In order for LIGO to operate on a dark fringe the carrier power should be zero in the absence of a gravitational-wave. This corresponds to $k\Delta L = \pi/2 + 2n\pi$. This simplifies the combined fields,

$$
\begin{aligned}
E_1 + E_2 &= i\frac{E_0}{2} e^{i\omega t - ikL} \Big\{ 2\sin\left(\phi_h\right) + i\Gamma (e^{i\Omega t - ik_m L} - e^{-i\Omega t + ik_m L}) \sin\left[k_m \Delta L\right] \Big\} \\
&= iE_0 e^{i\omega t - ikL} \Big\{ \sin\left(\phi_h\right) + \Gamma \sin\left[-\Omega t + ik_m L\right] \sin\left[k_m \Delta L\right] \Big\} & (5.7)
\end{aligned}
$$

The power is,

$$
\begin{aligned}
P &= |E_1 + E_2|^2 \\
&= E_0^2 \sin^2(\phi_h) \\
&\quad + 2\Gamma E_0^2 \sin\left(\phi_h\right) \sin\left[-\Omega t + ik_m L\right] \sin\left[k_m \Delta L\right] \\
&\quad + \Gamma^2 E_0^2 \sin^2\left[-\Omega t + ik_m L\right] \sin^2\left[k_m \Delta L\right] \\
&\approx E_0^2 \phi_h^2 + 2\Gamma E_0^2 \phi_h k_m \Delta L \sin\left[-\Omega t + ik_m L\right] + \Gamma^2 E_0^2 (k_m \Delta L)^2 \sin^2\left[-\Omega t + ik_m L\right] (5.8)
\end{aligned}
$$
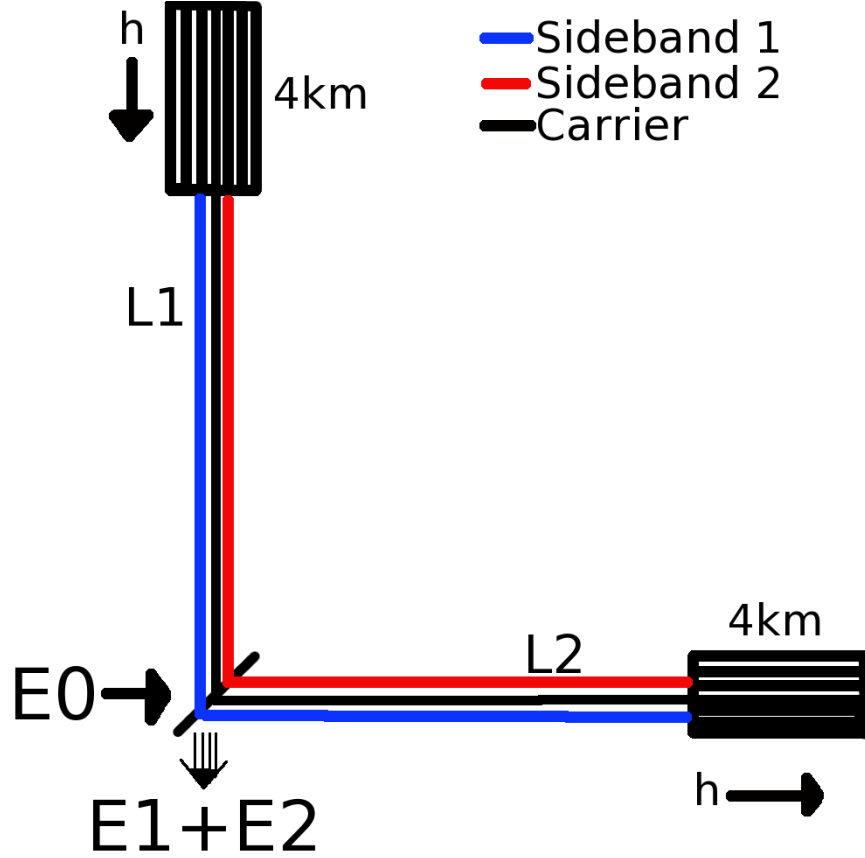
Figure 5.1: Simplified geometry of LIGO's Michelson interferometer with non-symmetric arm lengths and Fabry-Perot end mirrors. The input field E_0 is transformed into 2 output fields E_1, E_2 by the different optical path lengths in each arm. Part of the path difference, $L_1 - L_2$ is a fixed distance known as the Schnupp Asymmetry (126). The other difference is a phase delay ϕ_h caused by the gravitational-wave strain and only *appreciably* occurs in the Fabry-Perot cavites, where the carrier is resonant, but the sidebands are not.

The phase of the oscillator can be tuned to make up for the phase caused by the optical path. After this tuning the above expression is now "in phase" with the oscillator.

$$P = E_0^2 \phi_h^2 + 2\Gamma E_0^2 \phi_h k_m \Delta L \cos[\Omega t] + \Gamma^2 E_0^2 (k_m \Delta L)^2 \cos^2[\Omega t] \tag{5.9}$$

The modulation term (with $\Gamma \cos(\Omega t)$) provides first order sensitivity to the gravitational-wave. The photo current containing the possible gravitational-wave signal must be demodulated using the reference oscillator in order to record a signal that can be calibrated as the strain. The technical details can be found in (124; 125).

The demodulation produces two signals. The first signal is called the ASQ channel. The other is called the ASI channel. Only the terms which are linear in $\cos[\Omega t]$ will contribute.

$$
\begin{aligned}
\mathrm{ASQ} &= \langle \int P \cos(\Omega t)\,\mathrm{d}t \,\rangle \\
&= \frac{1}{\tau} \int_0^\tau 2E_0^2 \Gamma \phi_h k_m \Delta L \cos^2\left(\Omega t\right)\mathrm{d}t \\
&= E_0^2 \Gamma \phi_h k_m \Delta L
\end{aligned}
\tag{5.10}
$$

$$
\begin{aligned}
\mathrm{ASI} &= \langle \int P \sin(\Omega t)\,\mathrm{d}t \,\rangle \\
&= \frac{1}{\tau} \int_0^\tau 2E_0^2 \Gamma \phi_h k_m \Delta L \cos\left(\Omega t\right)\sin\left(\Omega t\right)\mathrm{d}t \\
&= 0
\end{aligned}
\tag{5.11}
$$

Only the ASQ channel should contain a signal proportional to the gravitational-wave. However, imperfections in the demodulation process leave a residual component in the ASI channel. If this imperfection is modeled as a phase error δ then the above expressions become,

$$
\begin{aligned}
\mathrm{ASQ} &= \frac{1}{\tau} \int_0^\tau 2E_0^2 \Gamma \phi_h k_m \Delta L \cos\left(\Omega t\right)\cos\left(\Omega t + \delta\right)\mathrm{d}t \\
&\approx (1 - \delta^2) E_0^2 \Gamma \phi_h k_m \Delta L
\end{aligned}
\tag{5.12}
$$

$$
\begin{aligned}
\mathrm{ASI} &= \frac{1}{\tau} \int_0^\tau 2E_0^2 \Gamma \phi_h k_m \Delta L \cos\left(\Omega t\right)\sin\left(\Omega t + \delta\right)\mathrm{d}t \\
&\approx \delta E_0^2 \Gamma \phi_h k_m \Delta L
\end{aligned}
\tag{5.13}
$$

where the approximations are valid for $\delta \ll 1$.

Diluted gravitational-wave signals are not the only things recorded in the ASI channel. The ASI channel may also record signals produced by amplitude noise, reference oscillator phase noise and electronics noise, as well as signals produced by alignment fluctuations in the suspended optical components.

5.3 Vetoing False Alarms Produced by ASI Glitches

One must be able to distinguish with confidence between glitches that produce ASI noise and a real GW signal that can also produce a signal in ASI. The ASI/ASQ channel coupling function is known to be weak (and is measurable in different ways) (123). This justifies the small phase error expansion in equation 5.10. The phase error in the demodulation is typically less than 0.10 rad. This gives a predicted ratio of order 10

$$
\frac{\mathrm{ASQ}}{\mathrm{ASI}} = \frac{1 - 0.1^2}{0.1} \sim 10,
\tag{5.14}
$$

whereas instrumental transients that appear in both quadratures may produce amplitude ratios of order 1 or less. Thus it is possible to determine if BNS triggers are caused by glitches by carefully comparing the amplitude ratios of the ASQ and ASI channels.

In order to utilize the resources available from other veto studies, we choose to use a wavelet analysis algorithm called Kleinewelle (127). Kleinewelle defines an excess energy
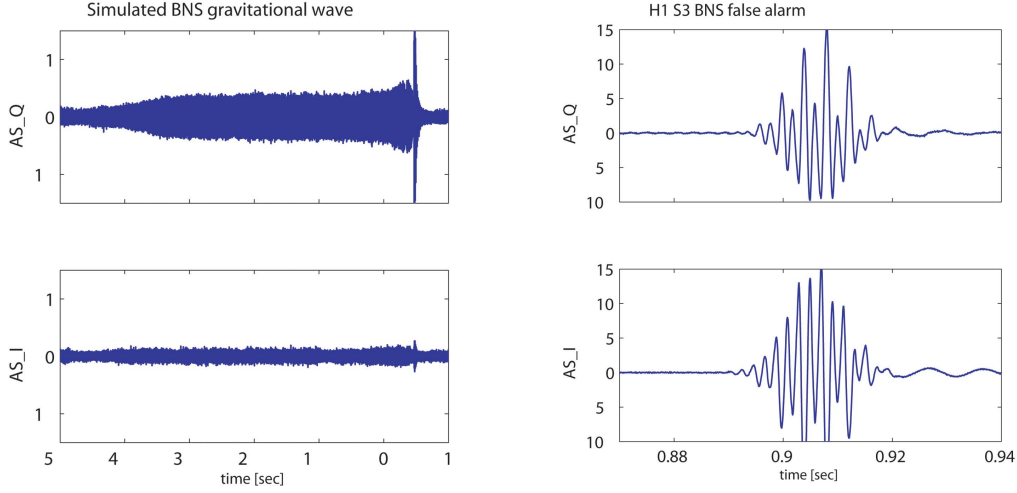
Figure 5.2: We plot ASQ and ASI time series from data taken with the H1 detector during S3, high-pass filtered at 100Hz. On the left is data taken during the hardware injection of a BNS GW signal. On the right is a glitch which triggered a BNS analysis pipeline false alarm (or false trigger). For the simulated GW, the ASQ channel has an amplitude about 5 times greater than for the glitch. The glitch has roughly equal amplitudes in both channels which is a sign that it is likely a false alarm.

in the ASI and ASQ data channels, and generates triggers when this excess energy exceeds a predefined threshold. We define the ratio of ASQ/ASI trigger energies produced by Kleinewelle to be κ.

$$\kappa \equiv \frac{\text{ASQ energy}}{\text{ASI energy}} \tag{5.15}$$

It is common practice to simulate a gravitational-wave by injecting a theoretical waveform into the hardware (by actuating on the end mirrors using the control system) and performing normal analysis procedures (55). Hardware injections are useful in validating detection methods and characterizing the detector. In our case, it provides us with an upper limit of the ratio of gravitational-wave signal in the ASQ and ASI channels.

The left panel in Figure 1 depicts the raw time series of a simulated gravitational-wave in the uncalibrated ASI and ASQ channels. It is clear from the time series that the amplitude of ASI is less than ASQ. The case is quite different for the right panel plots which display a noise glitch found in both ASI and ASQ data streams in coincidence with similar channel amplitudes. This glitch is consistent with noise that we would like to veto.

In order to quantify these amplitude differences, we use the Kleinewelle algorithm to detect simulated gravitational waves and glitches in both ASQ and ASI datastreams. Kleinewelle produces triggers with excess energy corresponding to many types of glitches, and provides some frequency and duration information as well. We require that an ASI Kleinewelle trigger occurs within ± 1 second of the end of a hardware injection. We also require the ASI Kleinewelle trigger to have an ASQ counterpart within ± 0.3 seconds of the ASI trigger. In Figure 2 we show that simulated gravitational waves have an energy ratio κ greater than two for all ASI triggers above an energy of 1.5. This result is smaller than the prediction
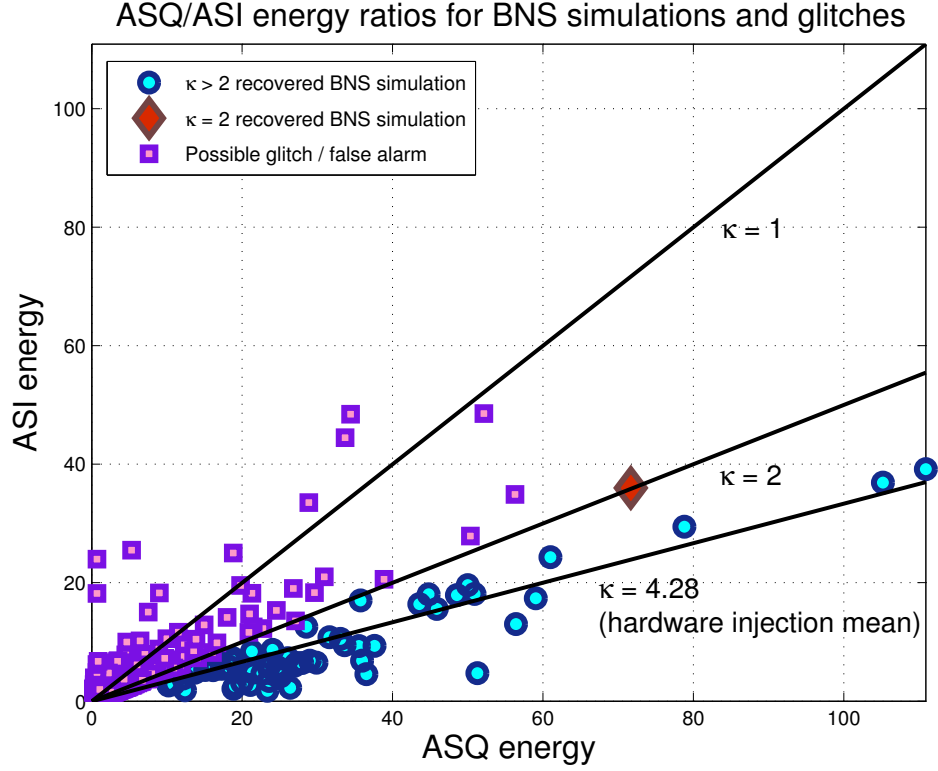
Figure 5.3: We compare the output of the Kleinewelle analysis algorithm for the ASI and ASQ channels at times of hardware injections of simulated inspiral signals and times of glitches. All simulations have an ASQ/ASI ratio greater than or equal to two. Therefore triggers with ratios less than two (about 2/3 of the above ASI KW triggers coincident with BNS triggers) may be false alarms.

based on the phase error in equation 5.14. Although the real reason for the lower than expected κ has not been studied. Frequencies below 200Hz could be effected by the lack of calibration. It has been conjectured that imperfections in the hardware injection process cause misalignments that increase the power in ASI. Thus we expect the ratio of two to be a worst case scenario for real GW's and conclude that BNS triggers that are coincident with Kleinewelle triggers having κ less than two should be considered false alarms.

5.4 Application to S3 Search for Binary Neutron Star Systems

A lack of GW simulations in the Livingston detector and the presence of a different successful veto for the H2 detector (121) constrains our examination to H1 data. As described in Section 3, the ratios of ASQ/ASI energies are determined by studying data taken during hardware injections. We also need to determine a threshold on the absolute magnitude of the ASI energy that should be considered a veto trigger. Therefore we define

$$E_0 \equiv min(\text{ASI Kleinewelle energy for veto trigger}). \qquad (5.16)$$

In order to explain the need for E_0 it is useful to define a few quantities:

use percentage - number of Kleinewelle ASI veto triggers that veto BNS triggers divided by the total number of veto triggers available (normalized to 100%.)

efficiency - number of vetoed BNS triggers divided by the total number of BNS triggers (normalized to 100%.)

veto window - coincidence window between a Kleinewelle ASI trigger and a BNS trigger within which the ASI veto may be applied.

dead time - amount of time which is excluded by the veto divided by the total amount of time analyzed (normalized to 100%.) Ignoring any possible overlaps, the dead time is approximately given by

$$deadtime \propto (\text{veto window}) * (\text{number of Kleinewelle ASI veto triggers}) \qquad (5.17)$$

As the energy threshold E_0 is reduced, the amount of time containing glitches becomes so large that they cease to be associated with BNS triggers, and the dead time approaches 100%. Eventually the number of identified glitches becomes large enough to lose correlation with BNS triggers. The **use percentage** becomes small. In general we want **use percentage** to be large compared to **dead time**. Maximizing **use percentage** and **efficiency** while simultaneously minimizing **dead time** gives the appropriate energy threshold for the ASI channel E_0 (122). Following this procedure we set $E_0 \equiv 1.5$, which produces a **use percentage** $\sim 80\%$ and **dead time** $< 2\%$.

Beyond E_0, the only remaining parameter to establish is the **veto window**. Glitches are often brief (~ 1 second), but BNS triggers occur in large clusters around those times since. glitches can be like delta functions in time compared to the typical length of the search templates described in chapter 2. There can be an excellent overlap with any template waveform in the search template bank. The templates in general will give a range of end times spanning several seconds. We find a strong correlation between Kleinewelle ASI triggers and high signal-to-noise (SNR) BNS triggers within a time window of [-1, +8] seconds.

Figure 3 shows the **veto window** superimposed over BNS triggers. The green diamond is the time of an ASI glitch trigger (as found by Kleinewelle). BNS triggers with high SNR are coincident with the glitch within a fraction of a second. There is a tail of lower SNR BNS triggers that follow the glitch according to the response of the filter discussed in chapter 2 and should also be excluded.
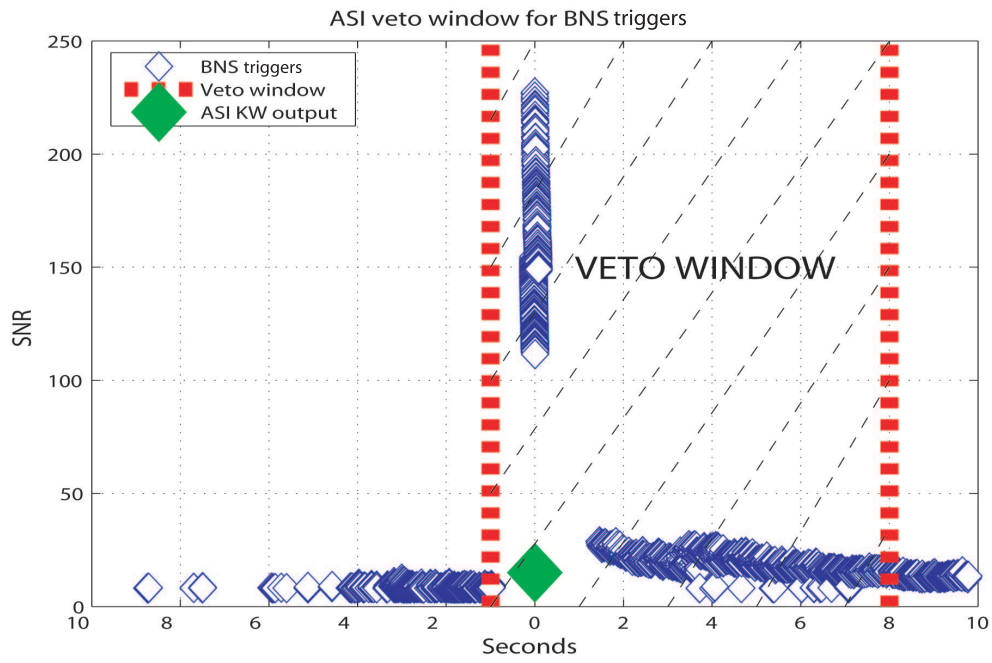
Figure 5.4: The SNR of BNS triggers found in the LIGO S3 data from H1, versus the time between the BNS trigger and the nearest Kleinewelle ASI glitch trigger. The high SNR BNS triggers are coincident with the glitch found in the ASI channel. There is also a tail of lower SNR triggers at larger values of the time difference.
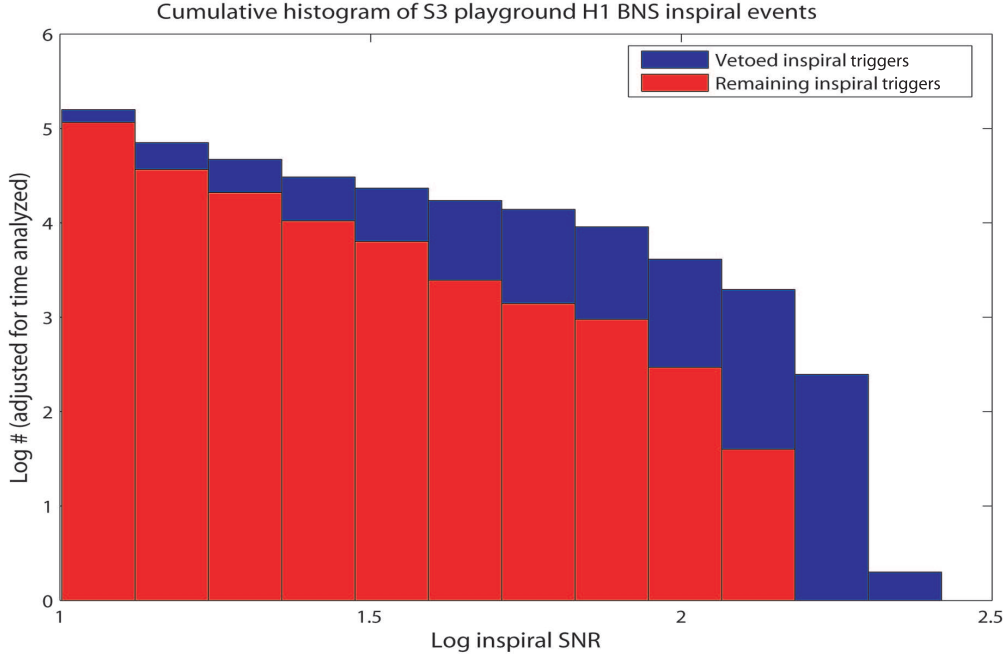
Figure 5.5: A cumulative histogram of the number of BNS triggers in the S3 playground data from the H1 detector versus the threshold on the BNS trigger SNR (upper histogram). Many of the high SNR BNS triggers are coincident with ASI glitches, with values of κ consistent with noise glitches, and can be vetoed; unvetoed triggers are in the lower histogram.

5.5 Results

Every LIGO science run has designated a **playground** which has approximately 10 percent of the science run data allocated for tuning search parameters and identifying useful vetoes. The ASI veto was very successful at vetoing high SNR BNS false alarms as indicated by Figure 4. This log scale cumulative histogram demonstrates that about one-third of the BNS triggers above SNR 20 were vetoed by our method during the **playground** time (these were also false alarms because of lack of coincidence with any other GW detectors and failure to pass the χ^2 test (48)).

We used this ASI veto for the full dataset analysis of S3 BNS in LIGO's H1 detector. We identified approximately 1000 false alarm triggers in S3 science run data using the ASI channel. A similar strategy was used for S4 searches (40).

LIGO's auxiliary channel (ASI) dismissed a large number of false BNS triggers in the S3 BNS search by exploiting the known coupling of simulated gravitational-waves to the ASI channel. Instrumental vetoes are powerful tools but cannot negate the effects of all glitches in the searches for compact binary coalescence. The next chapter will discuss veto strategies based only on the gravitational wave signal whereby the data is explicitly checked for consistancy with the templates used in the search. Such signal-based vetoes tend to have excellent discriminative power.

6. Computationally Efficient χ^2 Tests for Gravitational-Wave Searches

6.1 Introduction

The last chapter described how to reduce false alarms in searches for compact binary coalescence with data quality vetoes. This chapter will describe several signal based vetoes, one of which was discussed in chapter 2.

Gravitational-wave searches that employ matched filtering would have a well defined false trigger rate in Gaussian, stationary noise (82). As described in chapter 2 each filter produces a signal-to-noise ratio (SNR) time series. When a filter crosses a predetermined threshold, and a local maximum is found, a trigger is recorded (47). The higher a trigger's SNR the less likely it is to be caused by Gaussian, stationary noise and a sufficiently high SNR trigger will clearly stand above the background expected from Gaussian noise. Unfortunately presence of transient signals that are not gravitational-waves, called glitches, can increase the background significantly over what is expected from Gaussian noise (84; 48; 85; 16). In this case the matched filter SNR alone is no longer a measure of significance. It is necessary to find robust methods of distinguishing these false triggers caused by transients from triggers caused by real signals (121). The previous chapter described a way to do this based on auxiliary channels recorded by the LIGO instrument. This chapter will describe methods based only on the data and the expectations of a real signal as determined by injections. These methods, referred to as signal based vetoes, were described in chapter 2, such as the χ^2 and r^2 tests. These signal based vetoes can be contrasted to the data quality vetoes introduced in chapter 2 and 5, which are often related to correlations with environmental or instrumental monitors.

The χ^2 test is used to check how well data matches the expected signal (128) This test can help in determining whether a trigger is from a real signal or a transient. Transients tend to have χ^2 values that are significantly higher than the expectation from noise in a quantifiable way. There is more than one way to construct a χ^2 test in large scale matched filter searches such as those described in chapter 2. This chapter will explore three unique χ^2 tests, one that has been used in LIGO searches previously (56) and two new computationally efficient tests introduced here for the first time. The tests differ in their efficacy and computational cost.

In order to evaluate how effective the χ^2 tests are at rejecting glitches and how safe they are at retaining signals we rely on simulations of real signals. Simulations are done by digitally injecting waveforms of the appropriate type and amplitude into the data as it is read by the analysis software. Thousands of such "software injections" are done in order to ascertain how a χ^2 test responds to real signals. In addition to software injections we tested Gaussian Noise and simulated detector data.

This chapter is organized as follows. First I will review matched filtering and establish some notation. Next I will discuss three χ^2 tests in a unified picture. And finally I will show the results of all three tests on simulated data, and LIGO S4 data.

6.2 Formalism

Gravitational-wave detector data $s(t)$ is typically represented as a time series of finite duration made of two components

$$s(t) = n(t) + h(t) \tag{6.1}$$

where n(t) is Gaussian, stationary noise and h(t) is a gravitational-wave signal (48). In reality the data is discretely sampled. For the purposes of this chapter it is useful to introduce a third component of the data to represent a transient. This component could be a gravitational-wave not from a compact binary coalescence or it could be an environmental or instrumental disturbance (i.e. a glitch) like those described in chapter 6. It is assumed to be short duration and will be denoted as $x(t)$. Since the data is actually discretely sampled, this work will incorporate all three components, $n(t), h(t), x(t)$ as vectors $\mathbf{n}, \mathbf{h}, \mathbf{x}$ into a data vector $\mathbf{s}$,

$$\mathbf{s} = \mathbf{n} + \mathbf{h} + \mathbf{x} \tag{6.2}$$

where $\mathbf{n}$ is the Gaussian, stationary noise, $\mathbf{h}$ is the gravitational-wave signal, and $\mathbf{x}$ is a transient signal and *most likely* not a gravitational-wave. Figure 6.1 shows how these three components might hypothetically appear in the data. The only guaranteed non zero contribution comes from $\mathbf{n}$. Therefore any detection algorithm must have a well understood output when its only input is $\mathbf{n}$. Furthermore the algorithm should distinguish between $\mathbf{x}$ and $\mathbf{h}$.
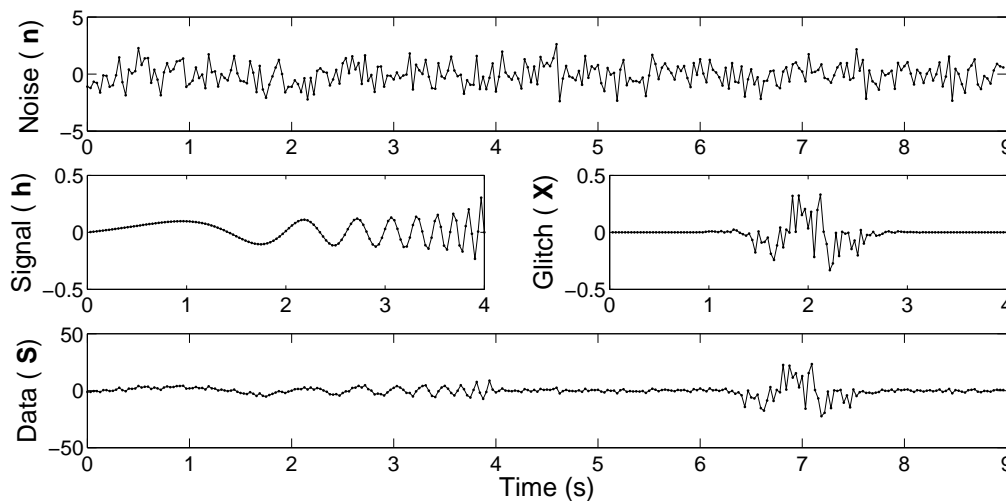
Figure 6.1: Components that may contribute to a detector data stream (exaggerated for illustration). Top: Most of the time the data stream is simply Gaussian noise $\mathbf{n}$. Center Left: A simulated binary inspiral signal $\mathbf{h}$. Center Right: A simulated transient $\mathbf{x}$. Bottom: The combination of all contributions $\mathbf{s}$.

6.2.1 Noise

The properties of the Gaussian, stationary noise ($\mathbf{n}$) are of particular interest (21). Most signal processing is based on the expectation that Gaussian noise will be present. It is necessary to understand the statistical properties of the noise and the detection algorithm in the presence of noise.

It is desirable to have the data stream in a whitened form, one that when only noise is present has equal power in all frequencies. Signal-whitening Fourier transforms the time series data $\mathbf{s}$ and divides it by its amplitude spectral density (ASD), which is the square root of the Power Spectral Density (PSD) $\sqrt{\mathcal{S}_{\mathbf{n}}}$ (47),

$$s_j \rightarrow s_k = \left[\sum_{k=0}^{N} s_k e^{-2\pi ijk/N} \right] / \left[\sqrt{N\,\mathcal{S}_{\mathbf{n}\,k}} \right] \tag{6.3}$$

(see chapters 1 and 2). If the PSD is measured over a time much greater than the duration of signals and transients then it measures the spectrum of the noise only. Often many PSD estimates are made and averaged together. The averaging process reduces the uncertainty in each frequency interval. This leads to the representation of the noise $\mathbf{n}$ part of $\mathbf{s}$ with expectation values that satisfy the properties of an orthonormal basis. The frequency domain, whitened noise can be decomposed as

$$\mathbf{n} = \sum_{k}^{N} (n_k + i\, m_k)\, \hat{\mathbf{n}}_{\mathbf{k}} \tag{6.4}$$

Each n_k and m_k has an amplitude given by the probability

$$P(n_k) = \frac{1}{\sqrt{2\pi}}\, \exp[-n_k^2/2] \tag{6.5}$$

The noise unit vectors have a zero mean and a unity variance.

$$
\begin{aligned}
\langle n_k \rangle &= 0 & \text{(6.6)} \\
\langle n_k n_l \rangle &= \delta_{kl} & \text{(6.7)} \\
\langle \hat{\mathbf{n}}_{\mathbf{k}}{}^\dagger \hat{\mathbf{n}}_{\mathbf{l}} \rangle &= \delta_{kl} & \text{(6.8)} \\
\langle \mathbf{n}^\dagger \mathbf{n} \rangle &= N & \text{(6.9)}
\end{aligned}
$$

The remainder of the chapter will work in the whitened basis unless otherwise noted. Since the whitening transformation is actually applied to $\mathbf{s}$, the signals $\mathbf{h}$ and transients $\mathbf{x}$ are also transformed, which will be important for the discussion of the optimal linear filter in the next section. For clarity let the whitened data now be written as

$$
\begin{aligned}
\mathbf{s} &= \mathbf{n} + A\,\mathbf{h} + B\,\mathbf{x} & \text{(6.10)} \\
\langle \mathbf{n}^\dagger \mathbf{n} \rangle &= N & \text{(6.11)} \\
\langle \mathbf{h}^\dagger \mathbf{h} \rangle &= 1 & \text{(6.12)} \\
\langle \mathbf{x}^\dagger \mathbf{x} \rangle &= 1 & \text{(6.13)}
\end{aligned}
$$

6.2.2 Signal

This section demonstrates that the matched filter is the optimal linear filter to find a signal $\mathbf{h}$ in noise $\mathbf{n}$ (129). In the continuous time domain, a linear filter is a convolution integral applied to the data $s(t)$

$$z(t) = \int_0^{\tau_c} L(\tau)\, s(t-\tau)\, d\tau \tag{6.14}$$

that produces a filtered time series $z(t)$. For the discrete case the filter will be a matrix operator, $\widehat{\mathbf{L}}$. A filter of the form of equation (6.14) is diagonalized by the Fourier transform. Thus in the whitened noise basis it will be diagonal, denoted as $\widehat{\mathcal{L}}$. It is also assumed to be normalized such that $\mathrm{Tr}(\widehat{\mathcal{L}}^\dagger \widehat{\mathcal{L}}) = 1$. The optimal linear filter will maximize the signal-to-noise ratio (SNR) for the desired signal $\mathbf{h}$

$$\mathrm{SNR}^2 = \frac{\text{signal power}}{\text{noise power}} \tag{6.15}$$

$$\mathbf{SNR}^2 = \frac{A^2\,|\widehat{\mathcal{L}}^\dagger \mathbf{h}|^2}{\langle |\widehat{\mathcal{L}}^\dagger \mathbf{n}|^2\rangle} = \frac{A^2\,|\widehat{\mathcal{L}}^\dagger \mathbf{h}|^2}{\langle \widehat{\mathcal{L}}^\dagger \mathbf{n}\, \mathbf{n}^\dagger \widehat{\mathcal{L}}\rangle} \tag{6.16}$$

$$= A^2\,|\widehat{\mathcal{L}}^\dagger \mathbf{h}|^2 \tag{6.17}$$

Using the Schwarz inequality we know (56),

$$|\mathcal{L}^\dagger \mathbf{h}|^2 \ \leq\ (\mathcal{L}^\dagger \mathcal{L})(\mathbf{h}^\dagger \mathbf{h}) \tag{6.18}$$

Equation (6.18) becomes an equality only when $\mathcal{L} \propto \mathbf{h}$: A "matching" filter. From here forward the optimal form of $\widehat{\mathcal{L}}$ will be denoted as $\widehat{\mathbf{h}}$.

The maximum SNR measurable from a signal of the form given by equation 6.6 is A. When $\widehat{\mathbf{h}}$ is applied to $\mathbf{s}$, which contains signal and noise, the result is the vector $\boldsymbol{\rho}$,

$$\boldsymbol{\rho} = \widehat{\mathbf{h}}^\dagger \mathbf{s} \tag{6.19}$$

$$= \widehat{\mathbf{h}}^\dagger \mathbf{n} + A\,\widehat{\mathbf{h}}^\dagger \mathbf{h} + B\,\widehat{\mathbf{h}}^\dagger \mathbf{x} \tag{6.20}$$

$$\simeq \mathbf{SNR} \tag{6.21}$$

which is approximately the SNR when there are no transients ($B = 0$) and the signal amplitude is sufficiently larger than the noise (> 1). $\boldsymbol{\rho}$ is a surrogate for the true SNR but is used interchangeably and is the one described in chapter 2. This is why noise can counter-intuitively produce a signal-to-noise ratio. Using $\boldsymbol{\rho}$ as a surrogate for $\mathbf{SNR}$ leads to nonzero absolute value of SNR that could be biased by the presence of loud transients when $\mathbf{h}^\dagger \mathbf{x} \neq 0$.

The probability distribution of $\boldsymbol{\rho}$ given Gaussian noise $\mathbf{n}$ is typically used to estimate the significance of a matched filter trigger but this only works in the absence of glitches.

$$P(\boldsymbol{\rho}\,|\mathbf{n}) = P(\mathbf{h}^\dagger\,\mathbf{n}) = \sum_{i=1}^{N} \frac{h_i}{\sqrt{2\pi}}\, e^{-n_i^2/2}$$

$$P(\rho|\mathbf{n}) = \frac{1}{\sqrt{2\pi}} \frac{1}{\sqrt{\sum_{i=1}^{N} h_i^2}} e^{-\rho^2/\left[2\sum_{i=1}^{N} h_i^2\right]}$$

$$P(\rho|\mathbf{n}) = \frac{1}{\sqrt{2\pi}} e^{-\rho^2/2} \tag{6.22}$$

This means that the probability of having ρ above some value SNR* is

$$P(\rho > \text{SNR}^*|\mathbf{n}) = \text{erfc}[\rho] \tag{6.23}$$

which is independent of the filter. For example, the number of times to expect a SNR greater than 6 for one matched filter in a year of data sampled at 4096 samples per second is

$$\begin{aligned} P(\rho > 6|\text{n}) &= \text{erfc}[6] \times 4096\text{Hz} \times 3.15 \times 10^7\text{s/yr} \\ &= 2.8 \times 10^{-6}/\text{yr} \end{aligned} \tag{6.24}$$

LIGO searches use as many as 10^4 matched filters and use a complex matched filter output. Thus the chance of finding a trigger from *any* one of these filters is actually much higher as described in chapter 2. Finding an SNR = 6 trigger in a year of data consisting only of Gaussian noise and real signals is rare and odds are the event is caused by a real signal. However the effect of transients spoils this confidence.

Before closing this section it is important to mention that although ρ is only a surrogate for SNR the two are generally used interchangeably. Furthermore the SNR is usually taken to be the absolute value of the inverse Fourier transformed ρ. This leads to a positive definite discrete time series like what is shown in figure 6.2 for a signal and a glitch. The inverse transform, although made efficient by the use of the fast-Fourier-transform (FFT) is still computationally burdensome for a large number of filters. In fact Fourier transforms tend to be the computationally limiting aspect of matched filter searches (47) that don't employ additional signal processing techniques (such as χ^2 tests). The computational cost of filtering will serve as a benchmark for comparing the costs of χ^2 tests later.

6.2.3 Transients

With the distribution of SNR from noise alone one would expect matched filtering to be very powerful at discriminating real signals from noise. This is true in the case that stray, undesired signals (transients) are not common in the data set. For gravitational-wave detector data in general that is not the case because $\widehat{\mathbf{h}}^\dagger \mathbf{x} \neq \mathbf{0}$. The ρ resulting from a transient $B\,\mathbf{x}$ is

$$\boldsymbol{\rho} = (\widehat{\mathbf{h}}^\dagger \mathbf{x})\,B \tag{6.25}$$

Consider a class of transients that are Gaussian noise bursts with significantly higher power than the noise, e.g. a variance of $\sigma_B^2 = 1000$, and happen once per day (too infrequent to bias the estimate of $\mathcal{S}_\mathbf{n}$). Then number of events above SNR 6 in a year of data is

$$\begin{aligned} P(\rho > 6|\mathbf{X}) &= \text{erfc}[6/\sqrt{1000}] \times 1/\text{day} \times 365\text{days/yr} \\ &= 145/\text{yr} \end{aligned} \tag{6.26}$$

which is 8 orders of magnitude higher than the rate from Gaussian noise alone.

In reality transients are not simply Gaussian noise bursts – though they could be. Most are difficult or impossible to characterize to the level of predicting their effects. Their rate however can be studied and their effects are known in previous searches (84; 48; 16).
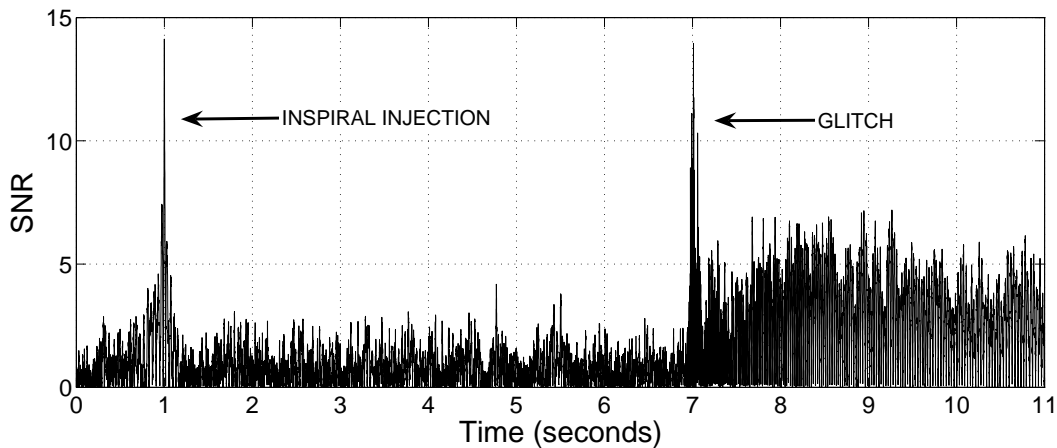
Figure 6.2: Absolute value of SNR for a simulated signal and glitch in the presence of Gaussian noise. The output of a matched filter in Gaussian noise alone has and expectation that is Gaussian distributed in SNR but both signals and glitches produce significant outliers. It is necessary to find additional ways to discriminate these signals.

6.2.4 Gravitational-Wave Matched Filter Searches

gravitational-wave searches for binary inspirals were described in detail in chapter 2. However for convenience I'll summarize a few points here.

gravitational-wave matched filter searches require far more filters than just a single $\widehat{\mathbf{h}}$. Searches may require more than 10^4 unique filters each representing a slightly different waveform arising from the different masses in compact binary system (83). Interferometric gravitational-wave detectors are not equally sensitive to all binary inspirals with similar incident flux of gravitational radiation. This is because the instruments have frequency dependent noise as in figure 1.4.

The sensitivity to a system depends on how long the system is expected to radiate in LIGO's most sensitive band ($\sim 40 - 2000$Hz) (40; 16) as shown in figure 1.4. Inspirals begin their evolution well below 40Hz. But each type of coalescence is expected to merge at very different frequencies. Some systems (e.g. $100+$ $M_\odot$ black holes) merge before ever reaching the sensitive region, and some (sub solar mass black holes) merge after they have already left. Merger frequencies can be estimated by the methods described in chapter 4. For this reason there is a clear mass upper bound that an interferometric gravitational-wave detector can detect. However merger frequency is not the only factor in determining signal duration; signal duration also depends on mass ratio. Asymmetric mass systems radiate longer in the span between 40 Hz and ISCO. A $\sim 40 M_\odot$ binary system will coalesce at ~ 100Hz for all component mass configurations, but a $\{39, 1\}$ $M_\odot$ pair lasts for over 2s, whereas an equal mass $\{20, 20\}$ pair lasts only 0.2s. Longer signals that span the same frequency range are generally more detectable.

Throughout this chapter the parameter space of signal waveforms $\mathbf{h_i}$ will be used as filters, and denoted as $\widehat{\mathbf{h_i}}$. These filters discretely cover a continuous parameter space and it

is possible that true signals will lie *in between* the filters. By imposing the condition that

$$\max[\mathbf{h_i}^\dagger \mathbf{h_j}] \geq 1 - \delta \tag{6.27}$$

the loss of SNR for such signals will be less than δ %.

The computational cost of a matched filter search with a large number of templates is dominated by the filtering stage itself. Some time is spent with data conditioning, power spectrum estimation and recording results. But for a search that has a large number of templates $\mathcal{N} \geq 1000$, the computational cost is dominated by the inverse Fourier transforms needed to produce the SNR time series. For data containing N samples the computational cost to filter $\mathcal{N}$ waveforms is $\mathcal{O}(N \log_2[N])$, typically no better than $5 \mathcal{N} N \log_2[N]$

6.3 χ^2 Tests

As discussed in the previous section the background rate for matched filter searches can be greatly impacted by the presence of transients. The remainder of this paper will describe ways to reject false alarms caused by transients.

A common method to check the consistency of a signal in data is to invoke a least-squares test on the data s(t).

$$\chi^2(t) = \int_0^{\tau_c} [s(t - \tau) - A\,h(\tau)]^2 d\tau \tag{6.28}$$

Or for a discrete time series s_i

$$\chi_j^2 = \sum_i^m (s_{j-i} - A\,h_i)^2 \tag{6.29}$$

where m is the duration of the signal in samples. If the data only contains the signal $\mathbf{h}$ then this quantity is zero. If the data contains only Gaussian noise, it will be χ^2 distributed with p degrees of freedom (this means that the expectation is $p \pm \sqrt{2p}$.)

Consider now a generalized χ^2 test of the form

$$\chi^2 = |\widehat{\mathbf{P}}_p \mathbf{s} - A\widehat{\mathbf{P}}_p \mathbf{h}|^2 \tag{6.30}$$

where $\widehat{\mathbf{P}}$ is an operator that projects $\mathbf{s}$ onto a subspace of dimension p. This has the effect of checking that the p subspace of the signal is consistent with the desired waveform. If p is allowed to be the same dimension as the waveform m then the test reduces to the conventional definition of the χ^2 test. The remainder of this section will describe three different χ^2 tests, each with a unique projection. One of these tests is already used in LIGO data analysis (56; 84; 48; 16) the others are new. I will describe the expectations and computational cost of each.

6.3.1 Conventional χ^2 Test $- \chi_C^2$

The first test discussed is quite similar to the conventional notion of a least-squares test applied to the time series data (6.29). For this reason it will be called the "conventional χ^2 test", χ_C^2. However it will be applied in a more computationally efficient way than the expression 6.29 suggests. The projection used is the identity matrix over the subspace p,

$\widehat{\mathbf{P}}_{\mathbf{p}} = \widehat{\mathbf{I}}_{\mathbf{p}}$, which is the dimension of $\mathbf{h}$ (i.e. the part of the waveform not padded with zeroes), then

$$
\begin{aligned}
\chi^2 &= |\widehat{\mathbf{I}}_p \mathbf{s} - A \widehat{\mathbf{I}}_p \mathbf{h}|^2 \\
&= \widehat{\mathbf{I}}_{\mathbf{p}} \mathbf{s}^\dagger \mathbf{s} - \rho^2
\end{aligned}
\tag{6.31}
$$

Equation (6.31) is the most efficient form of the conventional χ^2 test as it will be shown later that with careful choices it can be done with very little computational cost.

Equation (6.31) has an expectation value in Gaussian noise using (6.9),

$$
\langle \chi_C^2 \rangle_{\text{noise}} = p - 1
\tag{6.32}
$$

For sufficiently large p, which is the case for most filters, this distribution tends toward normality as indicated in figure 6.4.

The expectation value of this test will not be $p-1$, even when the desired signal is present. This is because the use of a discrete template bank means that a real signal is likely to fall in between the discretely chosen templates. Using (6.27) to parametrize the expectation for the desired signal gives

$$
\langle \chi_C^2 \rangle_{\text{signal}} = [\rho/(1-\delta)]^2 - \rho^2
\tag{6.33}
$$

$$
\langle \chi_C^2 \rangle_{\text{signal+noise}} \approx p + 2\delta\rho^2
\tag{6.34}
$$

where the last line holds for small δ, (i.e. small mismatch when the signal is very similar to the template waveform). A transient can be considered a signal with a very poor match to the template. In the spirit of (6.27) one can parametrize a transient acting on the template bank as having $\delta \lesssim 1$. For a transient the last line does not hold and typically produces large χ_C^2 values.

The cost of the conventional χ^2 test as described in (6.31) is very low by implementing the following procedure. Note that by inverse Fourier transforming the $\mathbf{s}$ part to the time domain $\mathbf{s} \to \mathbf{s}'$ and defining the series

$$
P_i = s_i' \times s_i' + P_{i-1}
\tag{6.35}
$$

the inner product $\widehat{\mathbf{I}}\mathbf{s}^\dagger\mathbf{s}$ can be computed over a space p at a time i as a subtraction and the χ_C^2 is

$$
\chi_C^2 = (P_i - P_{i-p}) - \rho_i^2
\tag{6.36}
$$

The SNR is already calculated as a time series for each filter. The cost of computing the χ_C^2 value is then simply the cost of the inverse Fourier transform of $\mathbf{s}$ plus some additional operations. This is $5\,N\,\log_2[N] + \mathcal{O}[N]$. Notice that is is the same order as *one* matched filter computation. That means that for a bank of 625 templates this test contributes $\approx 0.16\%$ to the overall computational cost. Others have suggested a similar form for the conventional chisq test, though to my knowledge have not discussed the computationally efficient method I have described or contrasted its performance directly with other methods (56; 130).

6.3.2 Template Bank χ^2 Test

The next χ^2 test that we will discuss uses p of the filter waveforms in the template bank $\{\mathbf{h}_j, \mathbf{h}_k, \mathbf{h}_l, ...\}$ to construct the $(N \times p)$ operator $\widehat{\mathbf{P}}$. The p columns are the filters each of length N.

$$\widehat{\mathbf{P}_\mathbf{p}} = \begin{pmatrix} h_{1,1}^\dagger & h_{2,1}^\dagger & \cdots & h_{p,1}^\dagger \\ h_{1,2}^\dagger & h_{2,2}^\dagger & \cdots & h_{p,2}^\dagger \\ \vdots & \vdots & \ddots & \vdots \\ h_{1,N}^\dagger & h_{2,N}^\dagger & \cdots & h_{p,N}^\dagger \end{pmatrix} \tag{6.37}$$

Now assuming that $\mathbf{h_i}$ is the template that we wish to check for consistency with signal this gives

$$\chi^2 = |\widehat{\mathbf{P}}_p \mathbf{s} - A\widehat{\mathbf{P}}_p \mathbf{h}|^2 \tag{6.38}$$

$$= \sum_{j=1}^{p} |\mathbf{h_j^\dagger s} - (\mathbf{h_i}^\dagger \mathbf{h_j}) \mathbf{h_i^\dagger s}|^2 \tag{6.39}$$

$$= \sum_{j=1}^{p} |\rho_j - (\mathbf{h_i}^\dagger \mathbf{h_j}) \rho_i|^2 \tag{6.40}$$

Since the SNRs for the entire bank are computed already as part of the search this test only requires computing the matrix of inner products $\mathbf{h_i}^\dagger \mathbf{h_j}$.

As it stands this test is not quite χ^2 distributed for Gaussian noise since each element does not have an expectation value equal to one. For one term

$$\langle \chi_j^2 \rangle_{\text{noise}} = \langle |\mathbf{h_j^\dagger n} - (\mathbf{h_i}^\dagger \mathbf{h_j}) \mathbf{h_i^\dagger n}|^2 \rangle \tag{6.41}$$

$$\leq 1 - |\mathbf{h_i}^\dagger \mathbf{h_j}|^2 \tag{6.42}$$

We can use a normalization so that each term has an expectation value equal to one

$$\chi_B^2 = \sum_{j=1}^{p} \frac{|\rho_j - (\mathbf{h_i}^\dagger \mathbf{h_j}) \rho_i|^2}{1 - |\mathbf{h_i}^\dagger \mathbf{h_j}|^2} \tag{6.43}$$

Assuming templates with a mismatch given by (6.27) the expectation for χ_B^2 is

$$\langle \chi_B^2 \rangle_{\text{signal}} \leq p \rho^2 \left[\frac{1}{1-\delta} - 1 \right]^2 \tag{6.44}$$

$$= p A^2 \delta^2 = p \rho^2 \delta^2 \tag{6.45}$$

where the last line holds in the limit that δ is small.

The only additional computational cost required for this test is computing the symmetric matrix of $(\mathbf{h_i}^\dagger \mathbf{h_j})$. Since this test can be done over a sub bank of filters instead of the entire filter bank ([10-100] vs. 1000+) it is not computationally expensive. Assuming that the number of filters $\mathcal{N}$ are broken into p sub banks then the number of operations is $\mathcal{N} N (p +$

1)/2. Comparing this to the computational cost of filtering alone which is $5\mathcal{N} N \log_2[N]$ one finds that as long as $(p+1)/2 < 5\log_2[N]$ the filtering will dominate. Consider a sub-bank where $p = 31$ filtering 256s of data sampled at 4096Hz. The computational cost ratio between computing χ_B^2 and filtering is $(31 + 1)/2/(5\log_2[256 * 4096] = 0.16$. In other words computing the χ_B^2 test contributes about 16% to the overall computational cost in that example.

6.3.3 LIGO Traditional χ^2 Test

The last χ^2 test that I will discuss I'll refer to as the traditional χ^2 test. It is the one described in chapter 2 and has been used exclusively thus far with great success in inspiral searches (56). Recall

$$\chi^2 = |\widehat{\mathbf{P}}_p \mathbf{s} - A\widehat{\mathbf{P}}_p \mathbf{h}|^2 \tag{6.46}$$

The traditional χ^2 test, like the bank veto χ^2 test uses the matched filter waveforms to construct a projection operator. However instead of using many different filter waveforms, the traditional χ^2 test instead uses a decomposition of one filter $\mathbf{h}$ into orthogonal projections $\mathbf{\mathfrak{h}}_i$ satisfying,

$$\mathbf{\mathfrak{h}}_i{}^\dagger \mathbf{\mathfrak{h}}_j = \frac{1}{p}\delta_{ij} \tag{6.47}$$

$$\mathbf{h} = \sum_{i=1}^{p} \mathbf{\mathfrak{h}}_i \tag{6.48}$$

$$\tag{6.49}$$

The projection operator $\widehat{P_p}$ is defined by the components of the $\mathbf{\mathfrak{h}}_i$

$$\widehat{\mathbf{P_p}} = \begin{pmatrix} \mathfrak{h}_{1,1}^\dagger & \mathfrak{h}_{2,1}^\dagger & \mathfrak{h}_{3,1}^\dagger & \cdots \\ \mathfrak{h}_{1,2}^\dagger & \mathfrak{h}_{2,2}^\dagger & \mathfrak{h}_{3,2}^\dagger & \cdots \\ \mathfrak{h}_{1,3}^\dagger & \mathfrak{h}_{2,3}^\dagger & \mathfrak{h}_{3,3}^\dagger & \cdots \\ \mathfrak{h}_{1,4}^\dagger & \mathfrak{h}_{2,4}^\dagger & \mathfrak{h}_{3,4}^\dagger & \cdots \\ \vdots & \vdots & \vdots & \ddots \end{pmatrix} \tag{6.50}$$

Now evaluating (6.30) gives

$$\chi^2 = \sum_{i=1}^{p} |\mathbf{\mathfrak{h}}_i{}^\dagger \mathbf{s} - \rho/p|^2 \tag{6.51}$$

$$= \sum_{i=1}^{p} |\rho_{\mathfrak{h}_i} - \rho/p|^2 \tag{6.52}$$

The expectation values are given in (56) For a signal the expectation is the lesser of

$$\langle \chi_T^2 \rangle = 2\delta\rho^2 \tag{6.53}$$

$$\langle \chi_T^2 \rangle = 2\delta^2 p\rho^2 \tag{6.54}$$

The cost of the traditional chisq test is expensive. Each filter must be broken into p sub filters and Fourier transformed. This makes the computational cost $5\,p\,\mathcal{N}\,N\,\log_2[N]$ which is a factor of p times higher than the filtering cost alone. For $p = 16$ this is a 1,600% increase in computational time [1]

6.3.4 Summary

In this section we have discussed three separate χ^2 tests of the form

$$\chi^2 \;\; = \;\; |\widehat{\mathbf{P}}_p\mathbf{s} - A\widehat{\mathbf{P}}_p\mathbf{h}|^2 \tag{6.55}$$

Each test has a unique projection operator $\widehat{\mathbf{P}}$ that probes a different subspace of the detector data. These tests vary dramatically in their computational time.

Conventional χ^2 test (χ^2_C): The conventional χ^2 test is given by the following

$$\chi^2_C = \widehat{\mathbf{I}}_\mathbf{p}\mathbf{s}^\dagger\mathbf{s} - \rho^\mathbf{2} \tag{6.56}$$

For searches with many templates the computational cost of this technique vanishes. Recall that for ~ 1000 filters the cost is $\ll 1\%$ of the filtering.

Bank χ^2 test (χ^2_B): The χ^2_B test is given by the following,

$$\chi^2_B \;\; = \;\; \sum_{j=1}^{p}\frac{|\rho_j - (\mathbf{h_i}^{\,\dagger}\,\mathbf{h_j})\,\rho_i|^2}{1 - |\mathbf{h_i}^{\,\dagger}\,\mathbf{h_j}|^2} \tag{6.57}$$

For a small number of sub banks p the computational cost of this test is only a fraction of the total cost of filtering the data, however it is roughly 2 orders of magnitude more costly than χ^2_C under typical situations.

Traditional χ^2 test (χ^2_T): The χ^2_T test is given by

$$\chi^2_T \;\; = \;\; \sum_{i=1}^{p}|\rho_{\mathfrak{h}_i} - \rho/p|^2 \tag{6.58}$$

It is the most computationally expensive taking a factor of p times longer to compute than the filtering itself. Under typical situations this is 100 times longer than χ^2_B and 10,000 times longer than χ^2_C.

6.4 Results in Simulated Data

This section will present the results of applying the three tests χ^2_C, χ^2_B and χ^2_T to simulated data of the form of (6.6). A filter bank of sixteen templates was made from

$$h(t) \propto (8 - t)^{-1/4} \sin\left[\alpha\,(8 - t)^{5/8} - 1\right] \tag{6.59}$$

---

[1]This high cost is not seen in current LIGO coincidence searches. By only applying the χ^2_T test to triggers already found in coincidence the cost is reduced to roughly 10% of the total data analysis pipeline cost. However, it is the intention of this chapter to compare these tests at the single detector level.

Table 6.1: Comparison of computational cost relative to filtering for the three χ^2 tests. $\mathcal{N} = 625$, N = 1048576 in these examples (256s of data sampled at 4096Hz with 625 filters.)

Action	Computations	% of filter time
Filtering	$5\,\mathcal{N}\,N\,\log_2[N]$	100%
χ_C^2	$5\,N\,\log_2[N] + \mathcal{O}(N)$	0.16%
χ_B^2	$\mathcal{N}\,N\,(p+1)/2$	16.0% (p=31)
χ_T^2	$5\,\mathcal{N}\,N\,(p/2)\,\log_2[N]$	1600% (p=32)

where $\alpha \in [5.0250, 5.3250]$. These waveforms mimic the quadrupole approximation to inspiral waveforms. The glitches were made by

$$x(t) = e^{[-b(\tau_x/2-t)^2]} \sin[2\pi f t + R_n(t)] \tag{6.60}$$

Where R_n is a normally distributed random variable, $\tau_x \in [0.01, 8]$, $f \in [100, 300]$ and $b \in [1, 11]$.

Both glitches and simulated signals were injected into 32 second blocks of white noise at amplitudes that resulted in a logarithmically uniform distribution of SNR from approximately $\{1, 200\}$. Injections of glitches and real signals were performed to sample the probability distribution of χ^2 and SNR. The injected signals were mismatched from the filter bank by an average of a few percent. That means that the expected χ^2 value for signals is a function of SNR as described in the previous section. It is possible to parametrize the expectation for mismatched signals for all the χ^2 tests as

$$\xi = \frac{\chi^2}{p + \epsilon\,\mathrm{SNR}^2} \tag{6.61}$$

I found that for χ_C^2 and χ_B^2 $\epsilon = 0.06$ was appropriate making ξ independent of SNR when injecting simulated signals. For χ_T^2 $\epsilon = 0.001$ worked.

I evaluate the probability of obtaining a ξ value above some threshold ξ^*. Let the number density of triggers (simulated signals and glitches) as a function of SNR and ξ be

$$\frac{\mathrm{dN}}{\mathrm{d}\rho\,\mathrm{d}\xi} = \mathrm{N}(\rho, \xi) \tag{6.62}$$

The number of triggers found above a given SNR threshold, ρ^* and above a given ξ^* threshold is

$$N_F(\rho > \rho^*, \xi > \xi^*) = \int \mathrm{N}(\rho, \xi^2)\,\Theta[\rho - \rho^*]\,\Theta[\xi^* - \xi^2]\,\mathrm{d}\rho\,\mathrm{d}\xi \tag{6.63}$$

Furthermore the number of triggers above ρ^* for all ξ values is

$$N_T(\rho > \rho^*) = \int \mathrm{N}(\rho, \xi)\,\Theta[\rho - \rho^*]\,\mathrm{d}\rho\,\mathrm{d}\xi \tag{6.64}$$

The probability that a trigger is above a given ξ^* threshold and above a given SNR threshold is defined as

$$\mathrm{P}(\rho > \rho^*, \xi > \xi^*) = N_F(\rho^*, \xi*)\ /\ N_T(\rho^*) \tag{6.65}$$

and is always between [0,1].

Figure 6.4 shows the distribution of ξ for injections. The distributions are roughly SNR independent by construction. The ξ_T and ξ_B have similar degrees of freedom and thus similar widths. The number of degrees of freedom was chosen to be consisten with previous LIGO searches (16). However ξ_C has far more degrees of freedom. The resulting distribution is nearly Gaussian. Choosing a threshold in ξ should result in a small number of injections being rejected (0-5%). As discussed in chapter 2 the detection efficiency is directly effected by such cuts. Once a threshold is chosen at the desired efficiency it can be compared to figure 6.5. It is then possible to evaluate the probability that an false trigger (glitch) has a ξ value above the threshold. In every case high SNR triggers are completely rejected. ξ_T gives the best separation at large SNR however. Recall that the computational cost of ξ_T is orders of magnitude larger than the other tests. The next section will investigate these tests on real LIGO data and evaluate the efficacy of a combined approach using ξ_B and ξ_C versus the more expensive ξ_T.

6.5 Results in Real Data

This section looks at applying these tests to the data set and pipeline described in chapter 2. The codes were added to the LSC Algorithm Library (LAL) (131) and applied to a portion of single detector, L1, data. The pipeline was carried only through the first matched filtering stage (however the χ^2 test was enabled.) This is not meant to be a different search on this data. As stated before no plausible gravitational-wave candidates were found.

The template bank used spanned a component mass range of $\{1.2\text{-}1.6\}$ $M_\odot$ and required $\sim$ 450 templates to cover the region while allowing no more than 3% loss in SNR. Approximately 3000 injections were successfully recovered by the pipeline and 60,000 false triggers above a SNR of 6 were found. The injections were made uniformly across the sky and logarithmically in distance. Also included in this data set were 18 hardware injections (see chapter 2) of 1.4 $M_\odot$ binaries up to a SNR of about 50. The goal of this test is to evaluate the performance of the χ^2_B and χ^2_C tests compared to the more expensive χ^2_T test. We found that in order to remove the SNR dependence of the B, C, T tests we required $\epsilon = 0.15, 1, 0.1$ respectively. The scatter plots of triggers in the SNR and χ^2,ξ plane are shown in figures 6.6, 6.7 and 6.8.

In order to compare the use of ξ_C and ξ_B together with the use of ξ_T we first chose triggers that had ξ_B, $\xi_C \leq 2.3, 1.3$ respectively. Then we choose triggers that had $\xi_T \leq 1.3$. Neither set rejected any hardware injections. Both sets kept 97% of software injections. The result for the false triggers is shown in figure 6.9. Both situations result in similar rejection of high SNR transients making the computationally cheaper χ^2_C and χ^2_B tests a viable signal based veto choice.

6.6 Conclusion

I have presented two new χ^2 tests for LIGO data analysis and compared the effectiveness and computational cost to the traditional test currently used (56). The traditional test uses approximately 10^4 times the computing time than the conventional χ^2_C test. The second test, which uses the correlations between filters in the bank, lies in the middle computationally, requiring 10^2 times the computation of the conventional χ^2 test but still negligible compared to the matched filtering costs. The tests show that combining the χ^2_C and χ^2_B tests gives comparable performance to the χ^2_T test in real data.
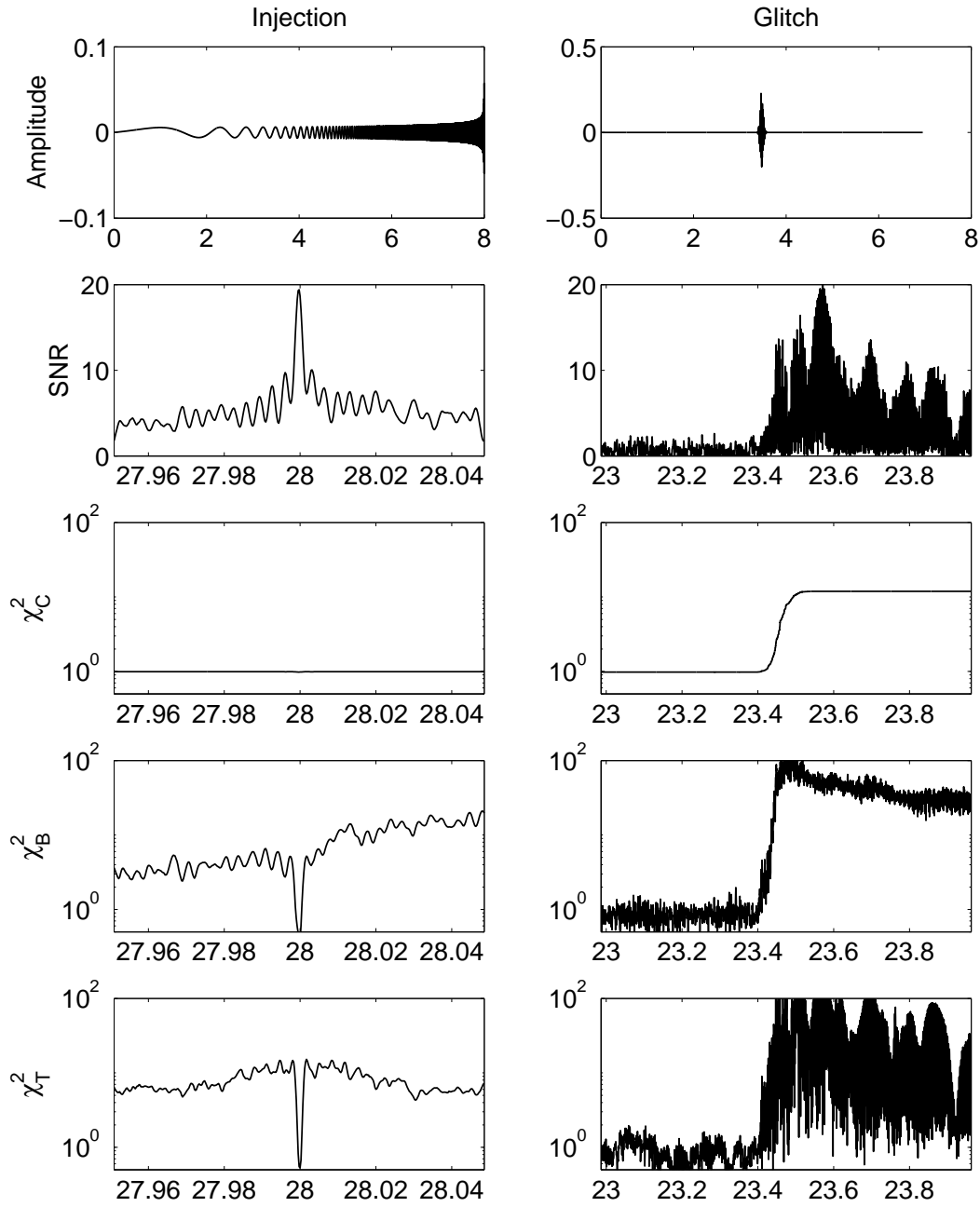
Figure 6.3: SNR and χ^2 time series for injections and glitches.
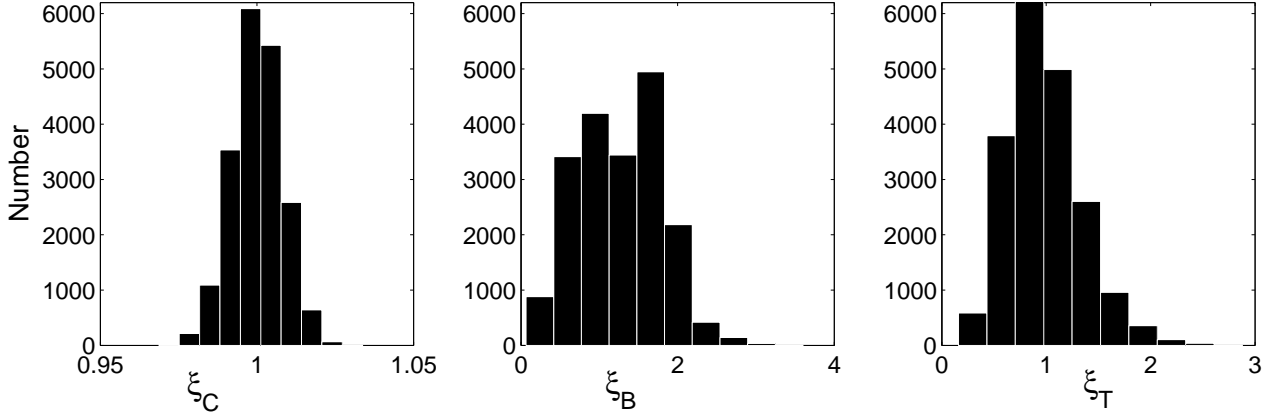
Figure 6.4: Gaussian noise distributions for ξ_C, ξ_B and ξ_T. The ξ_C has $\sim 10^5$ degrees of freedom and thus the distribution tends toward normality with the standard deviation given approximately by $\sqrt{2/p}$.
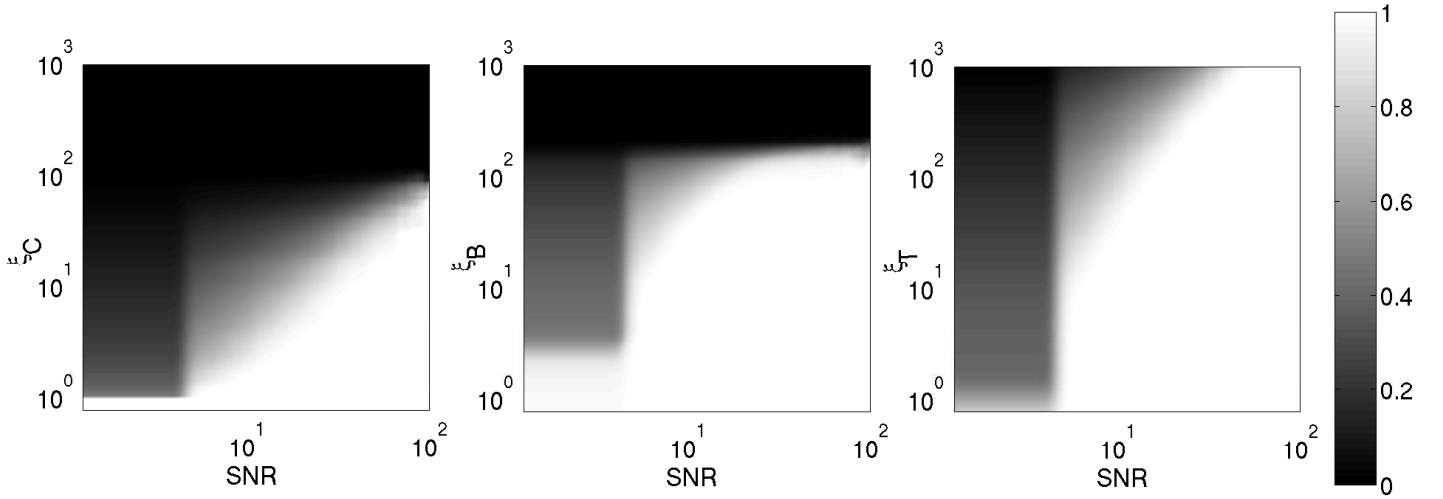
Figure 6.5: Probability of obtaining a false trigger above a given ξ and SNR. This can be interpreted as a rejection fraction for a given SNR and ξ threshold. Choosing a ξ threshold of 5 would reject all triggers above SNR 15 in all three cases, for example.
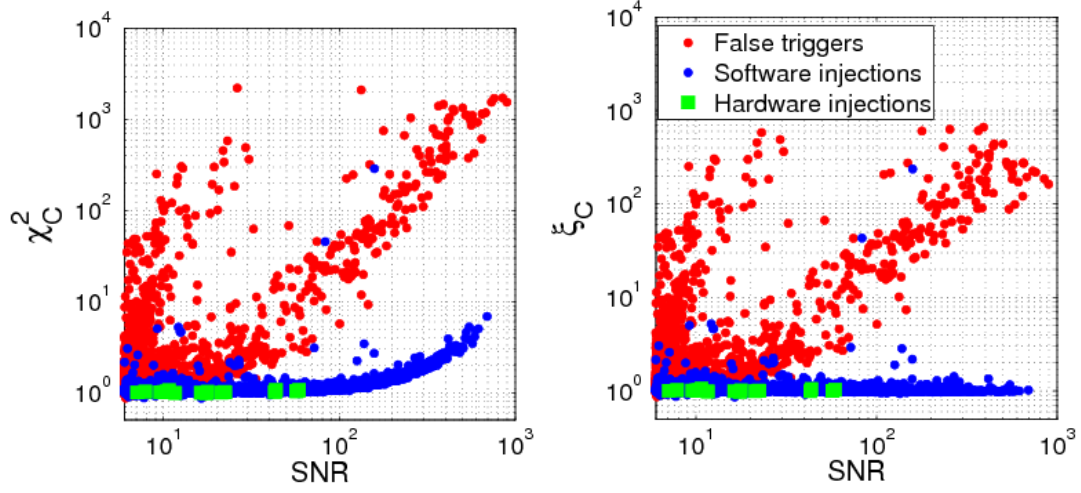
Figure 6.6: Left: SNR χ^2_C scatter plot of L1 triggers. Right: SNR, ξ_C scatter plot of L1 triggers.
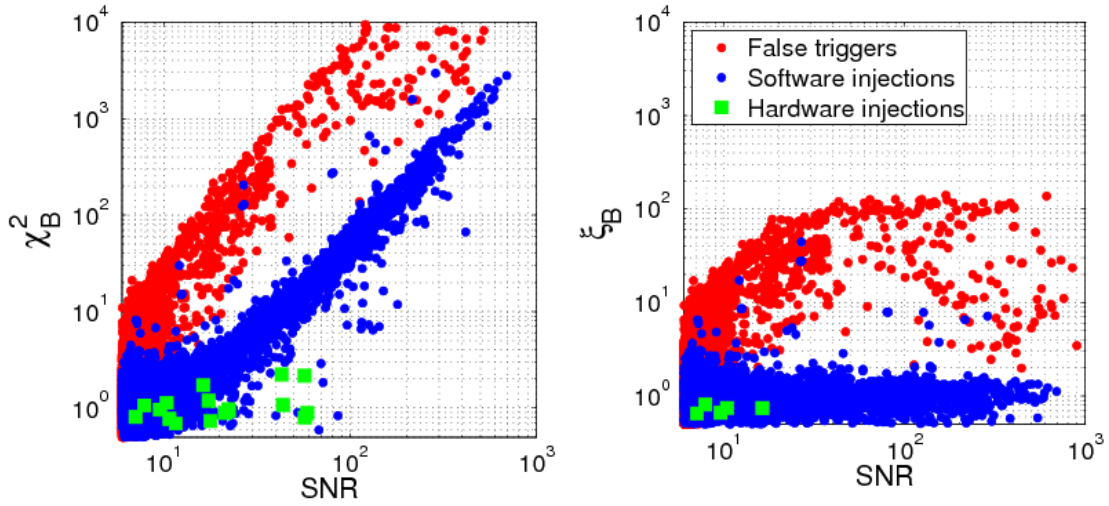
Figure 6.7: Left: SNR χ^2_B scatter plot of L1 triggers. Right: SNR, ξ_B scatter plot of L1 triggers.
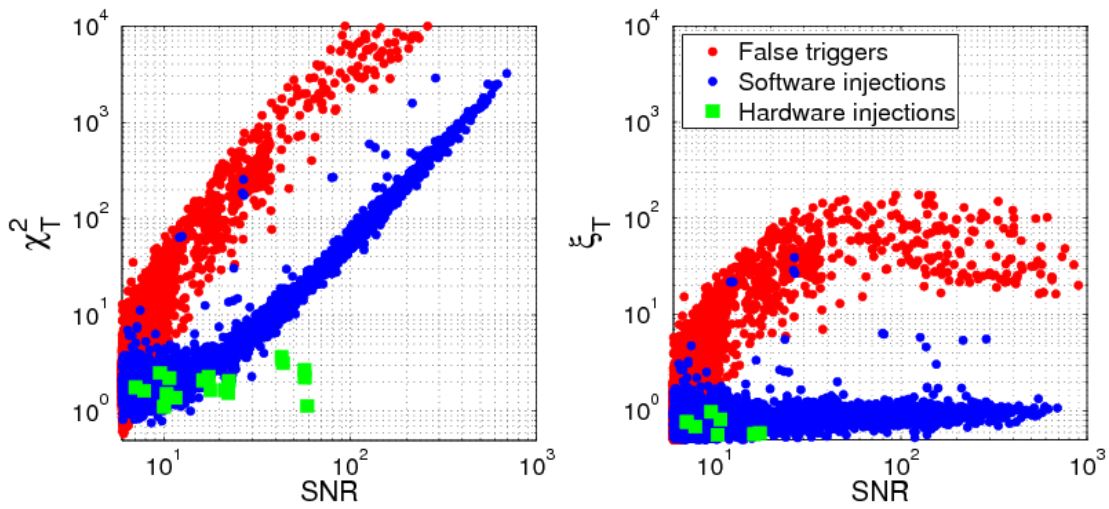
Figure 6.8: Left: SNR χ_T^2 scatter plot of L1 triggers. Right: SNR ξ_T scatter plot of L1 triggers.
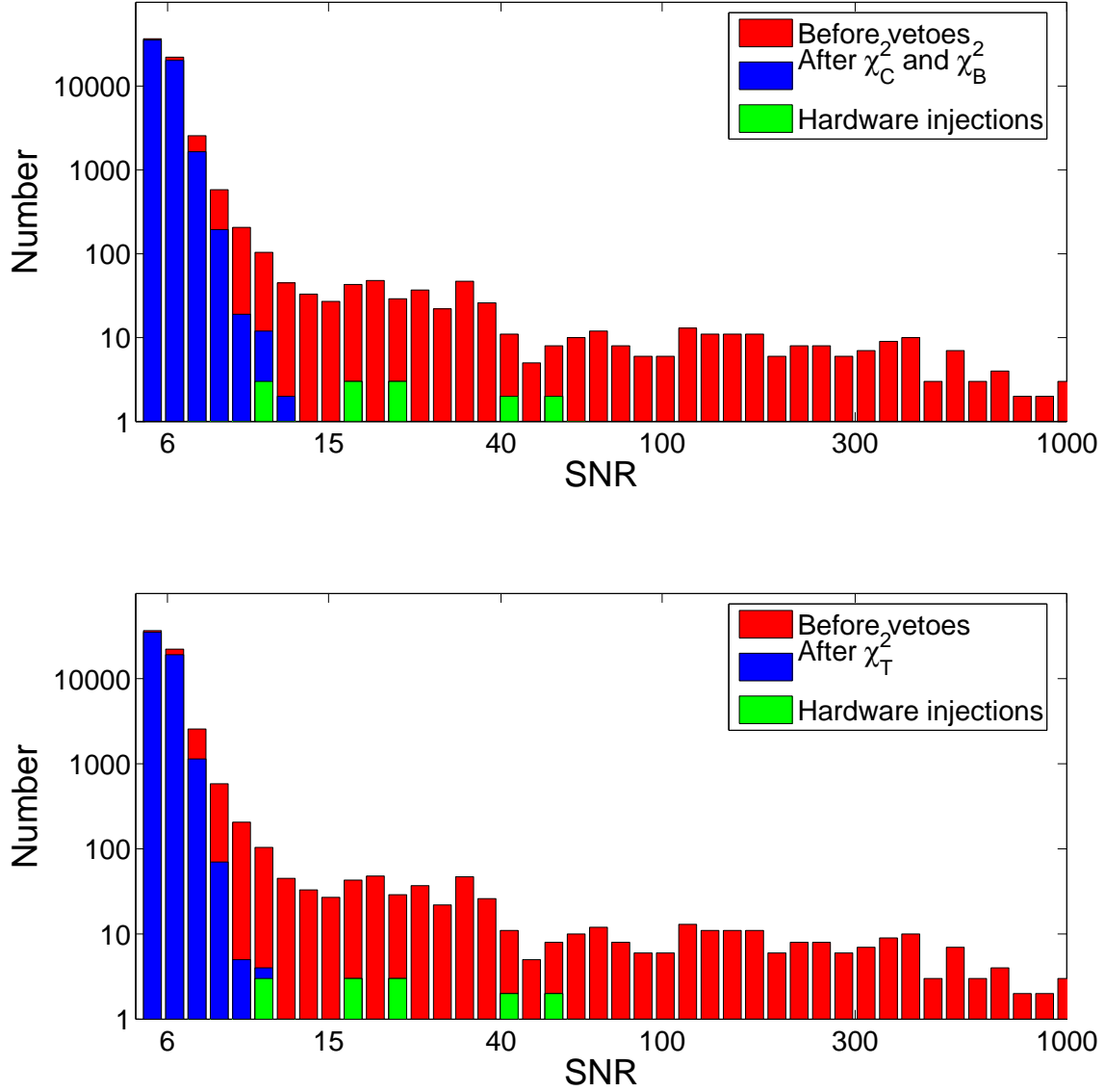
Figure 6.9: Comparison of χ^2_C and χ^2_B tests to the χ^2_T test in real data. The red histograms represent the distributions of triggers before vetoes. The blue histograms result from applying vetoes with a 3% loss in simulated signals. All hardware injections were recovered (green) and would be more detectable amidst the background of false triggers after vetoes are applied.

7. Conclusions

The detection of gravitational waves requires an extremely sensitive instrument capable of detecting strains of $\sim 10^{-21}$. The LIGO interferometers have reached that sensitivity across a broad frequency range. The range is suitable for detecting gravitational radiation from the late inspiral of compact binary systems up to about 100 solar masses. The waveforms for such systems are well known making matched filtering a powerful search technique.

This thesis has described an example of a search for sub solar mass compact objects in LIGO data. Key concepts regarding templates, filtering and rate upper limits were introduced early on in chapter 2. A more detailed look into how the rate upper limits depend on the nearby galaxy population was described in chapter 3. Chapter 4 touched on how numerical relativity is giving us information about the very late inspiral stages, the so called "merger" phases, and a way to use the information in LIGO data analysis. Chapter 5 discussed one example of a way to veto false triggers by examining auxiliary channels recorded by LIGO. Chapter 6 described in depth two new signal based vetoes that are computationally inexpensive and very powerful at rejecting false triggers. These tests may lead to an increased confidence in detection and improve overall search sensitivity.

Continued work on all the before mentioned concepts is bringing us closer to one day (regularly) observing gravitational radiation from compact binary systems. As our knowledge of signals and search techniques improves we will make more sensitive searches. This thesis discusses work analyzing data from the initial LIGO design. Already we have begun work commissioning enhanced and advanced detectors. Within a decade advanced LIGO will increase LIGO's range by more than a factor of 10. This allows us to probe 1000 times LIGO's currently probed portion of our Universe making the coming decade an exciting time for astrophysics, astronomy and gravitation. We expect to observe compact binary coalescence at 1000 times the rate we currently can. We will be able to verify the results of numerical relativity through the direct observation of gravitational-waves from binary black holes, and we may be able to answer questions about the origins of gamma ray bursts through combined LIGO / electromagnetic observations. There is no doubt that the resulting discoveries will be a new view of some of nature's most violent interactions. With a bit of serendipity they will be something totally unexpected.

Bibliography

[1] "A first course in general relativity" Bernard F. Schutz, Cambridge University Press (1985)

[2] "Gravitational-Wave-Detector Events" J. Weber, Phys. Rev. Lett. 20, 1307 - 1308 (1968)

[3] "Evidence for Discovery of Gravitational Radiation" J. Weber, Phys. Rev. Lett. 22, 1320 - 1324 (1969)

[4] "Anisotropy and Polarization in the Gravitational-Radiation Experiments" J. Weber, Phys. Rev. Lett. 25, 180 - 184 (1970)

[5] "A Fleeting Detection of Gravitational Waves" David Lindley, `http://focus.aps.org/story/v16/st19`

[6] `http://www.ligo.caltech.edu/`

[7] `http://geo600.aei.mpg.de/`

[8] `http://tamago.mtk.nao.ac.jp`

[9] `http://www.virgo.infn.it/`

[10] "A new test of general relativity : gravitational radiation and the binary pulsar PSR 1913 +16" Taylor, J. H. and Weisberg, J. M., Astrophysical Journal 253 (1982)

[11] "300 years of gravitation" Hawking, Israel ed., Cambridge University Press (1987)

[12] "Upper limits on gravitational wave emission from 78 radio pulsars" The LIGO Scientific Collaboration, Phys. Rev. D 76, 042001 (2007)

[13] "All-sky search for periodic gravitational waves in LIGO S4 data" The LIGO Scientific Collaboration, Phys. Rev. D 77, 022001 (2008)

[14] "Search for gravitational-wave bursts in LIGO data from the fourth science run" The LIGO Scientific Collaboration, Class. Quantum Grav. 24 5343 (2007)

[15] "Searching for a Stochastic Background of Gravitational Waves with the Laser Interferometer Gravitational-Wave Observatory" The LIGO Scientific Collaboration, ApJ, 659:918930, (2007)

[16] "Search for gravitational waves from binary inspirals in S3 and S4 LIGO data." The LIGO Scientific Collaboration, `http://arxiv.org/abs/0704.3368` (2007)

[17] "Fundamentals of interferometric gravitational wave detectors" Peter Saulson, World Scientific (1994)

[18] http://www.ligo.org/

[19] http://www.ligo.caltech.edu/docs/M/M980279-05/M980279-05.pdf

[20] "Feedforward reduction of the microseism disturbance in a long-base-line interferometric gravitational-wave detector" J. A. Giaime, E. J. Daw, M. Weitz, R. Adhikari, P. Fritschel, R. Abbott, R. Bork, and J. Heefner, Review of Scientific Instruments 74 1 218-224 (2003)

[21] "Statistical Digital Signal Processing and Modeling" Hayes, Monson H., Wiley (1996).

[22] "Method to estimate ISCO and ring-down frequencies in binary systems and consequences for gravitational wave data analysis" Chad Hanna, Miguel Megevand, Evan Ochsner, and Carlos Palenzuela, In preparation (2008)

[23] "An Analytic Representation for the Quasi-Normal Modes of Kerr Black Holes." E.W. Leaver, Proc. R. Soc. London Ser. A 402 285 (1985)

[24] "Search techniques for gravitational waves from black-hole ringdowns" Jolien D. E. Creighton, Phys.Rev. D60 022001 (1999)

[25] "Further experimental tests of relativistic gravity using the binary pulsar 1913+16" Taylor, J. H. and Weisberg, J. M., Astrophysical Journal 345 (1989)

[26] "Relativistic Binary Pulsar B1913+16: Thirty Years of Observations and Analysis" Weisberg, J. M. and Taylor, J. H. Binary Radio Pulsars, ASP Conference Series, Vol. 328, Proceedings of the conference held 11-17 January, 2004, Aspen, Colorado, USA. Edited by F. A. Rasio and I. H. Stairs. San Francisco: Astronomical Society of the Pacific, 2005

[27] "Neutron Star Mass Measurements. I. Radio Pulsars" S. E. Thorsett and Deepto Chakrabarty, Astrophys.J. 512 288-299 (1999)

[28] "Theoretical Astrophysics Volume II: Stars and Stellar Systems" T. Padmanabhan, Cambridge University Press. (2001)

[29] "Primordial black hole formation during the QCD epoch" Karsten Jedamzik, Phys. Rev. D 55, R5871 - R5875 (1997)

[30] "The MACHO Project: Microlensing Results from 5.7 Years of Large Magellanic Cloud Observations" The MACHO Collaboration, The Astrophysical Journal, 542:281307, (2000)

[31] "Gravitational Waves from Coalescing Black Hole MACHO Binaries" Takashi Nakamura, Misao Sasaki, Takahiro Tanaka and Kip S. Thorne, The Astrophysical Journal, 487:L139L142, (1997)

[32] "Search for gravitational waves from primordial black hole binary coalescences in the galactic halo" The LIGO Scientific Collaboration, Phys. Rev. D 72, 082002 (2005)

[33] "Interpreting the results of searches for gravitational waves from coalescing binaries" Brady, Patrick R. and Fairhurst, Stephen, arXiv:0707.2410 [gr-qc] (2007)

[34] ""Host Galaxies Catalog Used in LIGO Searches for Compact Binary Coalescence Events" Ravi Kumar Kopparapu, Chad Hanna, Vicky Kalogera, Richard O'Shaughnessy, Gabriela Gonzalez, Patrick R. Brady, Stephen Fairhurst, The Astrophysical Journal, 675 1459-1467 (2008)

[35] "Erratum: "The Cosmic Coalescence Rates for Double Neutron Star Binaries (ApJ, 601, L179 [2004])" Kalogera, V. and Kim, C. and Lorimer, D. R. and Burgay, M. and D'Amico, N. and Possenti, A. and Manchester, R. N. and Lyne, A. G. and Joshi, B. C. and McLaughlin, M. A. and Kramer, M. and Sarkissian, J. M. and Camilo, F., Astrophysical Journal Letters, 614 L137-138 (2004)

[36] "Constraining population synthesis models via observations of compact-object binaries and supernovae" O'Shaughnessy,R and Kim,C and Kalogera, V and Belczynski, K. astro-ph/0610076 (2006)

[37] "Upper limits on gravitational-wave signals based on loudest events" "P. R. Brady and J. D. E. Creighton and A. G. Wiseman, Class. Quant. Grav. 21 S1775-S1781 (2004)

[38] "The Loudest Event Statistic: General formulation, properties and applications" Biswas, Rahul; Brady, Patrick R.; Creighton, Jolien D. E. and Fairhurst, Stephen, arXiv:0710.0465 [gr-qc] (2007).

[39] `http://www.ligo.caltech.edu/advLIGO/`

[40] "Tuning matched filter searches for compact binary coalescence" LIGO Scientific Collaboration Technical Document, LIGO-T070109-01 `http://www.ligo.caltech.edu/docs/T/T070109-01.pdf`

[41] "Extraction of signals from noise" L A Wainstein and V D Zubakov, Prentice-Hall Englewood Cliffs, NJ (1962).

[42] "The Last three minutes: issues in gravitational wave measurements of coalescing compact binaries" Cutler, Curt et al., Phys. Rev. Lett." 70 2984-2987 (1993)

[43] "LIGO Calibration Accuracy" Bruce Allen. `http://www.ligo.caltech.edu/docs/T/T960189-00.pdf` (1996)

[44] "Calibration of the LIGO Detectors for the First LIGO Scientific Run" R. Adhikari and P. Fritschel and G. González and M. Landry and L. Matone and H. Radkins and A. Takamori and B. O'Reilly, `http://www.ligo.caltech.edu/docs/T/T030097-00.pdf` (2003)

[45] "Calibration of the LIGO detectors for S2" G. González and M. Landry and B. O'Reilly, `http://www.ligo.caltech.edu/docs/T/T040060-00.pdf` (2004)

[46] "Calibration of the LIGO detectors for S2" Alexander Dietz, Justin Garofoli, Gabriela González, Mike Landry, Brian O'Reilly and Myungkee Sung, `http://www.ligo.caltech.edu/docs/T/T050262-01.pdf` (2006)

[47] "FINDCHIRP: an algorithm for detection of gravitational waves from inspiraling compact binaries" Allen, B.; Anderson, W. G.; Brady, P. R.; Brown, D. A.; Creighton, J. D. E., http://arxiv.org/abs/gr-qc/0509116 (2005).

[48] "Search for gravitational waves from galactic and extra-galactic binary neutron stars." The LIGO Scientific Collaboration, Phys. Rev. D 72, 082001 (2005).

[49] Sathyaprakash, B S and Dhurandhar, S V, Phys. Rev D. 44 3819 (1991)

[50] "Gravitational waves from inspiraling compact binaries: Second post-Newtonian wave forms as search templates" Droz, Serge and Poisson, Eric., Phys. Rev. D 56 4449 (1997)

[51] "Statistical Theory of Signal Detection, 2nd edition" C. W. Helmstrom, Pergamon Press, London (1968)

[52] "Beam Pattern Response Functions and Times of Arrival for Earthbound Interferometers" Warren G. Anderson and John T. Whelan and Patrick R. Brady and Jolien D. E. Creighton and David Chin and Keith Riles, LIGO-T010110-00-Z `http://www.lsc-group.phys.uwm.edu/daswg/docs/technical/T010110.pdf`

[53] "Chi Distribution." Weisstein, Eric W, From MathWorld–A Wolfram Web Resource. `http://mathworld.wolfram.com/ChiDistribution.html`

[54] "Data Reduction and Error Analysis for the Physical Sciences" Philip Bevington and D. Keith Robinson, McGraw Hill (2003)

[55] "Testing the LIGO inspiral analysis with hardware injections" Duncan Brown (for the LIGO Scientific Collaboration), Class. Quant. Grav. 21 S797-S800" (2004)

[56] "A χ^2 time-frequency discriminator for gravitational wave detection" Bruce Allen, Phys. Rev. D 71 062001 (2005)

[57] "Reducing False Alarms in Searches For Gravitational Waves From Coalescing Binary Systems" Andres Rodriguez, M.S. Thesis, Lousiana State University (2007)

[58] "The rate of neutron star binary mergers in the universe - Minimal predictions for gravity wave detectors" Phinney, E. S., ApJ, 380, L17 (1991)

[59] "The gravitational wave sky" Lipunov, V. M., Nazin, S. N., Panchenko, I. E., Postnov, K. A., & Prokhorov, M. E., A&A, 298, 677 (1995)

[60] "Expected coalescence rates of NS-NS binaries for laser beam interferometers" de Freitas Pacheco, J. A., Regimbau, T., Vincent, S., & Spallicci, A., Int. J. Mod. Phys. D, 15, 235 (2006)

[61] "The Millennium Galaxy Catalogue: The luminosity functions of bulges and discs and their implied stellar mass densities" Driver, P, S., & Allen, D, P., ApJ Letters, 657, L85 (2007)

[62] "Black Hole Mergers in the Universe" Portegeis Zwart, S. F. and McMillan, S. L. W., ApJ, L17 (2000)

[63] "Dynamical Interactions and the Black Hole Merger Rate of the Universe" O'Leary, R., O'Shaughnessy, R., and Rasio, F. A., Phys. Rev. D 76, 061504(R) (2007)

[64] "Final Results from the Hubble Space Telescope Key Project to Measure the Hubble Constant" Freedman, W., et al., ApJ, 553, 47 (2001)

[65] "Dwarf Galaxies of the Local Group" Mateo, M., ARA&A, 36, 435 (1998)

[66] "HYPERLEDA. I. Catalog of galaxies" Paturel, G., Petit, C., Prugniel, Ph., Theureau, G., Rousseau, J., Brouty, M., Dubois, P., Cambrésy, L., A&A, 412, 45. http://leda.univ-lyon1.fr/intro.html (2003)

[67] Tully, B., Private communication (2006)

[68] "Action Principle Solutions for Galaxy Motions within 3000 Kilometers per Second" Shaya, E., Peebles, P. J., & Tully, B., ApJ 454, 15 (1995)

[69] "Three-Year Wilkinson Microwave Anisotropy Probe (WMAP) Observations: Implications for Cosmology" Spergel, D. N., et al. ApJS, 170, 377 (2007)

[70] "Galactic Dynamics" Binney, J., & Tremaine, S, (Princeton Series in Astrophysics; Princeton; Princeton University Press) (2000)

[71] "An analytic expression for the luminosity function for galaxies" Schechter, P., ApJ, 203, 297 (1976)

[72] "The Galaxy Luminosity Function and Luminosity Density at Redshift z = 0.1" Blanton, M. R., et al. ApJ, 592, 819 (2003)

[73] "K-Corrections and Filter Transformations in the Ultraviolet, Optical, and Near-Infrared" Blanton, M. R., & Roweis, S. AJ, 133, 734 (2007)

[74] "The Coalescence Rate of Double Neutron Star Systems" Kalogera, V., Narayan, R., Spergel, D. N., & Taylor, J. H., ApJ, 556, 340 (2001)

[75] "The 60-micron and far-infrared luminosity functions of IRAS galaxies" Saunders, W., Rowan-Robinson, M., Lawrence, A., Efstathiou, G., Kaiser, N., Ellis, R. S., & Frenk, C. S., MNRAS, 242, 318 (1990)

[76] "Gravitational Waves from Extragalactic Inspiraling Binaries: Selection Effects and Expected Detection Rates" Nutzman, P., Kalogera, V., Finn, L. S., Hendrickson, C., & Belczynski, K., ApJ, 612, 364 (2004)

[77] "The Probability Distribution Of Binary Pulsar Coalescence Rates. II. Neutron Star-White Dwarf Binaries" Kim, C., Kalogera, V., Lorimer, D. R., & White, T., ApJ, 616, 1109 (2004)

[78] "Effect of PSR J0737-3039 on the DNS Merger Rate and Implications for GW Detection" Kim, C., Kalogera, V., & Lorimer, D. R., astro-ph/0608280 (2006)

[79] "A Comprehensive Study of Binary Compact Objects as Gravitational Wave Sources: Evolutionary Channels, Rates, and Physical Properties" Belczynski, K., Kalogera, V., & Bulik, T., ApJ, 572, 407 (2002)

[80] "Black Hole Spin Evolution: Implications for Short-hard Gamma Ray Bursts and Gravitational Wave Detection" Belczynski, K., Taam, R. E., Rantsiou, E., & van der Sluys, M. V., astro-ph/0703131 (2007)

[81] "Excess power statistic for detection of burst sources of gravitational radiation" Anderson, W. G., Brady, P. R., Creighton, J.D., & Flanagan, É. É., Phys. Rev. D, 63, 042003 (2001)

[82] "The last three minutes: Issues in gravitational-wave measurements of coalescing compact binaries." C. Cutler et al., Phys. Rev. Lett. 70, 2984 (1993).

[83] "Search templates for gravitational waves from inspiraling binaries: Choice of template spacing." B. J. Owen., Phys. Rev. D 53, 6749 (1996).

[84] "Analysis of LIGO data for gravitational waves from binary neutron stars." The LIGO Scientific Collaboration, Phys. Rev. D 69, 122001 (2004).

[85] "Search for gravitational waves from binary black hole inspirals in LIGO data." The LIGO Scientific Collaboration, Phys. Rev. D 73, 062001 (2006).

[86] "Inspiral, merger and ring-down of equal-mass black-hole binaries." Alessandra Buonanno, Gregory B. Cook, Frans Pretorius, http://lanl.arxiv.org/abs/gr-qc/0610122 (2006).

[87] "Inspiral, merger and ring-down of unequal mass black hole binaries: a multipolar analysis." Emanuele Berti, Vitor Cardoso, Jose A. Gonzalez, Ulrich Sperhake, Mark Hannam, Sascha Husa, Bernd Bruegmann, http://arxiv.org/abs/gr-qc/0703053 (2007).

[88] "Matched filtering of numerical relativity templates of spinning binary black holes." Birjoo Vaishnav, Ian Hinder, Frank Herrmann, and Deirdre Shoemaker, Phys. Rev. D 76, 084020 (2007).

[89] "Binary black hole late inspiral: Simulations for gravitational wave observations." J. G. Baker, S.T. McWilliams, J. R. van Meter, J. Centrella, D. Choi, B. J. Kelly, and M. Koppitz., Phys. Rev. D 75, 124024 (2007).

[90] "A data-analysis driven comparison of analytic and numerical coalescing binary waveforms: non-spinning case." Yi Pan et al, arXiv:0704.1964v2 [gr-qc] (2007).

[91] "Gravitational-wave data analysis using binary black-hole waveforms." P. Ajith, arXiv:0712.0343v1 [gr-qc]

[92] "Estimating the final spin of a binary black hole coalescence." Alessandra Buonanno, Lawrence E. Kidder, Luis Lehner, http://arxiv.org/abs/0709.3839 (2007).

[93] "Effective one-body approach to general relativistic two-body dynamics." A. Buonanno and T Damour, Phys. Rev. D 59, 084006 (1999)

[94] "Toward faithful templates for non-spinning binary black holes using the effective-one-body approach." Buonanno, Alessandra; Pan, Yi; Baker, John G.; Centrella, Joan; Kelly, Bernard J.; McWilliams, Sean T.; van Meter, James R., `http://arxiv.org/abs/0706.3732` (2007)

[95] "Innermost stable orbits for coalescing binary systems of compact objects" L E Kidder, C M Will and A G Wiseman., Class. Quantum Grav. 9 L125-L131 (1992)

[96] "Innermost circular orbit of binary black holes at the third post-Newtonian approximation" Luc Blanchet, Phys.Rev. D65 (2002).

[97] "Gravitational Radiation from Post-Newtonian Sources and Inspiralling Compact Binaries." Luc Blanchet, Living Rev. Relativity 9, 4. URL (cited on 2007-12-20): `http://www.livingreviews.org/lrr-2006-4` (2006)

[98] "Rotating Black Holes: Locally Nonrotating Frames, Energy Extraction, and Scalar Synchrotron Radiation." Bardeen, J. M., Press, W. H., and Teukolsky, S. A., ApJ, **178** 347 (1972).

[99] "On the final spin from the coalescence of two black holes" Luciano Rezzolla, Enrico Barausse, Ernst Nils Dorband, Denis Pollney, Christian Reisswig, Jennifer Seiler, Sascha Husa., `http://xxx.arxiv.org/abs/0712.3541`

[100] "The final spin from the coalescence of aligned-spin black-hole binaries." L. Rezzolla, P. Diener, E. N. Dorband, D. Pollney, C. Reisswig, E. Schnetter, J. Seiler., ApJ, 674: L29L32 (2007)

[101] "Eccentric binary black-hole mergers: The transition from inspiral to plunge in general relativity." U. Sperhake, E. Berti, V. Cardoso, J. A. Gonzalez, B. Bruegmann, M. Ansorg, `http://arxiv.org/abs/0710.3823` (2007).

[102] Luis Lehner *private communication November 2007.*

[103] "Gravitational-wave measurements of the mass and angular momentum of a black hole" Fernando Echeverria., Phys. Rev. D 40, 3194 - 3203 (1989)

[104] "On gravitational-wave spectroscopy of massive black holes with the space interferometer LISA" Emanuele Berti, Vitor Cardoso, Clifford M. Will Phys.Rev. D73 064030 (2006)

[105] "Learning about compact binary merger: the interplay between numerical relativity and gravitational-wave astronomy" Thomas Baumgarte, Patrick Brady, Jolien D E Creighton, Luis Lehner, Frans Pretorius, Ricky DeVoe., `http://arxiv.org/abs/gr-qc/0612100` (2006)

[106] "Observing binary inspiral in gravitational radiation: One interferometer" Lee Samuel Finn and David Chernoff., Phys. Rev. D 47, 2198 - 2219 (1993)

[107] "Measuring gravitational waves from binary black hole coalescences. I. Signal to noise for inspiral, merger, and ring-down" Éanna É. Flanagan and Scott A. Hughes, Phys. Rev. D 57, 4535 - 4565 (1998)

[108] "Binary black hole merger: symmetry and the spin expansion" Latham Boyle, Michael Kesden, Samaya Nissanke., http://arxiv.org/abs/0709.0299 (2007)

[109] LIGO Science Requirement Document noise curve http://www.ligo.caltech.edu/~jzweizig/distribution/LSC_Data/srd.html.

[110] "Prospects for gravitational-wave observation of neutron-star tidal disruption in neutron-star/black-hole binaries." Vallisneri, M., Phys.Rev.Lett. **84** 3519 (2000)

[111] "Possible direct method to determine the radius of a star from the spectrum of gravitational wave signals II : Spectra for various cases." Motoyuki Saijo, Takashi Nakamura, Phys.Rev. D63 064004 (2001)

[112] "Determining the nuclear equation of state from neutron-star masses and radii." Lindblom, Lee, ApJ, 1 398, p. 569-573 (1992).

[113] "Reconstructing the equation of state for cold nuclear matter from the relationship of any two properties of neutron stars." Tomohiro Harada, Phys.Rev. C64 048801 (2001)

[114] "Merger of black hole and neutron star in general relativity: Tidal disruption, torus mass, and gravitational waves." Masaru Shibata and Keisuke Taniguchi, arXiv:0711.1410v1 [gr-qc]

[115] "Where post-Newtonian and numerical-relativity waveforms meet." Mark Hannam, Sascha Husa, Jose A. Gonzalez, Ulrich Sperhake, Bernd Bruegmann, http://arxiv.org/abs/0706.1305 (2007).

[116] "Consistency of post-Newtonian waveforms with numerical relativity." John G. Baker, James R. van Meter, Sean T. McWilliams, Joan Centrella, Bernard J. Kelly, Phys. Rev. Lett. vol. 99, 181101 (2007).

[117] "High-accuracy comparison of numerical relativity simulations with post-Newtonian expansions." Boyle et al, arXiv:0710.0158v1 [gr-qc].

[118] "Reducing gravitational wave false alarms using signals at the antisymmetric port in LIGO detectors" C. R. Hanna for the LIGO Scientific Collaboration, Class. Quantum Grav. 23 S17 (2006)

[119] "Waves and fields in optoelectronics" Hermann A. Haus, Prentice Hall (1984)

[120] *Gabriela González, personal communication* from her note: "Some calculations on optical cavities" (2000)

[121] "Vetoes for Inspiral Triggers in LIGO Data" N Christensen, P Shawhan and G González (for the LIGO Scientific Collaboration), Class. Quantum Grav. **21** S1747 (2004).

[122] "Gravitational wave burst vetoes in the LIGO S2 and S3 data analyses" Allesandra Di Credico, Class. Quantum Grav. 22 S1051 (2005).

[123] "PQMon: a powerful veto for burst events" K Kötter, I S Heng, M Hewitson, K A Strain, G Woan and H Ward, Class. Quantum Grav. **20** S895 (2003).

[124] "Signal Extraction in a Power-Recycled Michelson Interferometer with Fabry-Perot Arm Cavities by Use of a Multiple-Carrier Frontal Modulation Scheme" Daniel Sigg, Nergis Mavalvala, Joseph Giaime, Peter Fritschel, David Shoemaker, Applied Optics, **37**, Issue 24, 5687, (1998).

[125] "Alignment of an Interferometric Gravitational Wave Detector" Peter Fritschel, Nergis Mavalvala, David Shoemaker, Daniel Sigg, Michael Zucker and Gabriela González, Applied Optics, **37**, Issue 28, 6734 (1998).

[126] "Shot Noise in Gravitational-wave Detectors with Fabry-Perot Arms" Torry T. Lyons, Martin W. Regehr, Frederick J. Raab., LIGO-P000014-00-D Applied Optics, Vol. 39, Issue 36, pp. 6761-6770 (2000)

[127] "Multiresolution techniques for the detection of gravitational-wave bursts" S Chatterji, L Blackburn, G Martin and E Katsavounidis, Class. Quantum Grav. **21** S1809 (2004).

[128] "Random Data. Analysis and Measurement Procedures" Julius S. Bendat and Allan G. Piersol, *2nd Edition* John Wiley and Sons (1986)

[129] "An Introduction to Matched Filters" George L. Turin, IRE Transactions on Information Theory 6 311 (1960)

[130] "χ^2 testing of optimal filters for gravitational wave signals: An experimental implementation" L. Baggio et al., Phys. Rev. D 61, 102001 (2000)

[131] The LSC Algorithm Library (LAL) `http://www.lsc-group.phys.uwm.edu/daswg/projects/lal.html`

Appendix A: Derivation of Distance Errors from Chapter 3

To compute the average input distance error $\langle \sigma_{D_I} \rangle$ we do the following:

- Assume D_i is the true distance to a galaxy i.

- We have two different measures of distance in Tully's catalog: $D_{M,i}$ and $D_{Q,i}$

- We assume that both $D_{M,i}$ and $D_{Q,i}$ measure the distance D_i with some uncertainty parametrized $S_{M,i}$ and $S_{Q,i}$, which are random variables.

$$
\begin{align}
D_i &= D_{M,i} + S_{M,i} \tag{7.1}\\
D_i &= D_{Q,i} + S_{Q,i} \tag{7.2}\\
D_{M,i} + S_{M,i} &= D_{Q,i} + S_{Q,i} \tag{7.3}\\
S_{M,i} &= D_{Q,i} - D_{M,i} + S_{D_{Q,i}} \tag{7.4}
\end{align}
$$

An important point to note is (indicated in figure 1 of the galaxy paper)

$$
\sum_i^N \frac{[(D_{Q,i} - D_{M,i})]}{N} \approx 0 \tag{7.5}
$$

It follows that

$$
\langle S_{M,i} \rangle = \langle S_{Q,i} \rangle = 0 \tag{7.6}
$$

But we expect both $S_{M,i}$ and $S_{Q,i}$ to have different widths. We are actually interested in computing the standard deviation of $S_{M,i}$

$$
\sigma_{S_I}{}^2 = \sum_i^N \frac{[D_{Q,i} - D_{M,i} + S_{Q,i}]^2}{N} \tag{7.7}
$$

Expanding gives

$$
\sigma_{S_I}{}^2 = \sum_i^N \frac{[D_{Q,i} - D_{M,i}]^2}{N} + \sum_i^N \frac{\left[S_{Q,i}^2 + 2 S_{Q,i}(D_{Q,i} - D_{M,i})\right]}{N} \tag{7.8}
$$

Now using (7.5) and (7.6) gives

$$
\sigma_{S_I}{}^2 = \sigma_{D_{[Q-I]}}^2 + \sigma_{S_Q}^2 + \sum_i^N \frac{2 S_{Q_i} (D_{Q,i} - D_{M,i})}{N} \tag{7.9}
$$

Now using (3 or 4)

$$\sigma_{S_I}{}^2 \;=\; \sigma^2_{D_{[Q-I]}} + \sigma^2_{S_Q} + \sum_i^N \frac{2S_{Q_i}\left(S_{M,i} - S_{Q,i}\right)}{N} \tag{7.10}$$

And using the fact that $\langle S_{Q,i}\rangle = 0$

$$\sigma_{S_I}{}^2 \;=\; \sigma^2_{D_{[Q-I]}} + \sigma^2_{S_Q} - 2\sigma^2_{S_Q} + \sum_i^N \frac{2S_{Q_i}\,S_{M,i}}{N} \tag{7.11}$$

Since $S_{M,i}$ and $S_{Q,i}$ are uncorrelated

$$\sum_i^N \frac{2S_{Q_i}\,S_{M,i}}{N} \;=\; 0 \tag{7.12}$$

Thus leaving

$$\sigma_{S_I}{}^2 \;=\; \sigma^2_{D_{[Q-I]}} - \sigma^2_{S_Q} \tag{7.13}$$

$\sigma_{D_{[Q-I]}}$ is the width of the histogram computed in figure 1 of the galaxy paper (0.24) and σ_{D_Q} is the average quality distance error (0.10). So $\sigma_{D_I} \approx 0.22$

Appendix B: Copyright Permissions

(22) has been submitted for publication under the following copyright agreement

Ref: : CQG/271437/PAP/139842

ASSIGNMENT OF COPYRIGHT and DECLARATION OF RESPONSIBILITY

1. IOP Publishing Ltd ("the Publisher") agrees to publish

Manuscript title: Method to estimate ISCO and ring-down; frequencies in binary systems and consequences for; gravitational wave data analysis ("**The Article"**) written by

Names of all Authors: C R Hanna, Miguel Megevand, Evan Ochsner, Carlos Palenzuela Luque ("**the Named Authors**")

in the following journal: Classical and Quantum Gravity ("**the Journal**")

2. Transfer of Copyright Agreement

2.1 On acceptance for publication the undersigned author(s) ("Author") of the Article assigns exclusively to IOP worldwide copyright in the Article for the full term and for all media and formats in all material published as part of the Article, which expression includes but is not limited to the text, abstract, tables, figures and graphs, but excludes any supplementary material.

2.2 If any of the Named Authors are Government employees, on acceptance for publication the Author shall grant IOP a royalty free exclusive licence for the full term of copyright for all media and formats to do in relation to the Article all acts restricted by copyright worldwide.

2.3 On acceptance for publication the Author shall grant IOP a royalty free non-exclusive licence for the full term of copyright for all media and formats to do in relation to any supplementary material deemed to be part of the Article all acts restricted by copyright worldwide.

3. Author Rights

3.1 IOP grants the Named Authors the rights specified in 3.2 and 3.3. All such rights must be exercised for non-commercial purposes, if possible should display citation information and IOP's copyright notice, and for electronic use best efforts must be made to include a link to the on-line abstract in the Journal. Exercise of the rights in 3.3 additionally must not use the final published IOP format but the Named Author's own format (which may include amendments made following peer review).

3.2 The rights are:

3.2.1 To make copies of the Article (all or part) for teaching purposes;

3.2.2 To include the Article (all or part) in a research thesis or dissertation;

3.2.3 To make oral presentation of the Article (all or part) and to include a summary and/or highlights of it in papers distributed at such presentations or in conference proceedings; and

3.2.4 All proprietary rights other than copyright.

3.3 The additional rights are to:

3.3.1 Use the Article (all or part) without modification in personal compilations or publications of a Named Author's own works (provided not created by third party publisher);

3.3.2 Include the Article (all or part) on a Named Author's own personal web site;

3.3.3 Include the Article (all or part) on web sites of the Institution (including its repository) where a Named Author worked when research for the Article was carried out; and

3.3.4 Include the Article (all or part) on third party web sites including e-print servers, but not on other publisher's web sites.

Signature

In signing this Agreement the Author represents and warrants that the Article is the original work of the Named Authors, it has not been published previously in any form (other than as permitted under clause 3.2.2 which fact has been notified to IOP in writing), all Named Authors have participated sufficiently in the conception and writing of the Article, have received the final version of the Article, agree to its submission and take responsibility for it, and submission has been approved as necessary by the authorities at the establishment where the research was carried out.

The Author warrants that he/she signs this Agreement as authorised agent for all Named Authors and has the full power to enter into this Agreement and to make the grants it contains, that the Article has not been and will not be submitted to another publisher prior to withdrawal or rejection, it does not infringe any third party rights, it contains nothing libellous or unlawful, all factual statements are to the best of the Author's knowledge true or based on valid research conducted according to accepted norms, and all required permissions have been obtained in writing.

All Named Authors assert their moral rights.

Author's signature……………………………………........…………Date……………………

(118) is published and permission is granted to reproduce it.

Chad Hanna
<channa@phys.lsu.edu>
30/01/2008 15:32

To Permissions <permissions@iop.org>
cc
bcc
Subject Re: Use of Class. Quantum Grav. 23 S17 in my thesis

Hello,

Thanks for your quick reply! I would like permission to reproduce Figures
1-4 and their captions as well as the text in sections 2-6. Please let me
know if this is okay. For clarification, the thesis will _not_ be
published in another scientific journal. It will however be part of LSU's
electronic dissertation database for public access. I will cite the use
of the CQG paper appropriately.

Thanks again!

Chad

\\

On Wed, 30 Jan 2008, Permissions wrote:

> Dear Dr Hanna
>
> Thank you for your permission to the IOP. We however require more
> information of the figure(s) / text you wish to reproduce. Please can you
> reply to the following email address with further details, so that your
> request can be processed.
>
> Best Wishes
>
> Sarah Ryder
>
> Publishing Administrator
> Email: permissions@iop.org

PERMISSION TO REPRODUCE AS REQUESTED
IS GIVEN PROVIDED THAT:

~~(a) the consent of the author(s) is obtained~~
(b) the source of the material including author/editor,
    title, date and publisher is acknowledged.

IOP Publishing Ltd
Dirac House
Temple Back
BRISTOL
BS1 6BE   31/1/08   *(signature)*
                Date   Rights & Permissions

(34) is published and permission is granted to reproduce it.

```
------------------------------------------------------------------------
From Judy.Johnson@aas.org Thu Feb  7 14:28:29 2008
Date: Thu, 7 Feb 2008 15:13:33 -0500
From: Judy Johnson <Judy.Johnson@aas.org>
To: channa@phys.lsu.edu
Subject: RE: Permission to use ApJ MS# 72322 in my thesis

Dear Mr. Hanna,

Thank you very much for your permissions enquiry relating to ApJ
manuscript #73222; Host Galaxies Catalog Used in LIGO Searches for
Compact Binary Coalescence Events; to be published in a journal of
the American Astronomical Society.

Since you are one of the original authors, we are pleased to grant the
necessary permission for your use of this material.  We ask that you give
the original citation for the material. You may also acknowledge the
Society through the wording; reproduced by permission of the
AAS;

Truly,

Judy Johnson

--
Judith M. Johnson
Deputy Journals Manager
American Astronomical Society
2000 Florida Ave., NW, Suite 400
Washington, DC 20009
johnson@aas.org
202-328-2010, ext. 104
www.aas.org
------------------------------------------------------------------------
```

Vita

Chad Hanna was born in Grove City, Pennsylvania. He received a Bachelor of Science in physics from The Pennsylvania State University in 2004 and a Master of Science in physics from Louisiana State University in 2006.